Performance Enhancements of Microfluidic Fuel Cells with Flow-Through Porous Electrodes

by

Jin Wook Lee

M.A. (Aeronautics & Astronautics), Massachusetts Institute of Technology, 2000
B.Sc. (Mechanical Engineering), Yonsei University (Seoul), 1998

Thesis Submitted In Partial Fulfillment
of the Requirements for the Degree of
Doctor of Philosophy

in the
School of Engineering Science
Faculty of Applied Sciences

SIMON FRASER UNIVERSITY

Fall 2012

Approval

Name: **Jin Wook Lee**

Degree: **Doctor of Philosophy (Mechatronic Systems Engineering)**

Title of Thesis: ***Performance Enhancements of Microfluidic Fuel Cell with Flow-Through Porous Electrodes***

Examining Committee: **Chair: Behaad Bahreyni**
Assistant Professor

Erik Kjeang
Senior Supervisor
Assistant Professor

Woo Soo Kim
Supervisor
Assistant Professor

Michael Eikerling
Supervisor
Associate Professor

Farid Golnaraghi
Internal Examiner
Professor
School of Engineering Science

Mu Chiao
External Examiner
Associate Professor
Mechanical Engineering
University of British Columbia

Date Defended/Approved: December 11, 2012

Partial Copyright Licence

The author, whose copyright is declared on the title page of this work, has granted to Simon Fraser University the right to lend this thesis, project or extended essay to users of the Simon Fraser University Library, and to make partial or single copies only for such users or in response to a request from the library of any other university, or other educational institution, on its own behalf or for one of its users.

The author has further granted permission to Simon Fraser University to keep or make a digital copy for use in its circulating collection (currently available to the public at the "Institutional Repository" link of the SFU Library website (www.lib.sfu.ca) at http://summit/sfu.ca and, without changing the content, to translate the thesis/project or extended essays, if technically possible, to any medium or format for the purpose of preservation of the digital work.

The author has further agreed that permission for multiple copying of this work for scholarly purposes may be granted by either the author or the Dean of Graduate Studies.

It is understood that copying or publication of this work for financial gain shall not be allowed without the author's written permission.

Permission for public performance, or limited permission for private scholarly use, of any multimedia materials forming part of this work, may have been granted by the author. This information may be found on the separately catalogued multimedia material and in the signed Partial Copyright Licence.

While licensing SFU to permit the above uses, the author retains copyright in the thesis, project or extended essays, including the right to change the work for subsequent purposes, including editing and publishing the work in whole or in part, and licensing other parties, as the author may desire.

The original Partial Copyright Licence attesting to these terms, and signed by this author, may be found in the original bound copy of this work, retained in the Simon Fraser University Archive.

Simon Fraser University Library
Burnaby, British Columbia, Canada

revised Fall 2011

Abstract

This thesis presents performance improvements of microfluidic fuel cells with flow-through porous electrodes. The baseline cell is a laminar flow-based, membraneless, microfluidic fuel cell employing vanadium redox species (as electrolytes). The main objective of the current work is to establish a design guideline for microfluidic fuel cells and to propose new design strategies that lead to better performing cells. The fundamental physics including fluid flow, electrochemical reactions in porous media, and convective/diffusive mass transport is closely investigated. Various loss elements during the baseline cell operation such as activation, ohmic, and mass transport losses are identified and compared. Some feasible and practical remedies to reduce the overall losses are proposed and successfully demonstrated: thin film current collector for the overall ohmic loss; nanofoam material as electrodes to reduce the activation loss; and novel concept to overcome mass transport limited performances. Further improvements would be anticipated if both ohmic and fluidic resistances of the nanofoam material are reduced. Uniform distribution of the pore sizes is also important to maximize the utilization of active electrode areas. When combined, the demonstrated technologies and design improvements are anticipated to bring this unique membraneless and catalyst-free fuel cell closer to commercialization as a low-cost power source.

Keywords: microfluidics; laminar flow; fuel cell; vanadium; carbon materials; electrochemistry; nanofluidics;

Dedication

This thesis is dedicated to my father who always influences me with his courage and patience. It is also dedicated to my mother who always prays for me and never gives up. Finally, this thesis and all the accomplishments I made during my doctoral program at SFU are dedicated to my beloved wife, Ji yeon, for her endless love and sacrifices. Without her supports, I would have never succeeded in what I have done for last 3 years at SFU.

Acknowledgements

I would like to express my utmost appreciation to Dr. Erik Kjeang who introduced me this wonderful opportunity for entry to a world of microfluidic fuel cells. His advice and guidance have always stimulated my intellectual curiosity in constructive ways. Every aspect of the valuable supports from Dr. Kjeang undoubtedly served as a solid platform of all the accomplishments I made during my stay at Simon Fraser University. I also would like to thank my committee members, Drs. Woo Soo Kim and Michael Eikerling for their considerate advice and relevant questions, which solidified and improved the quality of my thesis.

I have to thank the co-op students that I worked with for their assistance and cooperation: Peter Hsiao, Larry Hoang, and David Afonso. Special thanks to Mr. Jun Ki Hong who joined our research team as a visiting student and wrote his undergrad thesis with us. Mr. Hong's dedication is highly appreciated especially for his assistance in the electrochemical measurements.

I would like to say “thank you” to colleague students in my office: Mr. Abhisheck Nanjundappa for his smiley face, which made my stay at SFU much more pleasant; Mr. Marc-Antoni Goulet for his diligence and dedication. I also thank Mr. Alireza Sadeghi Alavijeh for his assistance with SEM images at 4D LABs in Burnaby.

Very special thanks to Ms. Mary Boysel, Manager of the Nanofabrication Facility in 4D LABS, for her valuable support. The Natural Sciences and Engineering Research Council (NSERC) of Canada and a Simon Fraser University President's Research Start-up Grant is highly appreciated.

Table of Contents

List of Tables

List of Figures

List of Acronyms

EIS	Electrochemical Impedance Spectroscopy
IPA	Isopropylalcohol
LFFC	Laminar Flow-based Fuel Cell
MPL	Micro Porous Layer
OCV	Open Circuit Voltage
PDMS	Polydimethylsiloxane (also known as silicone)
PTFE	Polytetrafluoroethylene (also known as Teflon)
SCE	Standard Calomel Electrode
V(II)	V^{2+}
V(III)	V^{3+}
V(VI)	VO^{2+}
V(V)	VO_2^+

1. Introduction

1.1. Background and Motivation

Recent increasing demands on small-scale power sources for portable electronics have significantly boosted the interest in miniaturized fuel cells. Even though for the most of portable applications, secondary or rechargeable batteries are currently prevailing in the market, fuel cells can be an attractive alternative solution due to its fast re-chargeability. In addition, it has been reported that miniaturized fuel cells may enable higher overall energy densities than conventional batteries [1]. Potential applications of miniaturized fuel cells include portable electronic devices, remote sensors, and an auxiliary charger for onboard batteries. However, the present small-scale fuel cell technologies are generally suitable for low power applications such as wireless sensing nodes and require significant research investments to scale up for higher power output [1].

Small fuel cell technologies employing conventional electrocatalysts have been dominated by hydrogen-based proton exchange membrane (PEM) fuel cells and direct liquid fuel cells [2-6]. The overall architecture is generally similar to the conventional macro-scale PEM fuel cells and consequently, a stack of substrates and PEM layers is the predominant approach, resulting in a multi-layer configuration. Many system-level issues including air movement, fuel delivery, water management, thermal management and system integration were addressed and some implemented engineering solutions were proposed [2]. A bulk silicon micromachined microbial fuel cell employing cultured yeast, *S. cerrevisiae,* was introduced by Chiao et al. [7]. Although the cell performance was relatively low, this was an important technical contribution as a feasible miniaturization strategy for microbial fuel cells.

Another branch in the context of miniaturized fuel cell technology is microfluidic fuel cells or laminar flow-based fuel cells (LFFC) [8-10]. Due to the laminar nature of microscale flows to maintain separation between fuel and oxidant streams, such fuel cells predominantly operate without a physical membrane. A silicon-based microchannel for membraneless LFFC with horizontal flow-over electrodes was proposed by Cohen et al. [11]. E-beam evaporated Pt catalyst layers were placed at the top and bottom of the channel where two electrolytes were supplied horizontally. An air-breathing laminar flow-based microfluidic fuel cell was reported by Jayashree et al. [12]. A porous air-breathing gas diffusion cathode was integrated and significantly enhanced the oxygen reduction reaction rate and consequently the power density of the cell. A three-dimensional microfluidic fuel cell with ahexagonal array of graphite rods was introduced by Kjeang et al. [13]. Commonly employed as mechanical pencil leads, graphite rods served as both electrodes and current collectors for this unique three-dimensional fuel cell architecture. A counter flow membraneless microfluidic fuel cell design combined with flow-through porous carbon electrodes was invented by Salloum et al. [14] and operated on vanadium electrolyte. A sulfuric acid stream was injected at the interface to separate the fuel and oxidant streams. More recently, a multi-stack microfluidic fuel cell with porous flow-through electrodes was introduced [15], which employed vanadium redox electrolyte and a new form of porous carbon electrode made by laser ablation and pyrolsis process.

Membraneless fuel cell configurations also feature typical lab-on-chip designs that only require a single layer of microfluidic channels [8, 16]. This allows conventional microfabrication or micromachining techniques to be readily applicable, which is a preferable fabrication approach for microscale devices due to low cost, high precision, and repeatability. Moreover, batch process capability provides an opportunity for further cost reductions, if the devices are mass produced [17]. Problematic crossover effects are eliminated by strategic cell design, provided that interdiffusion is restricted to a small interfacial width at the center channel, from which the electrodes are positioned sufficiently far away [16].

More recently, a microfluidic fuel cell in flow-through porous electrode configuration was introduced by Kjeang et al. [13]. The design was based on cross-flow of aqueous vanadium redox species through the porous electrodes into an orthogonally arranged co-laminar exit channel, where the waste solutions provided ionic charge transfer in a membraneless configuration. This microfluidic vanadium fuel cell device demonstrated the highest power density levels (131 mW cm^{-2} with 300 μm thick electrodes) reported to date in this field [18, 19].

However, preliminary studies performed by our group indicate that the cell performance can be drastically improved, if the design parameters are optimized and better electrode materials are selected. To my knowledge, a matrix of optimized design and the selection of electrode materials for microfluidic fuel cells has not been developed and reported in the literature. In this thesis, a thorough investigation with an emphasis on the enhancement of cell performance will be performed to implement new design strategies and to identify physical limits of a microfluidic fuel cell employing vanadium redox electrolytes. In addition, various carbon-based materials will be examined in favor of cell performance.

1.2. Previous Work

It was late 1970s when the NASA-Lewis Research Center was involved in the development of a complete redox energy storage system based on Fe(III)/(II) and Cr(III)/(II) couples [20, 21]. They also conducted an initial screening of a large number of redox couple/electrode combinations including V(II)/V(III). Vanadium (symbol: V) is a hard, silvery gray, ductile and malleable transition metal. At that time, the cost associated with vanadium species was an issue but for some applications, an overall efficiency of redox couples is often more important. The electrochemical behavior of V(II)/V(III) redox couple at glassy carbon electrodes was led by Dr. Skyllas-Kazacos' research group at University of New South Wales [22]. The oxidation/reduction rates (k^o) at pH= 4 were experimentally obtained and a general trend in k^o with pH was observed. A positive half cell with V(V)/V(VI) at glassy carbon and gold electrodes was investigated by the same group [23]. More recently, Gattrell et al. [24] examined a kinetic mechanism of V(V)/V(VI) redox couple in acidic aqueous solutions. The analytical model was compared with experimental data and showed a fair agreement at various pH levels and concentrations of vanadium.

In 2002, Ferrigno et al. [8] introduced a very unique design feature for microfluidic fuel cells using vanadium redox species, which eliminated the membrane and catalyst. The design was based on a microfabricated, y-shaped fluidic channels whose height was less than 200 μm. Two planar thin film electrodes were located at the bottom of a y-shaped flow channel in which the fuel and oxidant were supplied in a co-laminar fashion (Figure 1). This design exploited the laminar flow that occurred in liquids flowing at low Reynolds number, while minimizing convective mixings of fuel/oxidant.

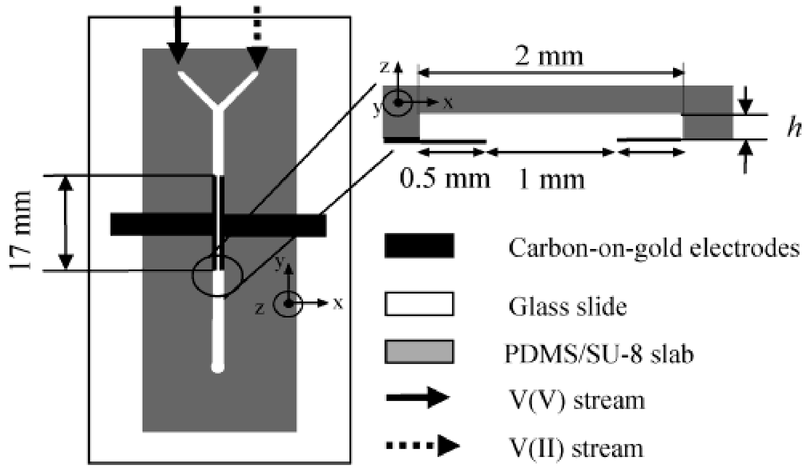

Figure 1. ***Schematic design of a vanadium redox microfluidic fuel cell [8]. Copyright ACS (2002).***

Another breakthrough in microfluidic fuel cells was made by adopting a concept of flow-through porous electrodes [13]. The main idea is to increase the utilization of actual electrode surfaces by employing porous media commonly used as a gas diffusion layer in conventional fuel cells. The device demonstrated the highest power density levels (131 mW cm^{-2} with 300 μm thick electrodes) reported to date in this field [18, 19] and served as a baseline cell throughout the current thesis.

The baseline design of the microfluidic fuel cell with flow-through porous electrodes considered in this proposal comprises two separate flow inlet ports and one common outlet port, as shown in Figure 2. The overall device architecture is consistent with the standard flow-through cell design previously developed by our group [13]. The fuel (V(II)) and oxidant (V(V)) are fed into the inlet ports and flow through the porous electrodes that are inserted in the microfluidic channel. Two electrical contacts, denoted anode and cathode in Figure 2, are located at the end of the electrodes to transfer the electrical current generated from the fuel cell to external wires that are attached using conductive silver epoxy.

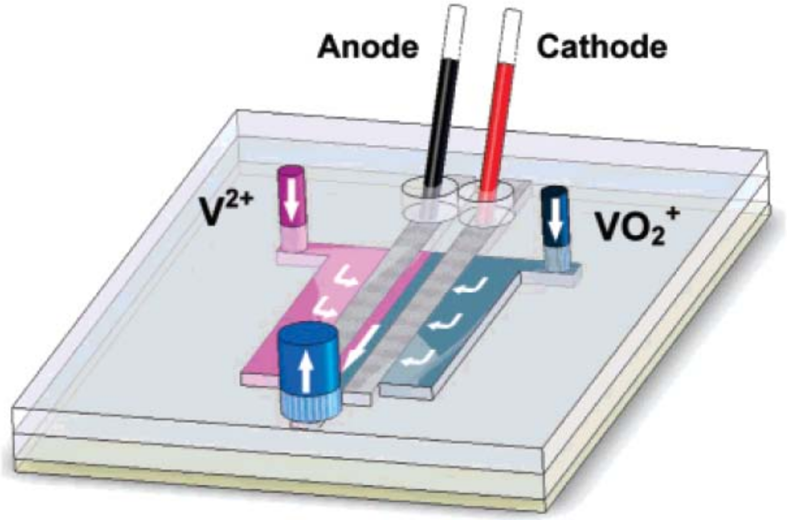

Figure 2. Schematic of the microfluidic fuel cell architecture with flow-through porous electrodes used as baseline in this study [13]. Copyright ACS (2008).

The choice of vanadium electrolyte as fuel originated from a rapid and balanced electrochemical system in terms of species transport characteristics and reaction rates. The rapid vanadium redox reactions on carbon electrodes sufficiently eliminated any additional catalyst and associated cost. In addition, the vanadium ions employed have four different oxidation states that enable a well-balanced all-vanadium fuel and oxidant combination for redox applications with in situ regeneration capabilities. The cell was reported to have relatively high ohmic resistance and associated voltage loss [25]. External wires were attached to the exposed ends of the porous carbon electrodes using conductive silver epoxy, which likely resulted in a sizeable contact resistance owing to the highly porous nature of the electrodes.

1.3. Objectives of Current Research

The current research was originally initiated to investigate the baseline cell performance, which is a membraneless, microfluidic fuel cell that employs vanadium redox species. The main objective is to establish a design guideline for microfluidic fuel cells and to propose new design strategies that lead to better performing cells. More detailed sub-goals are summarized:

- Understand fundamental physics that governs the cell operation, including fluid flow, electrochemical reactions in porous media, and convective/diffusive mass transport (Chapter 3).
- Explain and distinguish various loss elements during the baseline cell operation, such as activation, ohmic, and mass transport losses (Chapter 3).
- Propose feasible and practical remedies to reduce the losses and therefore improve the cell performance (Chapter 4, 6, & 7).
- Examine and characterize new carbon-based materials for their potential usage as porous electrodes in flow-through fuel cell configuration (Chapter 5 & 6).
- Develop a new fabrication technique for better precision and repeatability in a cost effective way (Appendix).

1.4. Thesis Layout

In Chapter 2, section 2.1 explains a generic fuel cell and its basic operation along with polarization curves. Section 2.2 is dedicated to introduce a vanadium microfluidic fuel cell and some fundamental theories: vanadium redox reactions, Nernst equation and Butler-Volmer equation.

A parametric study on microfluidic vanadium fuel cell is presented in Chapter 3. Dimensional variations of porous carbon electrodes and microchannels are discussed to evaluate their impacts on the fuel cell performance. Both numerical and experimental studies are performed to understand fundamentals of the baseline fuel cell design.

In Chapter 4, a chip-embedded thin film (Au) current collector is proposed to mitigate cell contact resistances, which is the major loss element in cell operation. The gain obtained by the proposed design is explained along with some electrochemical measurements.

In Chapter 5, various carbon materials such as graphite rod, regular carbon paper, wet-proofed carbon paper, are investigated and analyzed electrochemically. Basic kinetic parameters for both V(II) and V(V) discharging reactions are estimated from Tafel plot and compared for the different electrodes.

The electrochemical properties of vanadium redox species on novel carbon nanofoam are investigated and presented in Chapter 6. Detailed characteristics of the nanofoam are discussed with an emphasis of the device level performance.

In Chapter 7, a novel cell architecture employing double-pass concept is proposed to improve the overall cell performance. The key concept and complete cell performance are discussed.

The summary and conclusions of the current research are presented in Chapter 8, along with some suggestions for the future development. Finally, the Appendix covers detailed information about the microfabrication that is used for building the microfluidic devices studied in this thesis.

2. Theory

2.1. Basics of Fuel Cell Operation

Figure 3 shows a typical layout of PEM (polymer electrolyte membrane, also known as proton exchange membrane) fuel cell. The anodic and cathodic compartments are physically separated by an ionic conducting electrolyte membrane through which protons transfer from the anode to cathode. Electrons flow through an external circuit and ultimately a load device for electrical work from the anode to cathode to close the circuit. In this particular example, hydrogen is used as fuel, while oxygen, often obtained from the ambient air, is oxidant for chemical reactions. In order to overcome slow reaction rates of hydrogen/oxygen, noble metal catalysts are generally adopted, which is still a substantial portion of the entire fuel cell stack costs [26].

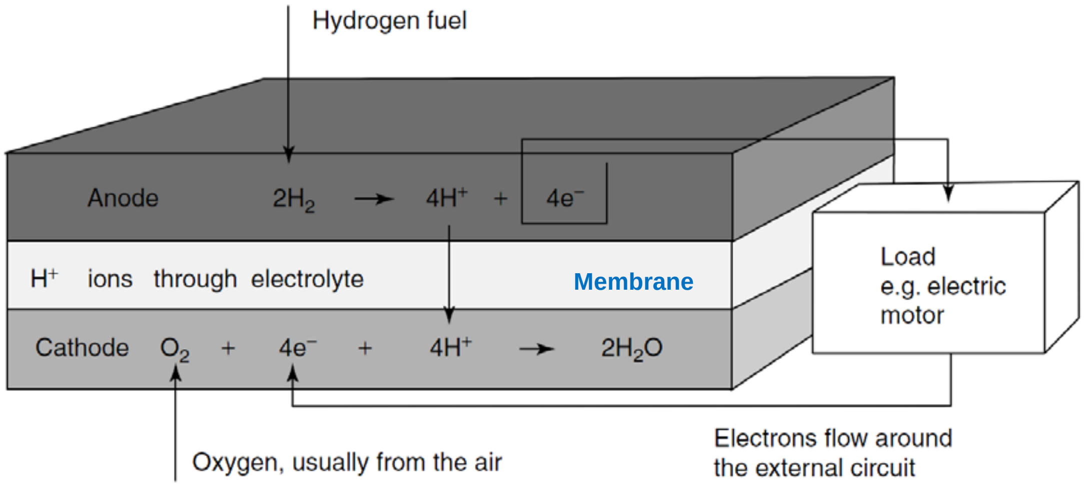

Figure 3. ***Typical anode/electrolyte/cathode configuration and electrode reactions of fuel cells [26].***

2.1.1. Polarization Curve of Fuel Cell Operation

Figure 4 is an illustration of a typical polarization curve for a PEM fuel cell, showing five regions of interest labeled I ~ V [27]:

- Region I: dominated by the activation or kinetic overpotential the electrodes.
- Region II: represents the ohmic polarization of the cell. This includes all electrical and ionic conduction losses through the electrolyte, catalyst layers, cell interconnects, and contacts.
- Region III: dominated by the concentration polarization of the fuel cell, caused by mass transport limitations of the reactants to the electrodes.
- Region IV & V: indicate the gap between the theories and real life, involving a deviation from thermodynamic equilibrium and entropy changes.

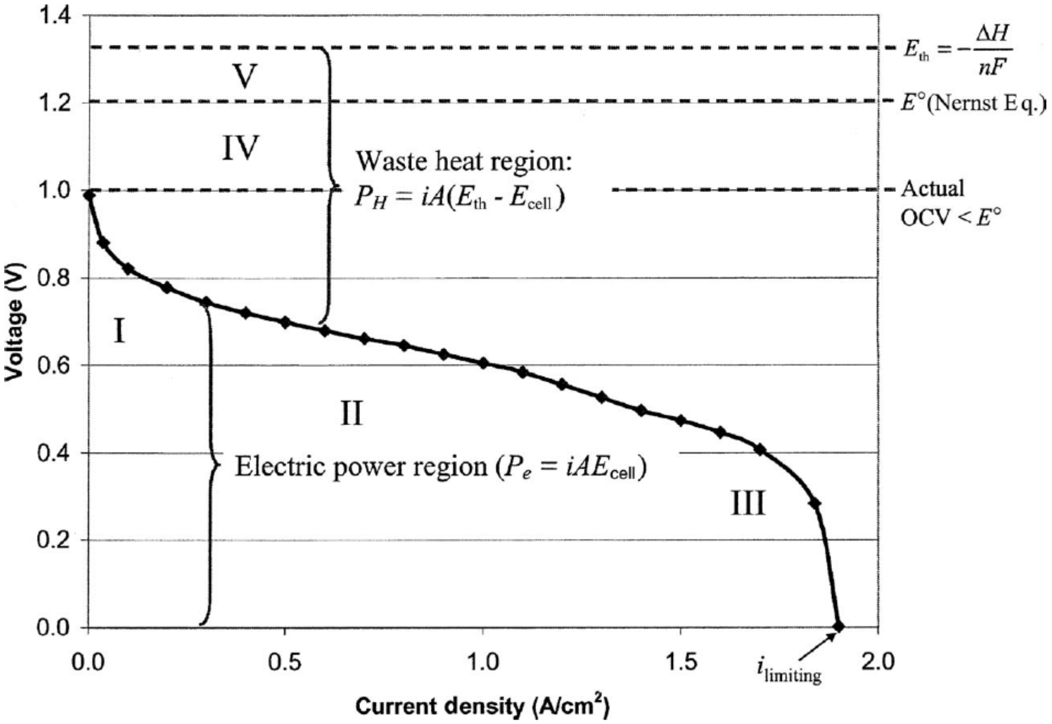

Figure 4. Typical polarization curve for fuel cell with significant losses attributed by various loss sources [27].

Note that $i_{limiting}$ indicates the maximum current density of the cell.

2.2. Vanadium Redox Microfluidic Fuel Cell

While the basic structure and operation are similar to PEM fuel cells, , the membrane can be eliminated in laminar flow based fuel cells (LFFC) or microfluidic fuel cells by a fact that microscale flows maintain separation between fuel and oxidant streams due to the nature of laminar flows at low Reynolds numbers. Problematic crossover effects are avoided by strategic cell design, provided that interdiffusion is restricted to a small interfacial width at the center channel, from which the electrodes are positioned sufficiently far away (Figure 2).

The microfluidic fuel cell devices studied in this thesis utilizes vanadium redox species which are based on the following anodic (1) and cathodic (2) reactions at 298K [28]:

$$V^{3+} + e^- \rightleftarrows V^{2+} \qquad E^o = -0.496V\ vs.SCE \tag{1}$$

$$VO_2^+ + 2H^+ + e^- \rightleftarrows VO^{2+} + H_2O \qquad E^o = 0.750V\ vs.SCE \tag{2}$$

The theoretical standard cell potential is 1.246 V but this can, however, be increased to as high as 1.5 V depending on the concentration ratio of the vanadium species.

2.2.1. *Nernst Equation and Open Circuit Voltage*

2 M vanadium electrolyte solutions are prepared from stock electrolyte in 4 M sulfuric acid base according to a previously reported procedure [13]. Assuming a constant proton concentration of 8 M (from 4M sulfuric acid as a supporting electrolyte), the Nernst equations for half-cell reactions (3) for anode and (4) for cathode can be solved to estimate the initial concentrations of V(II) (fuel) and V(V) (oxidant) in 4 M sulfuric acid electrolyte:

$$E_{OCV} = E^0 + \frac{RT}{F} ln\left[\frac{[V^{3+}]}{[V^{2+}]}\right] \tag{3}$$

$$E_{OCV} = E^0 + \frac{RT}{F} ln\left[\frac{[VO_2^+][H^+]^2}{[VO^{2+}]}\right] \tag{4}$$

where E_{OCV} is open circuit voltage, which is the potential when no electrical currents flow. First, OCVs are measured by using a graphite bar and a saturated calomel electrode (Fisher Scientific) and recorded. And then E^o values from the equation (1) & (2) are used to calculate the initial concentrations of V(II) /V(V).

2.2.2. Butler-Volmer Equation

The Butler Volmer equation has been playing an essential role in electrochemistry as a basic tool for modeling simple electron transfer reactions. Fabjan et al. [29] reported experimentally that a single electron transfer was the rate determining step in the vanadium redox kinetics. Several earlier modeling efforts of vanadium redox batteries [30, 31] have shown that performance of a cell based on these reactions is adequately captured by the Butler–Volmer equation. Therefore, given the uncertainties that exist with regards to the kinetics of the vanadium redox reactions, the Butler–Volmer equation [25] is justified simplification for the present work. The charge transfer current densities corresponding to the redox reactions are given by the following general form of Butler Volmer equation:

$$i_1 = i_1^o \left\{ \frac{c_{IV}^s}{c_{IV}} exp\left(\frac{\alpha_{1,a} F \eta_1}{RT}\right) - \frac{c_V^s}{c_V} exp\left(\frac{-\alpha_{1,c} F \eta_1}{RT}\right) \right\} \tag{5}$$

$$i_2 = i_2^o \left\{ \frac{c_{II}^s}{c_{II}} exp\left(\frac{\alpha_{2,a} F \eta_2}{RT}\right) - \frac{c_{III}^s}{c_{III}} exp\left(\frac{-\alpha_{2,c} F \eta_2}{RT}\right) \right\} \tag{6}$$

Note that subscript 1 refers to the V(V)/V(VI) side, which is the cathode during fuel cell operation, and subscript 2 refers to the V(II)$^/$V(III) side, or the anode. The superscript s refers to the surface concentration of the vanadium species. α is the charge transfer coefficient, with subscripts *a* and *c* referring to oxidation (anodic) and reduction (cathodic) reactions, respectively. *F* is Faraday's constant, *R* is the universal gas constant, *T* is the operating temperature and η is the overpotential. The exchange current density i^o represents the rate of charge transfer when the reaction is at equilibrium. For the cathode and anode side it is written as:

$$i_1^o = F k_1 (c_{IV})^{\alpha_{1,c}} (c_V)^{\alpha_{1,a}} \tag{7}$$

$$i_2^o = Fk_2(c_{II})^{\alpha_{2,c}}(c_{III})^{\alpha_{2,a}} \qquad (8)$$

where k_1 and k_2 are the standard reaction rate constants.

3. A Parametric Study on Microfluidic Fuel Cell

A parametric variation of microfluidic vanadium redox fuel cells is studied. The present membraneless and catalyst-free fuel cell consists of a microfluidic channel network with two porous carbon paper electrodes. An aqueous vanadium redox pair as reactants is supplied to the porous electrodes in a flow-through configuration. The dimensions of porous carbon electrodes and microchannels are varied from the baseline design to investigate their impacts on the fuel cell performance. In addition, a dependency on the number of electrical contacts is examined. Numerical simulations are performed in parallel with experimental activities to understand the coupled effects of mass transport, electrochemistry, electron conduction, and fluid mechanics. The simulation results are compared with the measured data from each cell design for verification. An optimal cell design is discussed based on the current study and future research opportunities are proposed.

3.1. Methodology

3.1.1. Baseline Design

As mentioned, the baseline cell consisted of two separate flow inlet ports and one common outlet port. The fuel (V(II)) and oxidant (V(V)) are fed into the inlet ports and flow through the porous electrodes that are inserted in the microfluidic channel. Two electrical contacts, denoted anode and cathode in Figure 5 (a), are located at the end of the electrodes to transfer the electrical current generated from the fuel cell to external wires. Note also that the net width and length of the porous electrodes are denoted as *W* and *L*, respectively. In the center channel, two electrolytes formed a co-laminar flow as shown in Figure 5 (b).

(a)

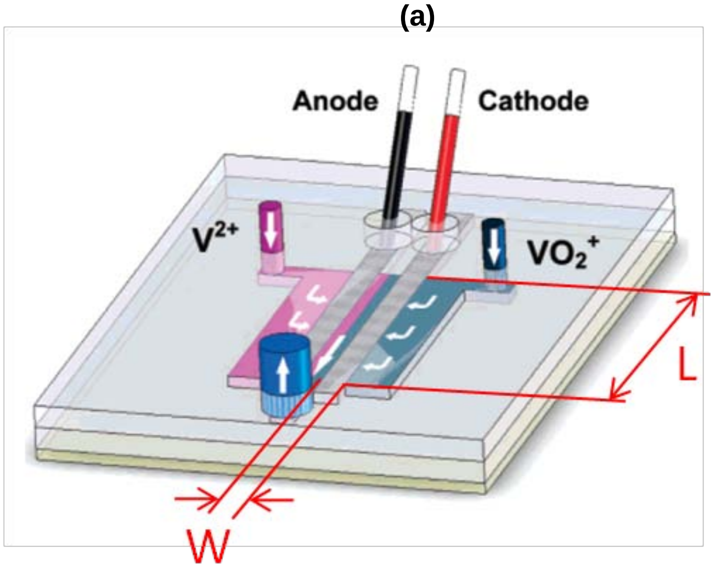

(b)

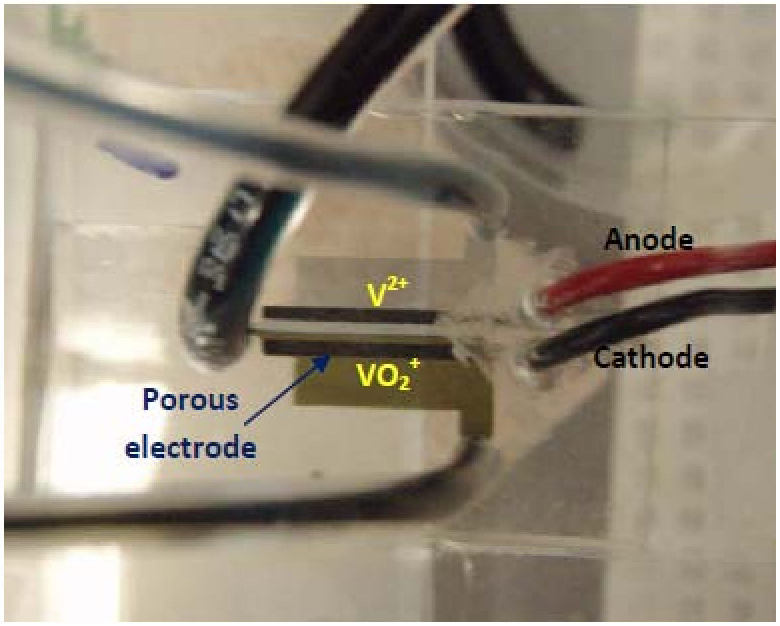

Figure 5. ***(a) Schematic of the baseline cell; and (b) photograph of actual cell operation.***

3.1.2. Parametric Study

The logic behind this parametric study is to investigate how dimensional variations of the electrode make impacts on the cell performance. The increments by a factor of 2 or 0.5 are applied in the dimensions of electrode length, width, and center channel. An interesting question is whether the cell performance is also increased or decreased in a proportional way corresponding to these incremental changes. Four independent geometrical parameters associated with the microfluidic fuel cell design are considered in this parametric study as listed in Table 1. Note that the variations are in bold fonts; for instance, *Case I* refers to “double width” electrode whose width is 2 mm. The center channel width (column 3) refers to the gap between two electrodes across the center channel of the cell.

Table 1. Dimensional variations of the fuel cell geometry in the parametric study.

	W [mm]	L [mm]	Center channel width [mm]	Number of contacts	Electrode area [cm^2]
Baseline	1	12	1	1	0.12
Case I	2	12	1	1	0.24
Case II	1	6	1	1	0.06
Case III	1	12	0.5	1	0.12
Case IV	1	12	1	2	0.12

For the fuel cell with double contacts (Case IV), two contacts are placed at both ends of the electrode to investigate the impact on the cell performance. The currents generated are collected through two ports in a form of electrically joined wires where an external load is connected serially.

3.1.3. Cell Fabrication

The cells are built by a well-established soft lithography technique [32]. Masters for the replica molding step are fabricated by using SU-8 2100 series photoresist purchased from MicroChem. In order to accommodate a Toray carbon paper (TGPH-060) with nominal thickness of approximately 180 μm, the target height of the master is chosen accordingly (180 μm). Polydimethylsiloxane (PDMS, DowCorning) is poured and cured for over 48 hrs at a room temperature and finally peeled off from the mold. After carbon papers are inserted in the microchannel, the PDMS microchannel structure is bonded onto a substrate (glass slide, 1" X 3"). The PDMS surface and the substrate are functionalized by a Corona Treater (BD-20AC, Electro-Technic Product Inc.) for 40 seconds before bonding. The electrical contact between the carbon electrodes and external wires is made using a silver conductive epoxy (MG Chemicals), which is expected to result in a sizeable contact resistance owing to the highly porous nature of the electrode surface. More detailed descriptions for the soft lithography fabrication can be found in [32] and Appendix (p.104-105). The carbon paper is cut manually by using an in-house jig and later inserted in the micro channel manually as well.

3.1.4. Preparation of Vanadium Solutions

Vanadium stock electrolyte was donated by a local company and received as 2 M vanadium redox species (50/50, V(III)/ V(V)) in 4 M sulfuric acid base. The solution is recharged by an in-house charger to produce V(II)/ V(V) that are used as anolyte and catholyte, respectively [33]. The actual concentration of V(II) achieved from the charger is 93.6% (equivalent to 1.87 M), while V(V) reached 93.2% (equivalent to 1.86 M).

3.1.5. Instrumentation

Polarization curves are generated by measuring the voltage across external resistances directly connected with the electrical contacts of the cells as shown in Figure 6. The current generated by the cells is monitored until a steady reading is achieved (30 ~ 40 seconds, depending on the flow rate). Two flow rates (10 μL min^{-1}, 300 μL min^{-1}) are chosen to investigate a low and a high flow regime, respectively. The current density and power density in the model are based on the top surface area of each electrode (listed in the last column of Table 1.) to be consistent with the previously reported data [13].

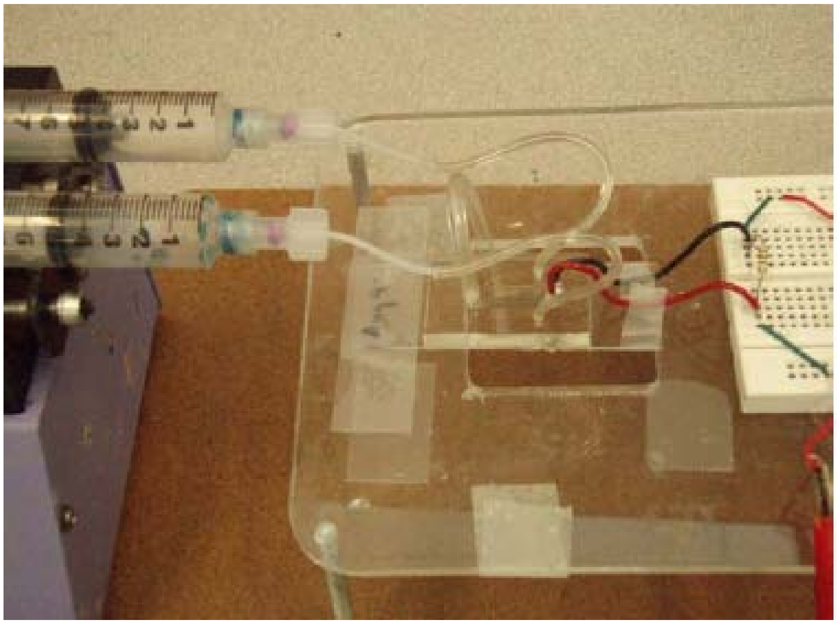

Figure 6. Experimental set up for the current study.

The electrolyte flow is driven and controlled by a dual syringe pump (MA1 70-2209, Harvard Apparatus). The fluidic connections between the device and syringes are achieved by forced fitting of Tygon tubing (R-3603).

The actual dimensions of the carbon electrodes are measured after the cell fabrication by an optical microscope (Nikon, LV 100). A surface profilometer (Mitutoyo, SJ-400) is used to measure the actual height of the SU-8 masters, which turns out to be identical to the channel height of replica PDMS mold.

Table 2. Measured dimensions of the key features.

	Electrode width [mm]	Center channel width [mm]	Channel height [mm]
Baseline	0.935	1.081	0.170
Case I	1.620	1.049	0.162
Case II	0.941	0.892	0.184
Case III	0.883	0.456	0.166
Case IV	0.935	1.081	0.170

Note that all values are averaged after measured 3 different locations.

3.1.6. *Numerical Simulation*

A comprehensive numerical model is developed and customized for these cells based on conservation of mass, momentum, species, and charge coupled with electrochemical kinetics using a commercially available multiphysics software package (COMSOL). The domain of 3D modeling comprised the interior fluidic parts of the cell, as illustrated in Figure 7(a). Due to high computational costs, the 3D modeling is mainly used to capture the fluidic behavior of the cell. The flow field results from the 3D models then are averaged across the channel thickness and mapped as a boundary condition at the inlet to the electrodes for the 2D model shown in Figure 7 (b). The use of 2D models is validated by directly comparing with the result of full 3D models [25]. Note that the current parametric study is based on the 2D models to save its computational costs. The dimensions for the computational domain are adjusted, based on the geometries listed in Table 1.

The pressure drop across the electrodes is calculated using the Darcy's law, while the incompressible equations for continuity and momentum conservation are used for the flow in the non porous regions [34]. The governing equations for species conservation and charge conservation in the carbon paper electrode and electrolyte are written as [35]:

$$\vec{v}\nabla c_j - D_j^{eff}\nabla^2 c_j = S_j \tag{9}$$

$$\nabla \cdot \vec{\iota_s} = -\nabla \cdot \vec{\iota_l} = -\sigma_s^{eff}\nabla^2\phi_s = k_l^{eff}\nabla^2\phi_l \tag{10}$$

where c_j denotes the bulk concentration of the vanadium species j; D_j^{eff} are the effective diffusion coefficients of species j; S_j are the species source terms for the species j; ϕ_s, ϕ_l are the potentials in the electrode and electrolyte, respectively; $\vec{\iota_s}$, $\vec{\iota_l}$ are the electrode and electrolyte current densities; and σ_s^{eff} and k_l^{eff} are the effective conductivities of the electrode and electrolyte, respectively. The electrode and electrolyte potentials (ϕ_s , ϕ_l) are estimated using Ohm's law and the pre-specified conductivity values [25].

A simple electron transfer reaction is assumed and the complete Butler-Volmer equation, including surface to bulk concentration ratio terms, is solved to estimate the charge transfer current densities corresponding to the redox reactions [26, 27]. The overpotentials at the cathode and anode side are written as:

$$\eta_1 = \phi_s - \phi_l - U_1 \tag{11}$$

$$\eta_2 = \phi_s - \phi_l - U_2 \tag{12}$$

And the Nernst equation is solved to estimate the half cell potentials (U_1, U_2). The rate of vanadium species transported to and from the electrode surface through the combined effect of convection and diffusion is estimated by:

$$S_j = ak_{mj}\left(c_j^s - c_j\right) \tag{13}$$

where c_j^sdenotes the surface concentration of the vanadium species j; a is the internal surface area of the electrode; k_{mj} are the mass transfer coefficients for each vanadium species that are calculated using an empirical relationship for mass transfer in carbon fiber electrodes [36]. More thorough details about the numerical model are available in reference [25], which was reported by our group.

A bridge between this model and a real operating cell is the external resistance in which the contact resistances at the electrical on-chip contacts are dominating. Based on the total ohmic resistance previously reported by Electrochemical Impedance Spectroscopy (EIS) [13] and the internal resistance calculations, a value of 25 Ω is added externally to the model in order to compare with the measured polarization curves [25].

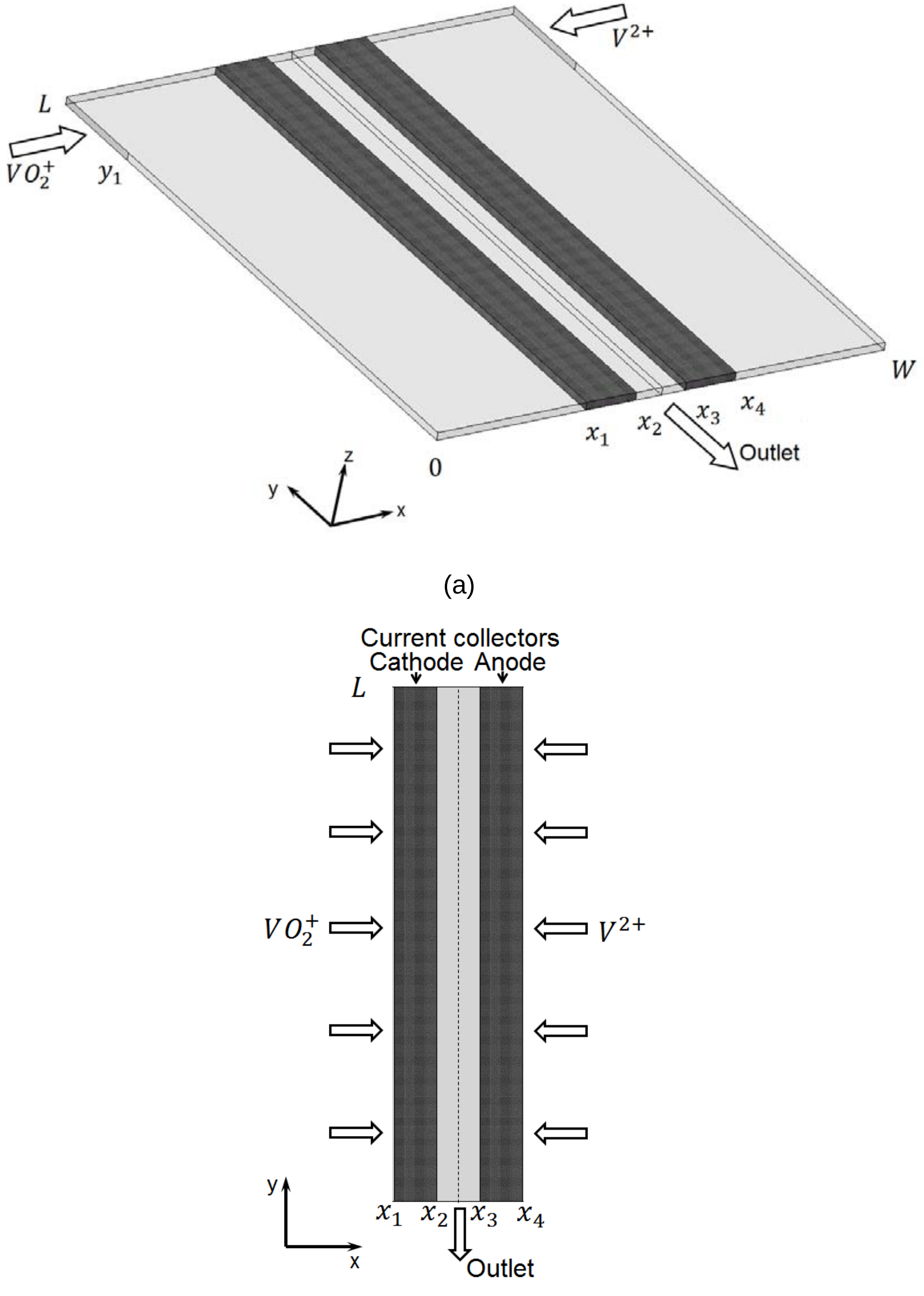

(a)

(b)

Figure 7. ***Schematic of the computational domain: (a) 3D; and (b) 2D [25]. Copyright JPS (2011).***

3.2. Results and Discussions

Both the numerical simulations and measurements of the five variant cells considered in the parametric study are completed and the polarization curves for each case are presented in Figure 8 (modeling predictions) and Figure 9 (measured data). The current densities are calculated by dividing the total current by the planar geometrical surface area of the electrodes given in Table 1 for the modeling investigations and Table 2 for the experimental results, in coherence with the previous work [13].

3.2.1. Results from Numerical Model

The key observations on the simulated polarization curves obtained in the numerical model are summarized below:

- *Mass transport limitations:* At the low flow rate (10 μL min^{-1}) in Figure 8 (a), the polarization curves tail down and the cell potentials tend to have an abrupt drop near the limiting currents due to mass transport limitations, while the polarization curves maintain initial slopes up to the limiting currents for high flow rate (300 μL min^{-1}) in Figure 8 (b), indicative of predominant ohmic losses. The presence of a clear performance drop near the limiting current, observed here at the low flow rate, indicates that the ohmic losses are effectively managed and demonstrates a suitable operating point just before the onset of the mass transport related performance drop. This observation is critical for design and operation of microfluidic fuel cells with respect to flow rate. The measured data confirm this tendency and show a fair agreement.
- *Ohmic cell resistance:* Although the total ohmic resistance of the cell is reduced, the modeling results indicate that no significant deviations from the baseline are expected in Case III (0.5 mm center channel) and Case IV (double contact), especially at the low flow rate (10 μL min^{-1}) where the three curves fall into a single line. This is a clear indication that the mass transport is the main performance-limiting factor at low flow rates. For the high flow rate when the impact of ohmic

losses increases proportionally to the cell current, slightly improved performance is found for Case III (0.5 mm center channel), mainly due to lower ohmic resistances

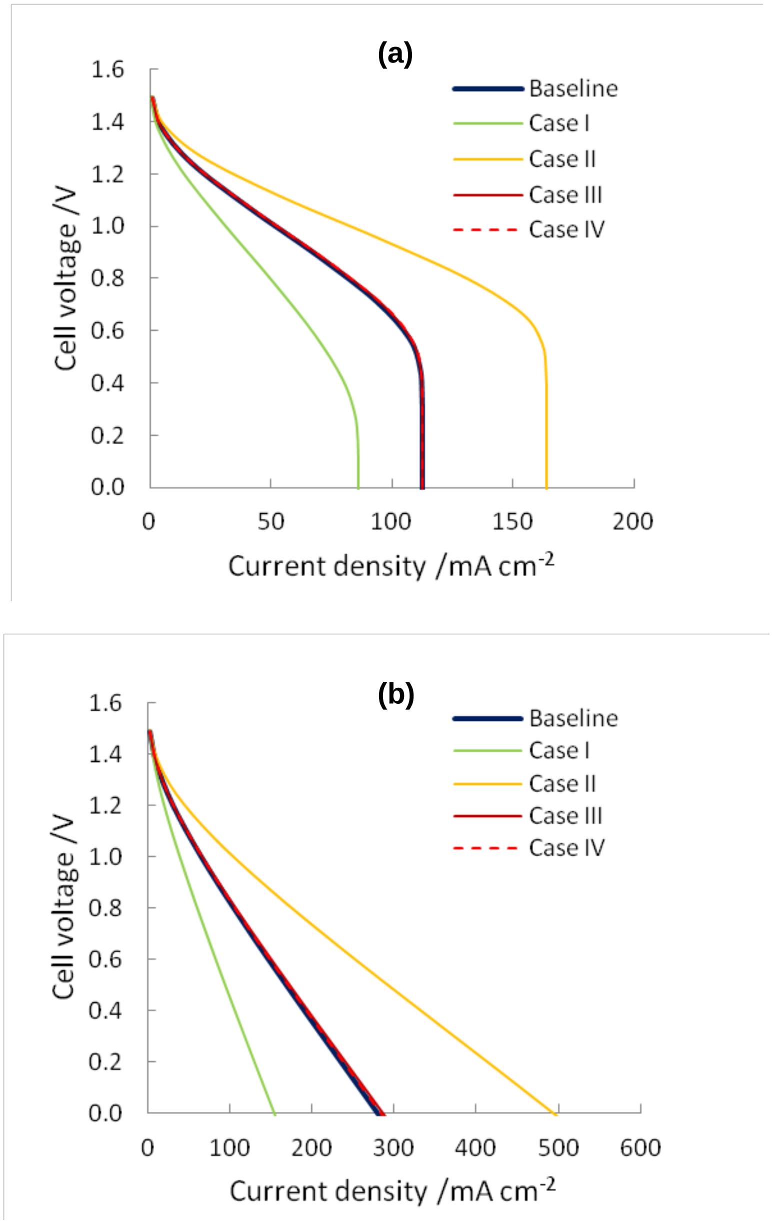

Figure 8. ***Polarization curves predicted by the model: (a) 10 μL min^{-1}; and (b) 300 μL min^{-1}.***

Note that Case I, II, III, IV refer to double width, half length, half center channel, and 2 contact, respectively.

across the center channel since the gap is reduced by half (from 1 mm to 0.5 mm). However, this effect does not make a substantial contribution in the cell performance.

The baseline, Case III (0.5 mm center channel), and Case IV (double contact) have the same electrode inlet area (see the red face in Figure 9) and therefore the velocity fields are almost identical at a given flow rate, resulting in the similar mass transport characteristics. This is especially true at the low flow rate when the mass transport of fuel/oxidant is the main limiting factor and leads to consistent polarization curves in all cases. The fuel utilizations for the three cases are also identical, as shown in Table 3, in support of this argument.

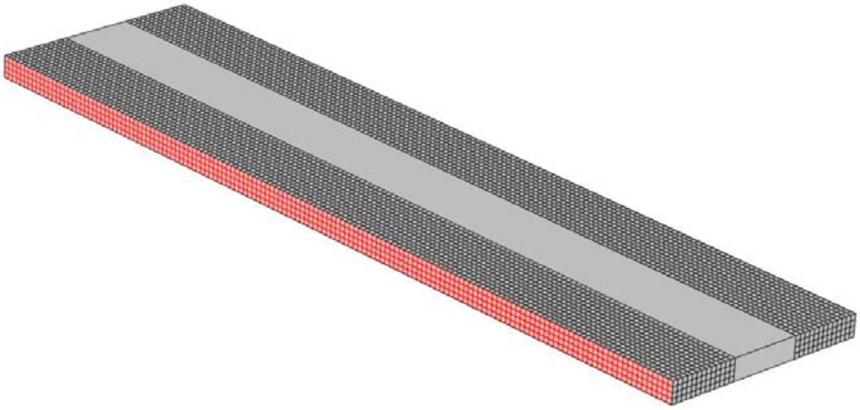

Figure 9. Two electrodes (anode and cathode) and center channel are shown with the cathode inlet colored in red.

Note that the drawing is exaggerated in z-direction for illustration purpose.

- According to Figure 8 (a), the Case I (double width) is expected to produce only a 53% increase in the total current compared to the baseline while its actual area is increased by a factor of 2. This corresponds to a 24% reduction in the limiting current density at 10 μL min^{-1}. In other words, the doubled active reaction area obtained by doubling the electrode width does not correspond to a proportional increase in fuel utilization. Indeed, the fuel utilization of Case I is 69.5% at the outlet of the electrode while the baseline case is 45.3% at 10 μL min^{-1} as shown in Table 3. There are two competing effects associated with increased electrode width: i) increased total current and net fuel utilization; and ii) reduced area-specific (normalized) current density and performance.

Table 3. Fuel utilizations calculated from the 2D model.

	Fuel utilization [%]	
	10 **μL min**$^{-1}$	300 **μL min**$^{-1}$
Baseline	45.3	7.7
Case I	69.5	13.8
Case II	33.1	5.1
Case III	45.3	7.7
Case IV	45.3	7.7

Note that the changes of the initial and final concentration of V(II) are divided by the initial concentration.

- For the Case II (half length cell), the total current produced is reduced by approximately 27% from the baseline at the low flow rate. However, the electrode area is also reduced by a factor of 2, resulting in a 46% net increase in the limiting current density at 10 μL min^{-1}. Since the electrode inlet area is reduced by half from the baseline, the average velocity at the electrode inlet is expected to be approximately doubled: 0.31 mm s^{-1} vs. 0.15 mm s^{-1} for the Case II and baseline, respectively (at 10 μL min^{-1}). Combined with the net surface area reduction, the higher local velocity and therefore the higher rate of convection enhance the mass transport limits, resulting in the 46% higher limiting current density.
- The contour plots of V(II) spatial concentration distribution obtained from the 2D model at the low flow rate are shown in Figure 10 for the baseline and Case I (double width) cells. Note that the plots are near the limiting current densities for both cases. The initial concentration of V(II) is 1.86 M (equivalent to 1860 mol m^{-3}) based on the actual measured concentration as discussed previously. Apparently, as the fuel (V(II)) flows through the porous electrode (anode, right side), its concentration decreases uniformly in the flow direction but does not reach zero.

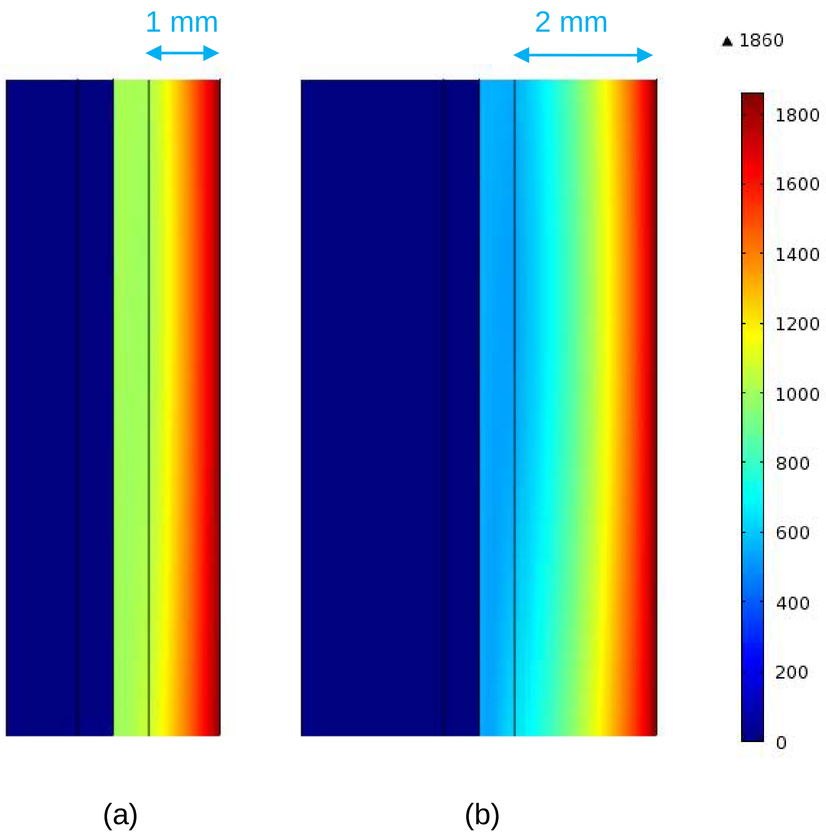

Figure 10. ***Contour plots of V(II) concentrations in [mol m^{-3}]: (a) Baseline; and (b) Double width cell (Case I) at 10 μL min^{-1}.***

Note that the averaged values along the inlet and the outlet of the anode are used to calculate the fuel utilizations listed in Table 3.

- For the high flow rate (300 μL min^{-1}), the trends are similar: a) the baseline, Case III, and Case IV have almost identical polarization curves, b) The magnitude of limiting current densities are the same order as 10 μL min^{-1} for Case I and Case II. However, the explanation for this is quite different. As one can see in Table 3, the fuel utilizations in general are much lower at 300 μL min^{-1}, indicative of predominant ohmic losses. Therefore, the velocity fields and convectional effects are less important while the ohmic resistances prevail instead. Consequently, the reduction of electrode length (Case II) causes a significant increase in the limiting current density: the net travel length for electrons in the longitudinal direction is reduced, which therefore lowers the overall ohmic resistance of the cell. The increase in width of the electrode (Case I) does not make a positive contribution in the cell performance. This is due to the increase of the ionic travel length in x-direction.
- For Case IV (Double Contact), the overall ohmic resistance inside the cell is almost the same as the baseline. The averaged travel distances are reduced by half but at the same time the currents are divided in a parallel setup, resulting in no noticeable benefits. It is concluded that increasing the number of electrical contacts is not preferable.

3.2.2. Measured Polorization Cuves

The polarization curves obtained from measured data are shown in Figure 11: (a) 10 μL min^{-1}, and (b) 300 μL min^{-1}. The key observations are:

- The mass transport losses are clearly observed at 10 μL min^{-1} while not seen at 300 μL min^{-1} as anticipated from the model.
- The overall performance trends for each parameter under investigation are in a fair agreement with the modeling results. However, significant discrepancies are observed in terms of the limiting current densities, especially at 300 μL min^{-1}. A possible explanation for this discrepancy lies in the treatment of external contact resistance. In all cases analyzed, an approximated value of 25 Ω (as the contact resistance) is added externally to the model. As demonstrated previously [13], the large variability of the contact resistance found experimentally dictates the initial slope in the polarization curves and ultimately determine the limiting current densities.

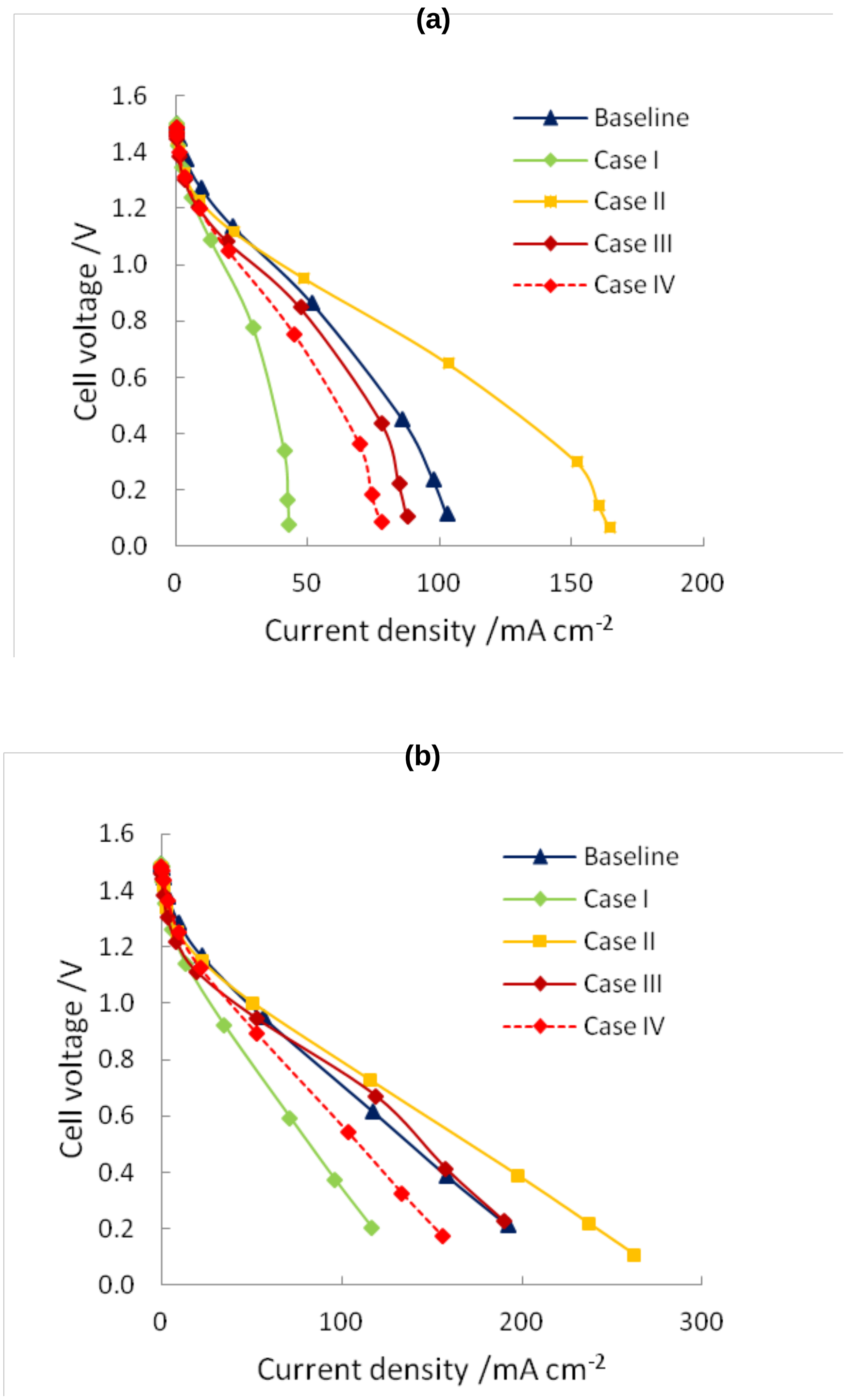

Figure 11. Polarization curves from measured data: (a) 10 μL min^{-1}; and (b) 300 μL min^{-1}.

Note that Case I, II, III, IV refer to double width, half length, half center channel, and 2 contact, respectively.

The uncertainty induced by the approximated value is more significant at 300 μLmin^{-1} due to the relatively high impact of overall ohmic resistance on cell performance.

- Another source of deviation is the actual dimensions of the fabricated cells. Since the carbon paper electrodes are cut manually using an in-house jig and aligned manually in the microchannel, significant human errors are expected. The actual measured dimensions listed in Table 2, such as the electrode width, the center channel gap, and the channel height, indicate the level of variability due to the fabrication process.

3.3. Conclusions

A parametric variation of microfluidic vanadium fuel cells with flow-through porous electrodes is studied both numerically and experimentally to provide guidelines for cell design and operation. The main findings of the current study are summarized below:

- Mass transport rates control the performance at low flow rates. The limiting current density can be increased at a given flow rate by reducing the electrode inlet area.
- Ohmic resistance controls the performance at high flow rates. Both current and power density can be increased by reducing the overall ohmic resistance in the longitudinal direction.
- Increasing the number of electrical contacts has only minor impact on the mass transport limit and ohmic resistance and consequently no major effect on cell performance.
- Narrowing down the center channel contributes a slight improvement at high flow rates due to reduced ohmic resistance but has no measureable impact on performance at low flow rates.
- In order to minimize the discrepancies between modeling results and measured data, detailed impedance measurements for the current cells are strongly recommended.

4.

4. Chip-embedded Thin Film Current Collector for Microfluidic Fuel Cells

In this chapter, a chip-embedded thin film current collector is discussed to mitigate the high contact resistance associated with the use of porous electrodes in microfluidic fuel cells. The proposed micromachining based thin film process is compatible with the overall cell fabrication and enables integration without substantial modification of the original cell design [13]. The main motivation of this work is to reduce the contact resistance of the cell by means of custom-designed, device-integrated current collectors that allows an increased number of contact points distributed across the length of the electrodes in close proximity to the reaction sites. Two different carbon paper materials as porous electrodes are investigated and tested, and cells with and without the current collectors are directly compared. In addition to regular performance measurements, an electrochemical impedance spectroscopy (EIS) study is conducted to analyze the voltage losses, impedance characteristics, and ohmic contributions of the cells. The experimental investigations are supported by numerical simulations using a three-dimensional computational model of the cells.

4.1. Methodology

4.1.1. Baseline Fuel Cell Architecture

The baseline design of the microfluidic fuel cell with flow-through porous electrodes considered in this work comprises two separate flow inlet ports and one common outlet port, as shown in Figure 2. The overall device architecture is consistent with the standard flow-through cell design previously developed by our group [13]. The fuel (V(II)) and oxidant (V(V)) are fed into the inlet ports and flowed through the porous electrodes that are inserted in the microfluidic channel.

4.1.2. Proposed Current Collector Design

The new microfluidic fuel cell concept introduced in this study comprises custom-designed thin film current collectors placed underneath the porous electrodes in order to increase the net contact areas and reduce the contact resistance. The cross-sectional device layout of the modified cell is compared to the baseline in Figure 12. The rectangular shaped current collectors are 23 mm long and 0.7 mm wide and designed to extend outward with square shaped pads (5 mm × 5 mm) at the ends on which external wires are soldered, as illustrated in Figure 13. The current collector width is intended to be narrower than the carbon electrode width (1 mm) in order to provide a one-to-one comparison without extending the active area of the electrodes. The porous electrodes are carefully aligned to cover the entire shape of the current collectors. Any highly conductive materials can be candidates for the current collector, as long as they are compatible with micromachining environments and acidic solutions.

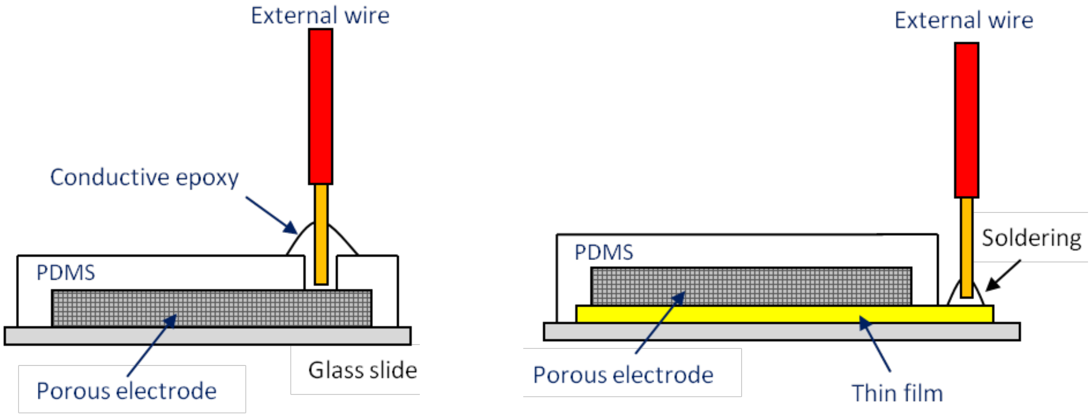

(a) (b)

Figure 12. ***Cross-sectional illustrations of: (a) baseline fuel cell; and (b) proposed fuel cell with thin film current collectors.***

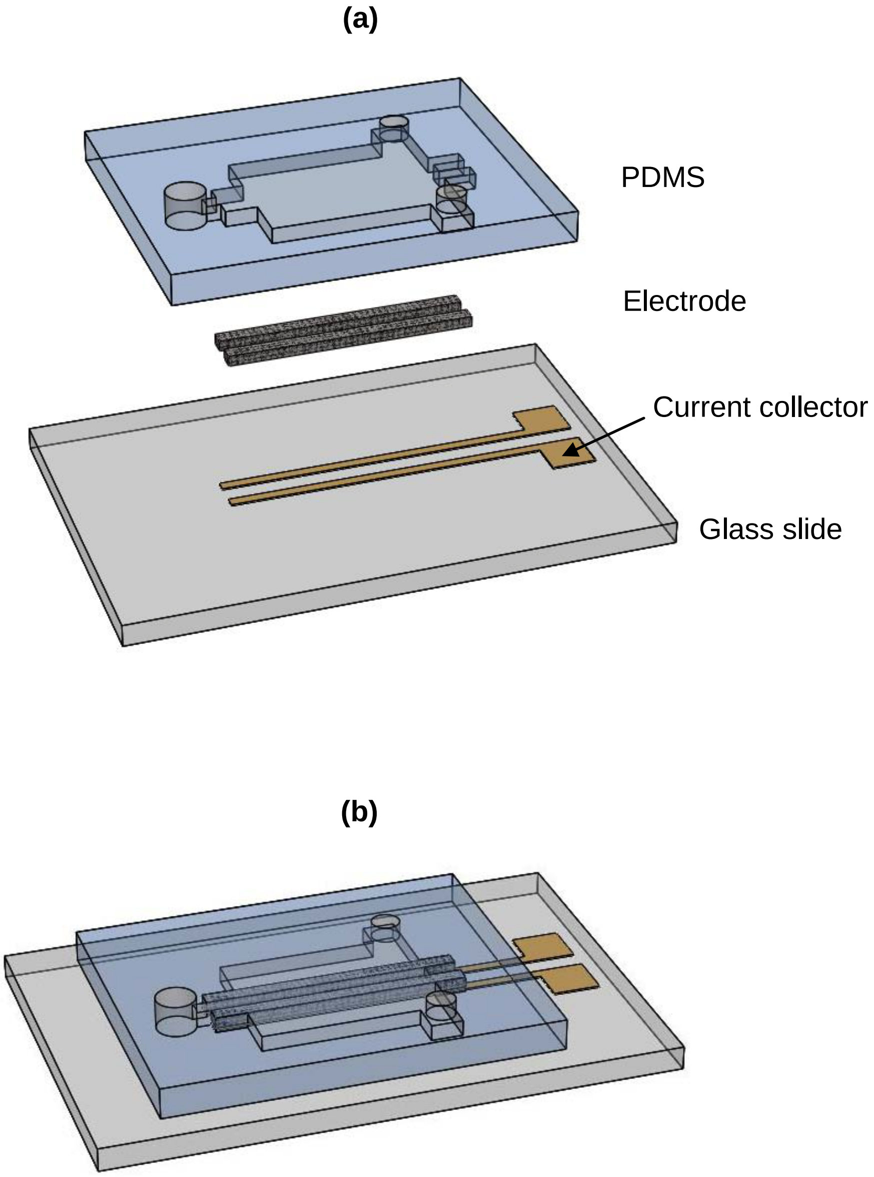

Figure 13. ***Schematics of: (a) exploded view of the parts; and (b) assembly of the proposed microfluidic fuel cell with thin film current collectors (not to scale).***

4.1.3. Microfabrication

The fabrication processes for both the baseline and current collector cells are based on a previously reported microfabrication procedure for microfluidic fuel cells with flow-through porous electrodes [13]. The processes for the two cells are identical except for the thin film process added prior to bonding the channel layer (PDMS) and substrate (glass slide). The PDMS channel layer is built by a well-established soft lithography technique [32]. In order to ensure multiple uses without delamination of the master from its substrate (Si wafer), an adhesion layer of SU-8 2100 (MicroChem) is coated, flood exposed without a mask, and fully cured. A 150 µm high master for the replica molding step is fabricated using the same SU-8. The master itself is formed by single coating and single exposure step with a transparency mask printed from a laser printer. A 10:1 mixture of polydimethylsiloxane (PDMS, Dow Corning) and its curing agent is poured and cured for over 48 hours at room temperature and finally peeled off from the mold. A hole punch of 0.095" OD (Technical Innovations Inc.) is used to create the fluidic inlet holes and 0.145" for the outlet hole. Porous carbon strips (20 mm long and 1 mm wide) are cut from sheets of Toray carbon paper (TGP-H-060) using an in-house jig and inserted into the microchannel grooves. After carbon paper is fitted in the channel, the PDMS microchannel structure is bonded onto a glass slide without sealants. Both the PDMS and glass slide bonding surfaces are functionalized by a Corona Treater (BD-20AC, Electro-Technic Products Inc.) for 45 seconds and followed by a physical contact. This corona treatment has been reported to activate chemical bonds for irreversible seals on the bonding surface [Haubert]. The sample is left overnight to ensure complete bonding.

4.1.4. Thin Film Process for Current Collector

A thin film of gold (Au) is chosen as the primary current collector material in this study due to its proven compatibility with acidic environments. Gold is highly conductive and widely used in the semiconductor industry. More importantly, the micromachining based Au thin film process is compatible with the overall cell fabrication and does not require a substantial modification of the original baseline design. A 3" × 4" microscope glass slide is cleaned with IPA and de-ionized water to remove any unwanted residues or particles. An e-beam evaporator (PVD 75, Kurt J. Lesker Co.) is used to deposit 10 nm thick chromium (adhesion layer), which is followed by 400 nm thick gold deposition. In order to pattern the obtained thin films, a masking photoresist (AZ 703) is coated and patterned using standard photolithography equipment, a mask aligner, and a wet bench. A transparency mask taped onto a glass plate is inserted into the aligner for UV exposure. The gold film is then wet-etched by a gold etchant followed by a chromium etching step and the masking photoresist is stripped by acetone. After the glass substrate with the patterned gold current collector is bonded to the PDMS microchannel layer (as described in Section 2.3), external wires are soldered onto the square pads at the end of the current collectors using a generic solder wire (60/40 Sn/Pb).

4.1.5. Porous Electrode Material

For the purposes of this work, two different carbon paper based materials are investigated and tested. The first one is a commonly employed carbon paper without hydrophobic coatings (TGP-H-060, Toray), which allows liquid electrolytes to fully saturate and flow through the pores with low capillary resistances. The second material is a carbon paper coated with a micro porous layer (MPL). Optically, it is almost identical to the Toray carbon paper on one side, while the other side (MPL side) has smoother morphological characteristics. The MPL is designed primarily for water management purposes in PEM fuel cells, and contains PTFE to obtain its desired hydrophobic properties. Note that the cell using standard carbon paper is denoted as “Current Collector I” (CC-I), while the MPL electrode cell is denoted as “Current Collector II” (CC-II). The measured heights of both electrode materials are approximately 180 µm.

4.1.6. Fuel Cell Testing

2 M vanadium electrolyte solutions are prepared from stock electrolyte in 4 M sulfuric acid base according to a previously described procedure [13]. The electrolyte concentrations tested in this work are 92% (equivalent to 1.84 M) or higher and the cells are operated at room temperature. The electrolyte flows are driven by a dual syringe pump (MA1 70-2209, Harvard Apparatus). The fluidic connections between the test device and syringes are achieved by forced fitting of Tygon tubing (R-3603). Polarization

curves are created during operation of the cells by measuring the voltage across external resistors directly connected with the electrical contacts of the cells, using 8 resistors ranging from 82 kΩ to 10 Ω [37]. The current generated by the cell is monitored until a steady reading is achieved (30 ~ 40 seconds, depending on the flow rate). Two flow rates (10 μL min^{-1} and 300 μL min^{-1}) are chosen to investigate a low and a high flow rate regime, respectively. The current density and power density in the polarization curves are based on the top surface area of each electrode. For fair comparison with the formerly reported fuel cell data, electrode volume specific parameters are also considered and discussed in section 4.2.2. Complete cell EIS (Electrochemical Impedance Spectroscopy) measurements are performed using an FRA (Frequency Response Analyzer) capable potentiostat (Reference 3000, Gamry Instrument). Nyquist plots are recorded at the open circuit cell voltage and at a flow rate of 100 μL min^{-1}, by applying an AC amplitude of 100 mV rms over the frequency range from 100 kHz to 10 Hz.

4.1.7. Numerical Model

A three-dimensional computational fluid dynamics (CFD) simulation is performed to investigate the flow distribution of the 150 μm channel height fuel cell, using a commercially available code, Fluent (ANSYS). The incompressible equations for continuity and momentum conservation are solved for the flow in the regions outside the porous electrodes, while the pressure drop across the porous electrodes is calculated using the well-known Darcy's law [25]. From a fluid dynamics point of view, the baseline and the current collector cells are considered identical since the thin film current collector is only 400 nm thick, i.e., less than 0.3% of the channel height. The density and viscosity of vanadium electrolyte are specified as working fluid properties. For porous media, a porosity value under compression (ε_c) is calculated from [38]:

$$\varepsilon_c = \frac{\varepsilon_o - c}{1 - c} \qquad (14)$$

where ε_o is the uncompressed porosity and c is the linear compression ratio given by:

$$c = 1 - \frac{t_c}{t_o} \tag{15}$$

Assuming a constant electrode thickness (t_o = 180 μm, measured) and a uniform channel height (t_c = 148.3 μm, measured), the linear compression ratio is 0.176 and the porosity value under compression is approximately 0.73. The parameters and material properties specified in the simulation are listed in Table 4. A mesh independence study is performed and a mesh size of 333,500 elements is selected.

Table 4. Parameters and material properties used in the numerical simulation.

Quantity	Symbol	Value	Unit	Source
Volumetric flow rate	Q	10 and 300	μL min^{-1}	Measured
Electrode length	L	12	mm	Designed
Electrode width	W	1	mm	Designed
Center channel width	w_c	1	mm	Designed
Electrolyte density	ρ	1,200	kg m^{-3}	[25]
Electrolyte viscosity	μ	0.008	Pa s	[25]
Electrode thickness	t_o	180	μm	Measured
Channel height	t_c	148.3	μm	Measured
Porosity	ε_o	0.78		[39]
Compressed porosity	ε_c	0.73		Calculated
Permeability	K	1.28×10^{-11}	m^2	[40]
Viscous resistance	K^{-1}	7.8×10^{10}	m^{-2}	[41]
Inertial resistance	$R_{inertial}$	1.08×10^{5}	m^{-1}	[41]

4.2. Results and Discussions

In this work, a chip-embedded thin film current collector is proposed to mitigate the relatively large contact resistances previously reported for microfluidic fuel cells with porous electrodes [13, 25]. To demonstrate this novel concept, vanadium fueled flow-through microfluidic fuel cell prototypes with three different electrode structures are fabricated and tested: a carbon paper cell without current collector (baseline), a carbon paper cell with current collector (CC-I), and a micro porous layer coated carbon paper cell with current collector (CC-II). The two cells with current collectors are both expected to enhance the electrical contact with the porous electrodes, while the MPL coated carbon paper (CC-II) had a smoother surface intended to further promote the physical contact area. The SU-8 master and the obtained microchannel height are carefully monitored during fabrication to minimize any uncertainty associated with height variations. A slight compression of the electrode is intended for ensuring a solid and uniform contact between the electrode and the current collector to compensate channel height variations, if any. In addition, non-uniform flow distributions from unwanted flow short-cuts over or under the porous electrodes are eliminated. The measured dimensions of the master and the three cells are listed in Table 5. The volume specific current/power densities are calculated using the measured height data combined with the actual electrode widths. It is noteworthy that all three cells discussed in this paper are fabricated from the same master and therefore had identical channel heights.

Table 5. Measured master height and electrode widths of the three fuel cell prototypes.

	Master height [μm]	Electrode width (anode/cathode) [mm]		
		Baseline	CC-I	CC-II
Position 1	144.5	1.048/1.023	1.027/1.072	1.020/0.980
Position 2	148	1.048/1.000	1.029/1.047	1.038/0.980
Position 3	152.5	1.038/0.990	1.042/1.010	N/A
Average	148.3	1.024	1.038	1.004

4.2.1. Flow Distribution

To assist in the evaluation of the new current collector cells, the flow distribution of the proposed microfluidic fuel cell architecture is first simulated using the three-dimensional numerical framework detailed in section 4.1.7. The cell geometry used in the simulations is ideal in the sense that the channel height and compressed electrode thickness are uniform (150 μm), as desired. The pressure distribution in the mid-plane of the cell at 10 μL min^{-1} flow rate is shown in Figure 14. The pressure contours within the porous electrode are almost parallel with the long edges of the electrodes and relatively dense, implying that the major pressure drops occurred across the electrodes, which contributed 43.7% of the total pressure drop from inlet to outlet. The pressure drop across the porous electrodes is validated by Darcy’s law with a fairly good agreement (less than 10% deviation). The pumping power required to maintain the flow rates is calculated by [25]:

$$P_{power} = 2\,\Delta P \times Q \tag{16}$$

where ΔP is the simulated pressure drop across the cell and Q is the volumetric flow rate. The calculated pumping power for 300 μL min^{-1} is 2.02×10^{-2} mW, merely 0.4% of the expected power output of the fuel cell. For 10 μL min^{-1} operation, the required pumping power is even less.

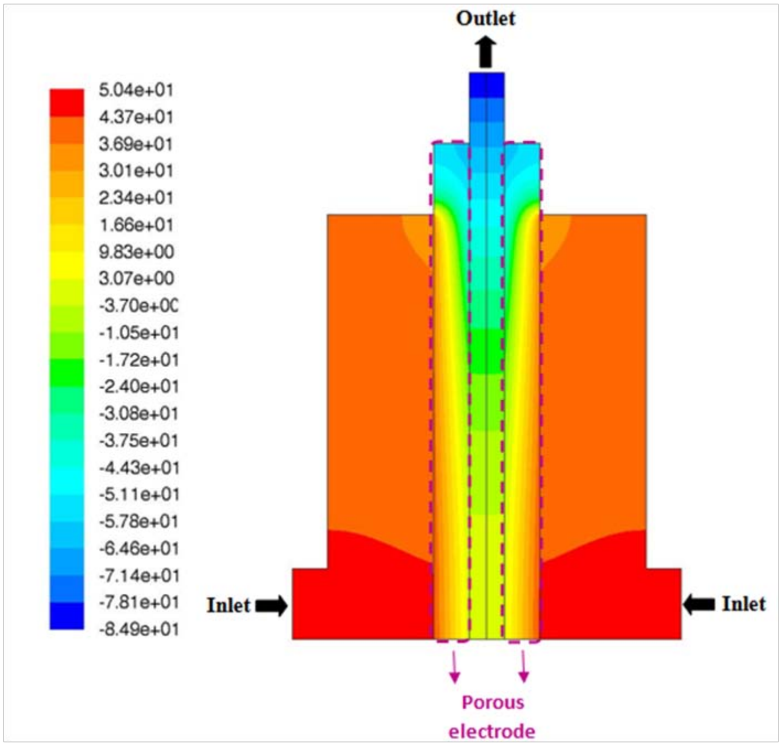

Figure 14. ***Pressure contours at the mid-plane of the fuel cell obtained by numerical simulations at 10 μL min^{-1} flow rate (unit: [Pa]).***

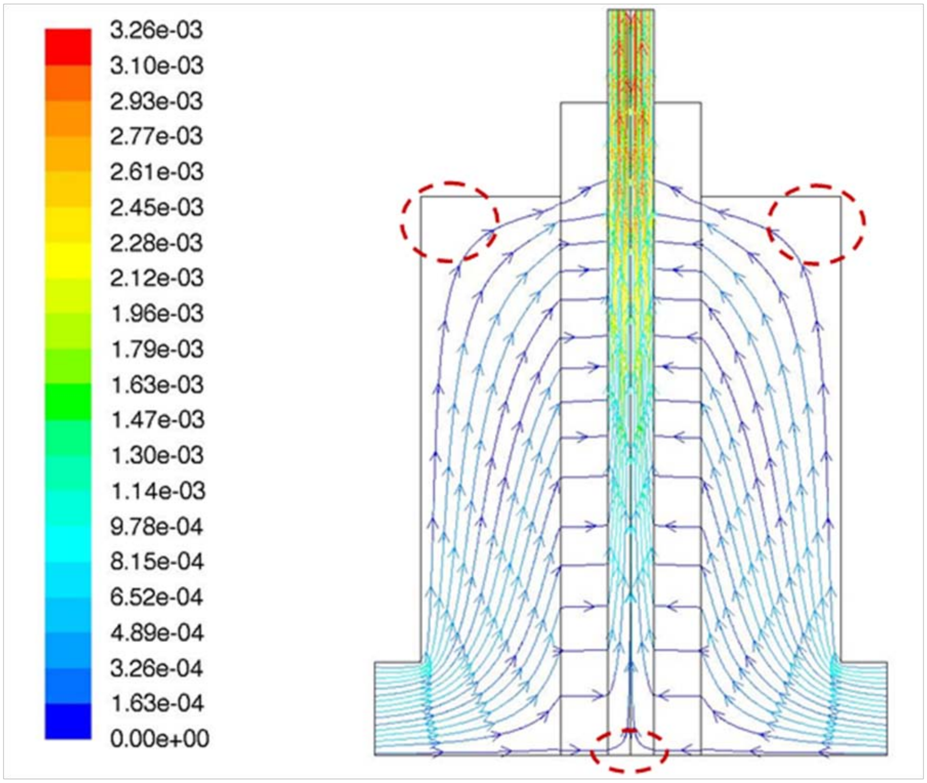

Figure 15. Pathlines colored by velocity magnitudes in the mid-plane of the fuel cell obtained by numerical simulations at 10 μL min^{-1} (Unit: [m s^{-1}]).

Note that the dashed ovals indicate stagnation zones.

Figure 15 shows a pathline plot colored by velocity magnitudes in the cell at 10 μL min^{-1} flow rate. The velocity magnitudes in the center channel increased gradually towards the outlet, indicating that the mixing width between the fuel and oxidant streams actually *decreased* along the center channel due to the convectional effects [25]. Another important observation is that the electrolytes entered the porous electrodes orthogonally, where the velocity magnitude is only about 5% of the maximum velocity in the center channel due to the relatively large cross-sectional area in the orthogonal direction compared to that of the center channel. Thus, the flow in the porous electrodes is expected to be uniform while mixing in the center channel is minimized. The calculated maximum Reynolds numbers near the cell outlet are 0.0145 and 0.437 for 10 μL min^{-1} and 300 μL min^{-1}, respectively. In addition, the dashed ovals in Figure 15 indicate stagnation regions where the electrolyte streams become stagnant at near zero velocities. The overall findings of the flow simulations are consistent with our visual observations during operation of the cells, which indicates that the actual flow distribution in the cells is indeed uniform, as anticipated.

4.2.2. Polarization and Power Density

4.2.2.1. Effect of Current Collector

This section presents a direct comparison of the measured polarization curves for the baseline microfluidic fuel cell and the equivalent cell with chip-embedded thin film current collector (denoted as CC-I). As mentioned, the baseline and CC-I cells have identical channel dimensions (approximately 148 μm high) since they are built from the same master mold and identical porous electrodes originating from the same sheet of carbon paper material; thus, the only notable difference between these two cells is the presence of the thin film current collector in CC-I. The comparison of polarization curves for both cells is shown in Figure 16. At the low flow rate (10 μL min^{-1}) in Figure 16 (a), the tail of the polarization curves gradually dropped, which is indicative of a mass transport limited performance. Since the fuel cell operation is dominated by fuel/oxidant supply rates, the gain from reducing contact resistances is marginal: the peak power density is increased by 25% from 37.6 to 47.1 mW cm^{-2}. For 300 μL min^{-1}, as shown in Figure 16 (b), the performance improvements attributed to the embedded current collectors are much greater, since the polarization is primarily controlled by the combined ohmic cell resistance at high flow rates [27]. It is noteworthy that the voltage loss associated with ohmic resistance is proportional to the current density, and therefore becomes more significant during operation at high flow rates where higher currents are obtained.

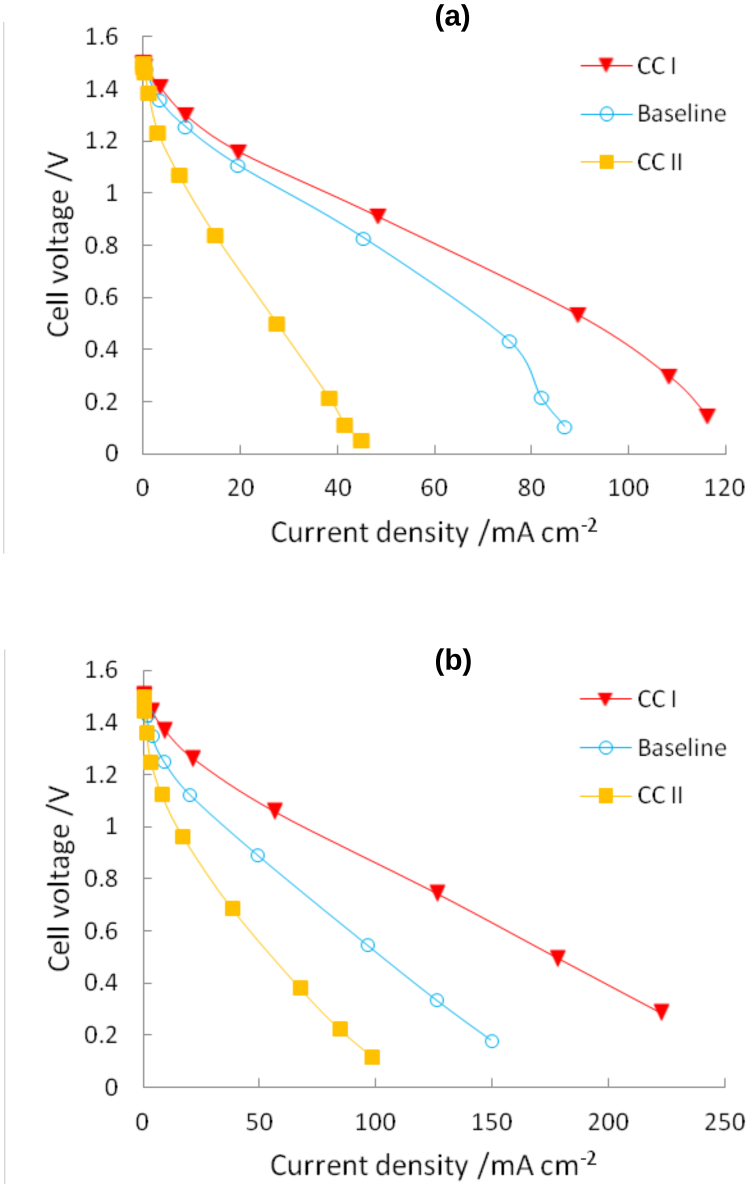

Figure 16. ***A comparison of polarization curves for the current collector I (CC-I), baseline, and current collector II (CC-II) cells: (a) 10 μL min^{-1}; and (b) 300 μL min^{-1}.***

Figure 17 shows the power density comparison for 300 μL min^{-1}. The peak power density is improved from 52 to 93 mW cm^{-2} by adding current collectors, corresponding to a 79% net increase. For fair comparison with the formerly reported fuel cell data, electrode volume specific parameters are also considered, as presented in Figure 17 (b). The measured channel height and electrode widths from Table 5 are multiplied by the length (12 mm) to calculate the total electrode volumes for each cell used for volumetric normalization of current and power. The CC-I cell achieves a volume specific peak power density of 6.2 W cm^{-3}, which is to the authors' knowledge the highest microfluidic fuel cell performance published to date. It compares favorably to the baseline cell of this study (3.5 W cm^{-3}) and the previously reported record of 4.37 W cm^{-3} with 300 µm thick electrodes, normalized from 131 mW cm^{-2} [13]. Three CC-I cells are built and tested on different days and the maximum deviation in the polarization curves is less than 3.5%.

The improvements in cell polarization attributed to the current collectors are mainly featured by a net reduction in the overall slope of the curve. While the slope of a polarization curve represents the combined effect of activation overpotentials, mass transport, and overall cell resistances, the slope in the central, linear portion is commonly dominated by ohmic voltage losses that are proportional to the current density [27]. In our case, since the electrolytes, their supply rates, and electrode dimensions are considered identical for both cells, we assumed that the activation overpotentials and mass transport losses are the same and that the only contribution toward the net slope changes is attributed to a contact resistance decoupled from the combined loss.

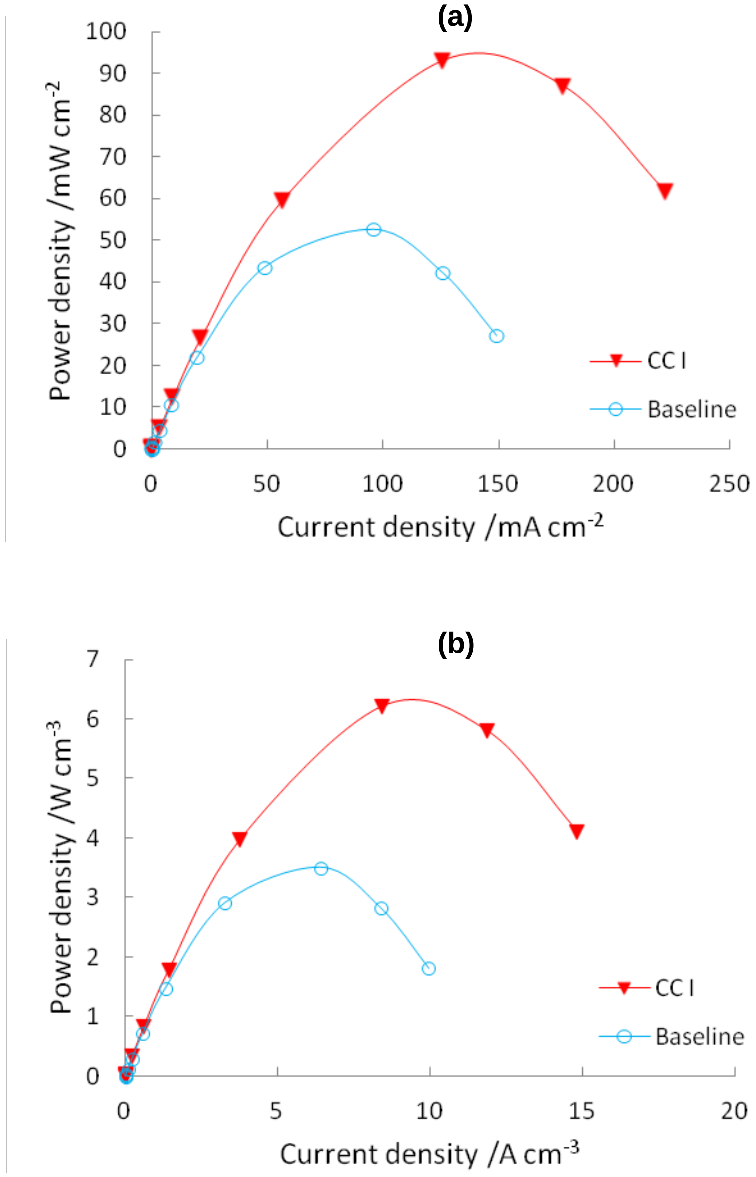

Figure 17. ***Power density of the baseline and current collector I (CC-I) cells at 300 μL min^{-1} flow rate: (a) area specific power density curves [mW cm^{-2}]; and (b) volume specific power density curves [W cm^{-3}].***

Figure 18 presents the slopes of the two polarization curves at 300 µL min^{-1}, calculated by a linear fitting method. The baseline slope is 0.0071 (absolute value), while the CC-I curve had a slope of 0.0047, which indicated a 34% reduction in slopes. It is worthwhile to mention that this 34% slope decrement had a positive effect on both the overall cell currents by means of reduced ohmic resistance and the overall cell potential by means of reduced ohmic voltage loss, resulting in a 79% combined improvement in peak power density.

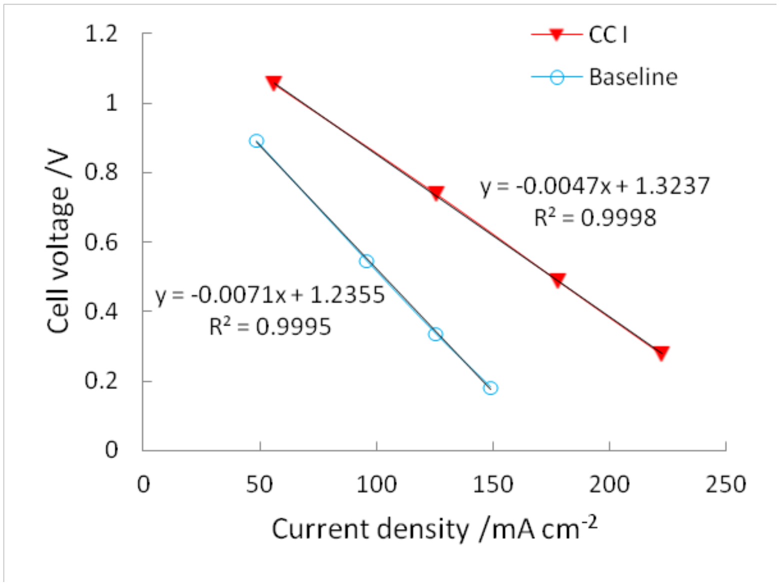

Figure 18. Linear fits to the central part of the polarization curves of the baseline and first current collector cells measured at 300 µL min^{-1}.

4.2.2.2. Effect of Micro Porous Layer

The second current collector cell built and analyzed in this study (denoted as CC-II) has the same channel dimensions as the baseline and first current collector cell (CC-I). The unique aspect of CC-II is that its electrodes are made of micro porous layer (MPL) coated carbon paper. Since the MPL side has much smoother surface, more surface area for contacts could be available and therefore less contact resistances to the thin film current collectors are expected. However, the measured performance of the CC-II cell is even lower than that of the baseline, as demonstrated by the orange polarization curves in Figure 16. We believe that the hydrophobic nature of the polytetrafluoroethylene (PTFE) coating included in this electrode material caused incomplete saturation of the porous medium, resulting in non-uniform flow distribution and reduced utilization of active reaction area. In addition, it is suspected that the PTFE coating had a negative impact on the through-plane conductivity and contact resistance and thereby hindered electron transfers to the current collector. Our EIS measurements (to be discussed in the following section) support this argument.

4.2.2.3. Overall Cell Resistance Measurements

In order to measure the overall ohmic cell resistances including contact resistances, a well-known technique in electrochemistry, Electrochemical Impedance Spectroscopy (EIS), is adopted. Figure 19 shows an equivalent circuit representation of the complete microfluidic fuel cell system. The superscripts *A* and *C* denote anode and cathode, respectively.

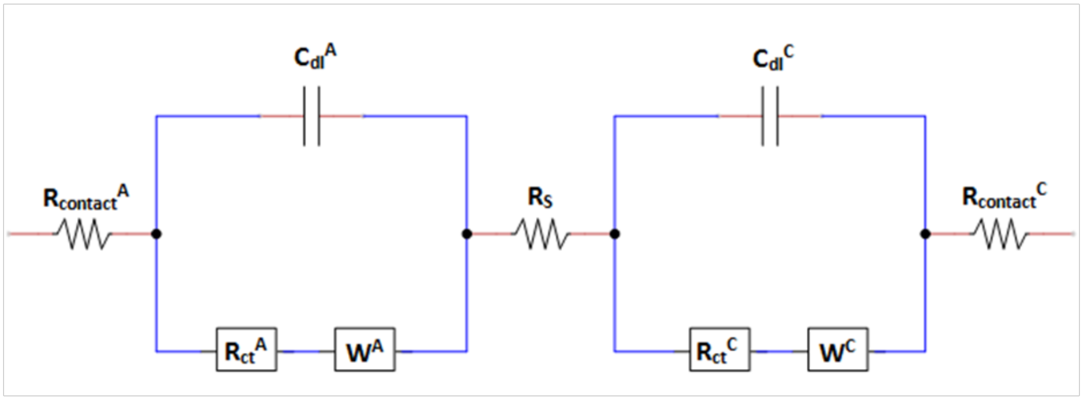

Figure 19. ***EIS-based equivalent circuit representation of the microfluidic fuel cell [42].***

Double layer capacitances are labeled as C_{dl}, while R_{ct} represents a charge transfer or Faradaic resistance. The contact resistances between the electrodes and external wires are $R_{contact}$, while R_s stands for a combined ionic resistance from solution and electronic resistance from electrodes. Warburg impedance is denoted as *W*, which represents diffusion and mass transport resistances. At high frequency excitations, the double layer impedance is very low and short circuits the charge transfer branch. This implies that the first real-axis intercept point in the Nyquist plot from EIS measurements indicates the sum of R_s and $R_{contact}$. On the other hand, at low frequencies, the double layer impedance is large and the current flows mostly through the charge transfer branch, resulting in a more complex combination of all the resistances: $R_{contact}$, R_s, R_{ct}, and W [42]. For the purpose of the current study, the high frequency impedances (R_s and $R_{contact}$) are compared to quantify the changes in contact resistances between cells.

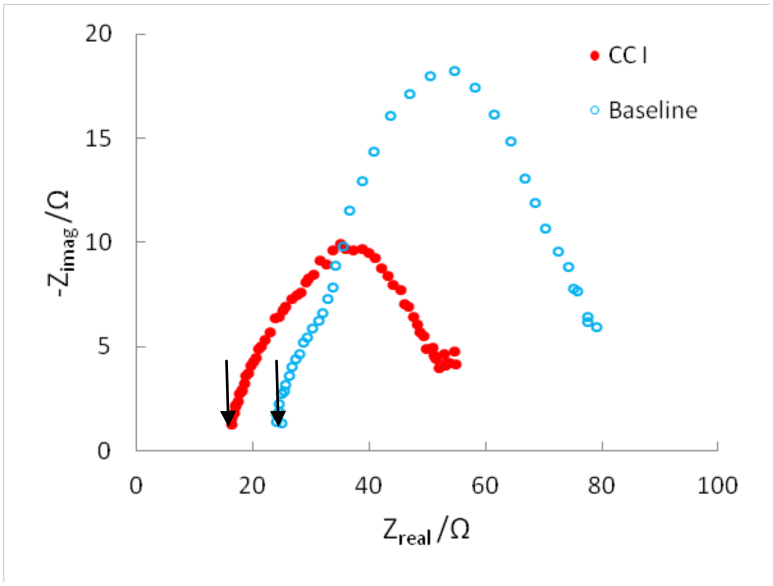

Figure 20. ***Nyquist plots measured by EIS of the baseline and first current collector (CC-I) cells.***

Note that the arrows point to the high frequency real-axis intercepts used to determine the overall ohmic cell resistance.

Figure 20 shows a comparison of Nyquist plots from EIS measurements obtained for the baseline and CC-I cells. For the baseline cell, the sum of R_s and $R_{contact}$ value is 24.5 Ω, while the corresponding value for the CC-I cell is 16.6 Ω, i.e., 7.9 Ω lower than the baseline cell. The net decrement of 7.9 Ω can be interpreted as the net reduction of contact resistances by the current collector, since the only difference between the two cells is the addition of the current collectors in CC-I. The electrolytes and carbon paper electrodes are identical and the geometrical dimensions are the same for both cells, except for a minor variation in electrode widths of 2%. Therefore, the net contact resistance decrement of 7.9 Ω indicates a 32% (out of 24.5 Ω) decrease in overall ohmic cell resistance. This result is in good agreement with the net polarization curve slope reduction of 34%, as described in section 4.2.2.1, and effectively results in a 79% increment in power density. The measured value for CC-II is approximately 30 Ω, which verifies that the PTFE component has a negative impact on the through-plane conductivity and contact resistance, and consequently the overall performance of the cell.

4.3. Conclusions

In this work, a chip-embedded thin film current collector for vanadium fueled microfluidic fuel cells with porous electrodes is proposed, fabricated, and tested. Two porous electrode materials are investigated: i) carbon paper for the baseline and first current collector (CC-I) cells; and ii) micro porous layer (MPL) coated carbon paper for the second current collector (CC-II) cell. Compared to the baseline, the current collectors incorporated in the CC-I cell results in a peak power density improvement from 52 to 93 mW cm^{-2}, corresponding to a 79% net increase. This drastic performance boost is attributed to a net decrement of 7.9 Ω in contact resistances, quantified by a negative shift in the high frequency impedance measured by EIS. The reduction in overall ohmic cell resistance associated with the current collectors is comparable to the net reduction in polarization curve slope in the central, linear portion of the curve. The CC-I cell achieved a volume specific peak power density of 6.2 W cm^{-3}, which compares favorably to all previously reported microfluidic fuel cell devices.

A carbon paper coated with an MPL is also evaluated as a potential strategy to enhance the contact area and uniformity of the porous carbon / current collector interface in the CC-II cell. The overall performance of CC-II is however found to be substantially lower than that of the baseline. Provided that the MPL-coated carbon paper contained a significant amount of PTFE as a structural binder and hydrophobicity agent, we expect that the electrode does not wet completely, resulting in reduced utilization of active reaction area and non-uniform flow distribution inside the electrodes. The PTFE coating is also verified to have a negative impact on the through-plane electrical conductivity of the bulk paper as well as the electrical contact resistance at the porous carbon / current collector interface. We anticipate that non-PTFE treated porous media with smoother surfaces would be a more suitable choice in this context.

5. Electrochemical Characteristics of Vanadium Redox Reactions on Porous Carbon Electrodes

In this chapter, the electrochemical characteristics of the vanadium redox reactions are investigated on commonly used porous carbon paper electrodes and compared to a standard solid graphite electrode as baseline. Half-cell electrochemical impedance spectroscopy is applied to measure the overall ohmic resistance and resistivity of the electrodes. Kinetic parameters for both V(II) and V(V) discharging reactions are extracted from Tafel plots and compared for the different electrodes. Cyclic voltammetry techniques reveal that the redox reactions are irreversible and that the magnitudes of peak current density vary significantly for each electrode. The obtained kinetic parameters for the carbon paper are implemented into a numerical simulation and the results show a good agreement with measured polarization curves from operation of a microfluidic vanadium redox fuel cell employing the same material as flow-through porous electrodes. Recommendations for microfluidic fuel cell design and operation are provided based on the measured trends.

5.1. Introduction

An in-depth fundamental understanding of the electrochemical characteristics of the vanadium redox reactions is essential for further development of such microfluidic fuel cell devices. There is extensive literature available for large-scale vanadium redox batteries employing the same set of reactants [43, 44]. It was late 1970s when the NASA-Lewis Research Center was involved in the development of a complete redox energy storage system based on Fe(III)/(II) and Cr(III)/(II) couples [20, 21]. They also conducted an initial screening of a large number of redox couple/electrode combinations including V(II)/V(III). Vanadium (symbol is V and atomic number is 23) is a hard, silvery gray, ductile and malleable transition metal. A significant swell of research activities in this area was spurred by the discovery of an unusually high cycle efficiency obtained with this redox couple [22, 23]. The electrochemical behavior of the V(II)/V(III) redox couple on glassy carbon electrodes was first investigated by Dr. Skyllas-Kazacos' research group at University of New South Wales [22]. The oxidation/reduction rates (k^o) at pH 4 were experimentally obtained and a general trend in k^o with pH was observed. A positive half-cell with V(IV)/V(V) at glassy carbon and gold electrodes was investigated by the same group [23]. It was claimed that the electrochemical behavior was strongly dependent on the surface preparation of the glassy carbon electrode. Later, the vanadium electrolyte stability in sulfuric acid solution was studied at various temperatures and at different compositions [45]. A H_2SO_4 concentration of 3 ~ 4 M was found to be more stable and suitable due to higher electrolyte conductivity. The diffusion coefficient of V(IV) with graphite electrodes was experimentally estimated by Zhong et al. [46]. For V(IV) oxidation, the exchange current density (i_o) and transfer coefficient (α) were also obtained. More recently, Gattrell et al. [24] examined a detailed kinetic mechanism of the V(V)/V(VI) redox couple in acidic aqueous solutions. A multistep of electrochemical-chemical-chemical reactions was analytically modeled with varying pH and vanadium concentrations. The analytical model was compared with experiments in which a rotating disk graphite electrode was used and showed a good agreement at various pH levels and concentrations of vanadium. The standard rate constants for vanadium redox species at a pyrolytic graphite and a plastic formed carbon (PFC) were experimentally determined by Yamamura et al. [47].

As mentioned, while some kinetic and diffusion parameters are available in the literature for conventional scale vanadium redox batteries, no studies have been performed to date on the specific electrode materials employed for vanadium redox based microfluidic fuel cells. Moreover, most previous investigations were focused on planar electrodes such as rotating disk electrodes and did not consider porous carbon electrodes. The objective of the current work is to investigate the electrochemical characteristics of the vanadium redox reactions on carbon based electrodes commonly employed in microfluidic fuel cells. The following three materials are considered: (i) graphite rod; (ii) carbon paper; and (iii) wet-proofed carbon paper. The emphasis is on the porous carbon paper electrodes and their performance advantages in relation to the solid graphite rod electrode. The carbon paper (ii) is physically employed in a vanadium redox fueled microfluidic fuel cell configuration and the cell performance is compared with a numerical simulation in which newly obtained kinetic parameters are specified.

5.2. Methodology

5.2.1. Electrode Materials

A graphite rod, which is used here as a solid baseline electrode, and two porous carbon based materials are investigated and characterized experimentally. The graphite rod is a cylindrical mechanical pencil lead with 0.58 mm diameter (Pentel, C505). The first porous carbon material is a commonly employed carbon paper without hydrophobic components (TGPH-060, Toray), which allows liquid electrolytes to fully saturate and flow through the pores with low capillary resistances. The second porous material is a carbon paper immersed in 19% wt. of polytetrafluoroethylene (PTFE, also known as Teflon) that attributes hydrophobic properties and is primarily used for water management purposes in polymer electrolyte fuel cells. This wet-proofed carbon paper is intended to examine the influence of wettability on its electrochemical behavior. As indicated by the SEM images of the two porous carbon materials shown in Figure 21, their structures are almost identical, exhibiting a compactly fused electrically conductive fibrous matrix with a range of microscale pores open to the flow of electrolyte. Moreover, a conformal layer of PTFE is observed in the wet-proofed carbon paper in Figure 21 (b).

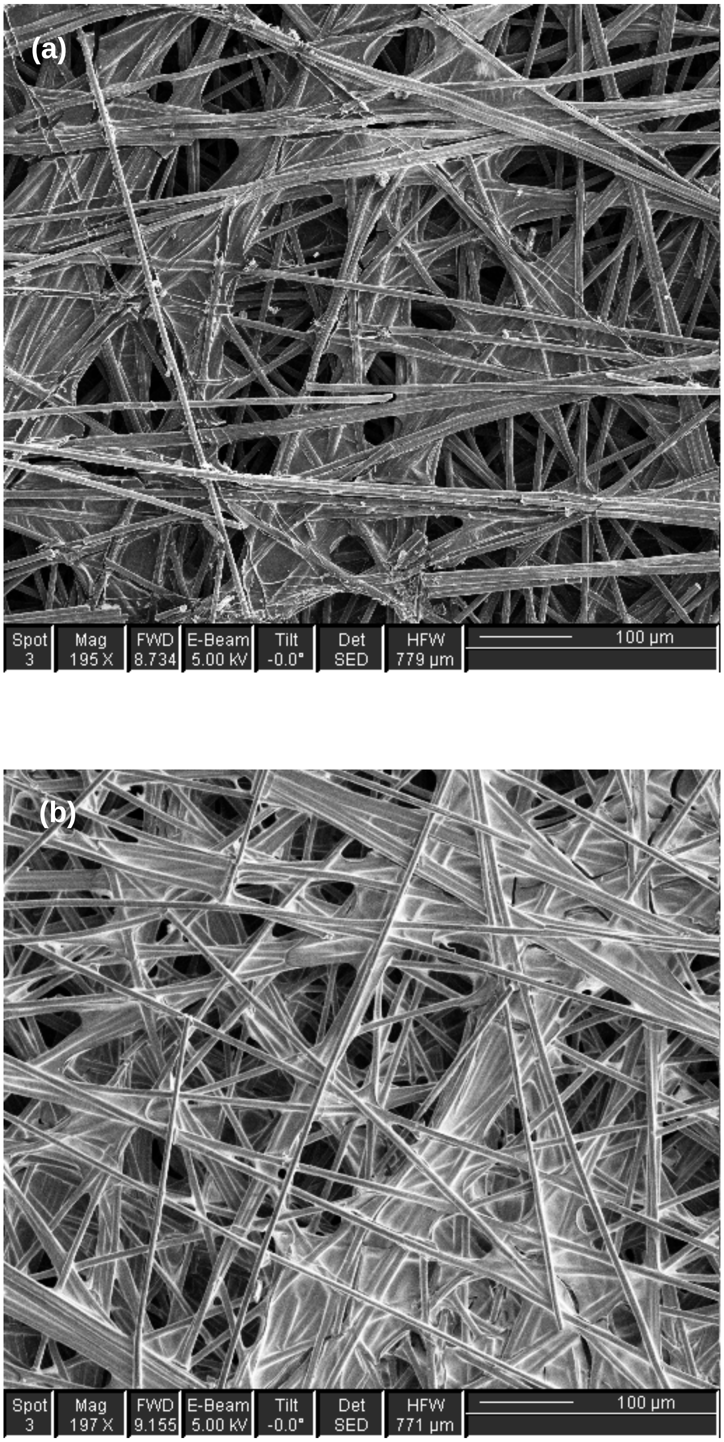

Figure 21. Scanning electron micrographs of the two porous carbon papers studied in this work: (a) regular carbon paper; and (b) wet-proofed carbon paper with 19% wt. PTFE.

5.2.2. *Vanadium Redox Electrolytes*

Microfluidic vanadium redox fuel cell operation is based on the following anodic and cathodic reactions at 298 K [28]:

$$V^{3+} + e^{-} \rightleftarrows V^{2+} \qquad E^{o} = -0.496\,V\,vs.SCE \tag{17}$$

$$VO_2^{+} + 2H^{+} + e^{-} \rightleftarrows VO^{2+} + H_2O \qquad E^{o} = 0.750\,V\,vs.SCE \tag{18}$$

2 M vanadium redox electrolyte solutions are prepared from stock electrolyte in 4 M sulfuric acid base according to a previously described procedure [13]. The solution (50/50, V(III)/V(IV)) is recharged by an in-house charger [33] to produce V(II) and V(V) that are used as anolyte and catholyte, respectively. In the present study, oxidation of V(II) to V(III) is of interest at anode side, while reduction of V(V) to V(IV) is examined at cathode side. The electrolyte concentrations tested in this work are 92% (equivalent to 1.84 M) or higher and the measurements are taken at room temperature.

5.2.3. *Electrochemical Cell Experiments*

For the main electrochemical study in this work, a simple, low-cost, standard three-electrode electrochemical cell configuration is assembled. The three carbon based electrodes in this experiment are prepared as the stationary working electrode: (i) 18mm long, 0.58 mm diameter graphite rod; (ii) and (iii) 18 mm long, 1 mm wide, and 0.18 mm thick carbon paper and wet-proofed carbon paper, respectively. The carbon paper dimensions are intended to be identical to the size of the porous electrodes used in the microfluidic fuel cell previously developed in our group [48]. Toothless alligator clips are used to connect these carbon electrodes with electrical leads for data acquisition and control. As the counter electrode, a graphite plate (10 × 20 × 3 mm) is cut to ensure a much larger surface area than the working electrode. All the electrode potentials including the open circuit potential (OCP) are measured against a saturated calomel electrode (SCE, Fisher Scientific). The electrolytes are agitated by a magnetic stirrer (Corning, PC-220) which is located 3 cm away from the working electrode at the bottom of the container to minimize mass transport limiting effects. The rotational speed dependence is evaluated prior to the main experiments. As shown in Figure 22, a significant jump in electrical currents is observed from stirring speed 0 to 380 rpm, indicative of mass transport limited case. At 380 rpm or higher, the current response is almost saturated without a noticeable change in output, and therefore, an optimal speed of 380 rpm is finally chosen. In order to minimize unwanted oxidation of V(II) in ambient air, the container is sealed (PARAFILM) and nitrogen is continuously purged during experiments. For V(V) measurements, the sealing and nitrogen purge are not required, as V(V) does not oxidize with oxygen in the air.

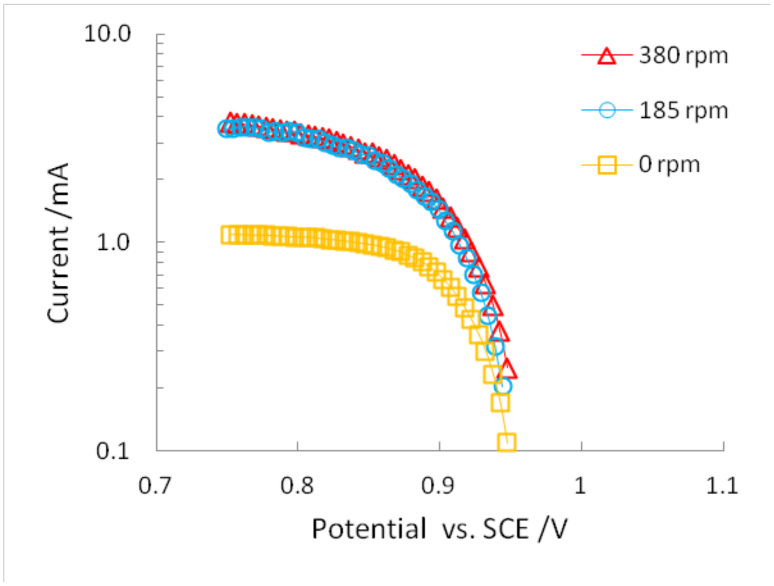

Figure 22. ***Raw data of stirrer rotational speed dependence for V(V) reduction on regular carbon paper at no rotation, 185 rpm, and 380 rpm.***

A frequency response analyzer (FRA) capable potentiostat (Reference 3000, Gamry Instruments) is utilized to control and operate the electrochemical cell measurements, including half-cell EIS, Tafel, and CV measurements as detailed in the following subsections. For EIS and CV experiments, the agitation is removed to impose a pure diffusion condition. The current densities reported in the Tafel and CV analyses are calculated based on the submerged geometrical surface area of the electrodes. All measurements are repeated at least three times to ensure that the results are repeatable and consistent.

5.2.3.1. Half-cell Electrochemical Impedance Spectroscopy

The overall ohmic resistance of each electrode material is determined by half-cell electrochemical impedance spectroscopy (EIS). In the EIS measurements, a small sinusoidal perturbation potential is applied to the electrode-electrolyte interface, and the resulting amperometric response is recorded [Schmickler]. For the purpose of this study, the first real-axis intercept points, denoted as R_s, at the highest frequency for each carbon electrode are measured in V(V) solution with AC amplitude of 10 mV rms over the frequency range from 100 kHz to 10 Hz (at OCP ≈ 0.956 V vs. SCE). The resistivity value of the carbon paper is calculated from the obtained R_s values using Ohm's law and its dimensions (18 × 1 × 0.18 mm).

5.2.3.2. Tafel Analysis

Tafel curves serve as a primary tool in analyzing and quantifying the electrochemical kinetics of the vanadium redox reactions on the three selected carbon electrode materials. Fabjan et al. [29] reported experimentally that a single electron transfer was the rate determining step in the vanadium redox kinetics. Several earlier modeling efforts [30, 31] of vanadium redox batteries also confirmed that the cell performance was adequately captured by the Butler-Volmer equation. The two main assumptions made for this experimental study are listed below:

- The vanadium redox reactions are assumed to be outer-sphere reactions. All solvation shells in the reactant species are intact and only electron transfer reactions are of interest.
- Uniform distributions of reactants and well-stirred solutions are assumed. Therefore, mass transport limitations are neglected, i.e., the rate of convection and diffusion from bulk to surface is much faster than the reaction rates, and bulk and surface concentrations are equal.

For large overpotentials (η > 80 mV), the Tafel curve, where logarithm of current densities are plotted against η, yields a straight line [42]. If η is positive (oxidation of V(II)), the simplified Butler-Volmer equation can be written as:

$$log_{10}(j) = log_{10}(j_o) + \frac{\alpha F}{2.3RT}\eta \tag{19}$$

When η is negative (reduction of V(V)), the alternate exponential term in the Butler-Volmer equation is negligible and this leads to:

$$log_{10}(|j|) = log_{10}(|j_o|) - \frac{(1-\alpha)F}{2.3RT}\eta \tag{20}$$

In the present study, a linear sweep voltammetry at a slow, constant scan rate of 0.1 mV s^{-1} is employed to create the Tafel plots. The overpotential range of 0 ~ 200 mV is chosen to ensure that the linear region can be adequately observed in the Tafel plots. Using these Tafel plots and Equations (19-20), the charge transfer coefficient α can be extracted from the slope of the linear regression line and the exchange current density j_o from the y-intercept point with the ordinate of the linear fit.

5.2.3.3. Cyclic Voltammetry

Cyclic voltammetry (CV) is used in this study to investigate the reversibility of the vanadium redox kinetics and the diffusion characteristics of vanadium redox species in solution. The peak current density j_p and scan rate v is related by [49]:

$$j_p = (2.99 \times 10^5)\alpha^{0.5} c_o^{bulk}\, D_o^{0.5}\, \nu^{0.5} \tag{21}$$

where c_o^{bulk} is the bulk concentration of reactant species and D_o is the diffusion coefficient. With measured j_p, c_o^{bulk}, and v, Equation (5) is used in this study to estimate the diffusion coefficients of V(II) and V(V).

For V(V)/V(IV) in this study, sweep rates of 10, 50, and 100 mV s^{-1} are selected within a potential range of 0.4 ~ 1.5 V; and for V(II)/V(III), 5, 10, and 50 mV s^{-1} with a potential range of -1.1 ~ -0.02 V are used. Prior to the CV measurements, the open circuit potential is measured to identify the equilibrium point for the two electrolytes: 0.96 V for V(V)/V(IV) and -0.57 V for V(II)/V(III). As mentioned, the V(II)/V(III) cell is properly sealed during the test to minimize its unwanted oxidation in the air.

5.2.4. *Microfluidic Vandium Redox Fuel Cell*

A microfluidic fuel cell with flow-through porous electrodes [13], incorporating regular carbon paper as electrodes, is fabricated and operated using vanadium redox electrolyte to evaluate the electrochemical characteristics of the vanadium redox reactions in situ during fuel cell operation and compare to the electrochemical cell measurements. As reported previously by our group [13, 16, 48], the microfluidic vanadium redox fuel cell with flow-through porous electrodes consists of two separate flow inlet ports and one common outlet port as illustrated schematically in Figure 2 (Chapter 1). The fuel, V(II), and oxidant, V(V), solutions are fed into the inlet ports and directed through the porous electrodes embedded in the microfluidic channel. Carbon paper is cut and inserted as porous electrodes with active dimensions of 12 × 1 × 0.18 mm. Fuel cell polarization curves are measured as described previously [48] at a flow rate of 10 μL min^{-1}.

5.2.5. Numerical Simulation

A numerical simulation of microfluidic fuel cell operation is conducted to link the fuel cell performance measurements to the parameters extracted from the electrochemical cell measurements. This simulation is based on a comprehensive numerical model previously developed and customized by our group for the flow-through porous electrode architecture [25]. The numerical model for the fuel cell in this study is based on conservation of mass, momentum, species, and charge coupled with electrochemical kinetics using a commercially available multiphysics software package (COMSOL Multiphysics 4.0a). In short, the pressure drop across the electrodes is calculated using Darcy’s law, while the incompressible equations for continuity and momentum conservation are used for the flow in the non-porous regions [34]. The governing equations for species conservation and charge conservation in the carbon paper electrode and electrolyte are solved simultaneously. A simple electron transfer reaction is assumed and the complete Butler-Volmer equation, including surface to bulk concentration ratio terms, is solved to estimate the charge transfer current densities corresponding to the redox reactions [26, 27]. The rate of vanadium species transported to and from the electrode surface through the combined effect of convection and diffusion is estimated by an empirical relationship for mass transfer in carbon fiber electrodes [36]. Further details about the numerical model are available in reference [25], which was recently published by our group.

5.3. Results and Discussions

Electrochemical cell measurements are conducted in V(II) and V(V) vanadium redox electrolyte using three different carbon materials as working electrode: (i) graphite rod; (ii) regular carbon paper; and (iii) wet-proofed carbon paper. The emphasis is on the two porous carbon paper electrodes and their performance compared to the solid graphite rod electrode. Experimental results from impedance testing, Tafel analysis, and cyclic voltammetry are reported and key observations and trends are discussed. Measured performance data are also provided for a vanadium redox fueled microfluidic fuel cell device, which employs (ii) regular carbon paper as electrodes, and compared with a numerical simulation in which newly obtained kinetic parameters are specified.

5.3.1. Half-cell Impedance Analysis

The ohmic resistance of each electrode material is estimated by half-cell electrochemical impedance spectroscopy (EIS) in V(V) solution. The first real-axis intercept point (R_s) in the obtained Nyquist plot is recorded as the combined ohmic resistance, which includes contact, solution, and electrode resistances. In order for fair comparison between the three carbon electrodes, all conditions are carefully controlled during the measurements, including electrolyte concentration, electrode dimension, and electrical connection. Therefore, the contact and solution resistances are constant, and the net differential values between the different electrodes can be used to compare their resistive properties. If assumed the sum of contact and solution resistances to be approximately 1 Ω and subtracted from the measured R_s, then the net electrode resistances (R_{net}) are: 1.7 Ω, 6.1 Ω, and 12.2 Ω for graphite rod, regular carbon paper, and wet-proofed carbon paper, respectively. Regular carbon paper, comprising a highly porous, low-density network of carbon fibers through which electrons are conducted, is found to have 4.4 Ω higher ohmic resistance than the graphite rod and thus significantly lower electrical conductivity. The resistivity of the regular carbon paper calculated using the net electrode resistance and its dimensions is 6.1×10^{-3} Ω cm, which is in good agreement with the manufacturer's specification of 5.8×10^{-3} Ω cm [39]. The resistivity values of the graphite rod and the wet-proofed carbon paper are estimated to 2.5×10^{-3} Ω cm and 12.2×10^{-3} Ω cm, respectively (Figure 23).

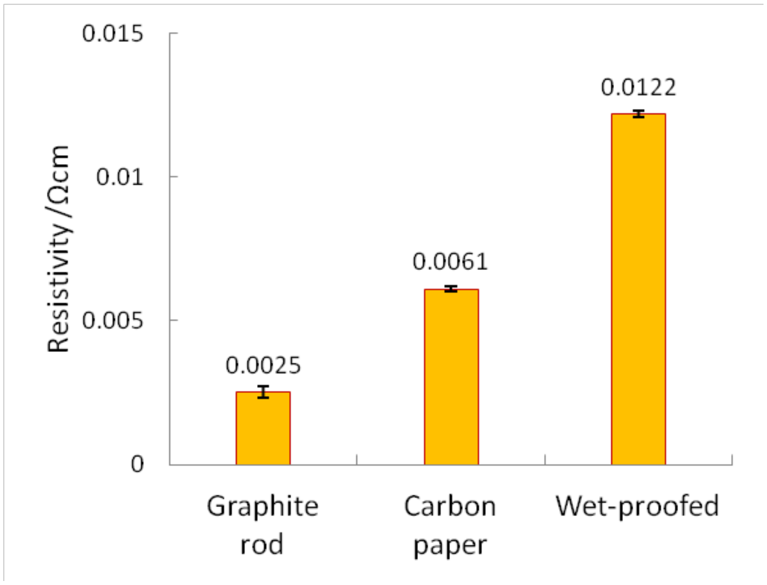

Figure 23. ***Net resistivity values of the three carbon electrodes estimated from half-cell EIS.***

Furthermore, the wet-proofed carbon paper is found to have almost five-fold higher resistivity than the graphite rod, and double the resistivity of the bare carbon paper. It is anticipated that the non-conductive Teflon component introduces a negative impact on the through-plane conductivity and contact resistance present in these measurements as well as in actual fuel cells, which is consistent with a complete fuel cell EIS measurement reported previously by our group [48]: the total resistance of a cell with wet-proofed electrodes was 81% higher than the baseline cell which employed regular carbon paper. On the device level, these results indicate that regular carbon paper is preferred to wet-proofed media and support the application of embedded current collectors to mitigate the reduced conductivity of the porous media and overcome their intrinsic ohmic overpotentials [48].

5.3.2. Kinetic Parameters from Tafel nalysis

A comprehensive Tafel analysis is conducted in both V(II) and V(V) solutions to determine the electrochemical kinetic parameters of the vanadium redox reactions with respect to the three carbon electrodes. The results are provided in Figure 24 for (a) V(V)

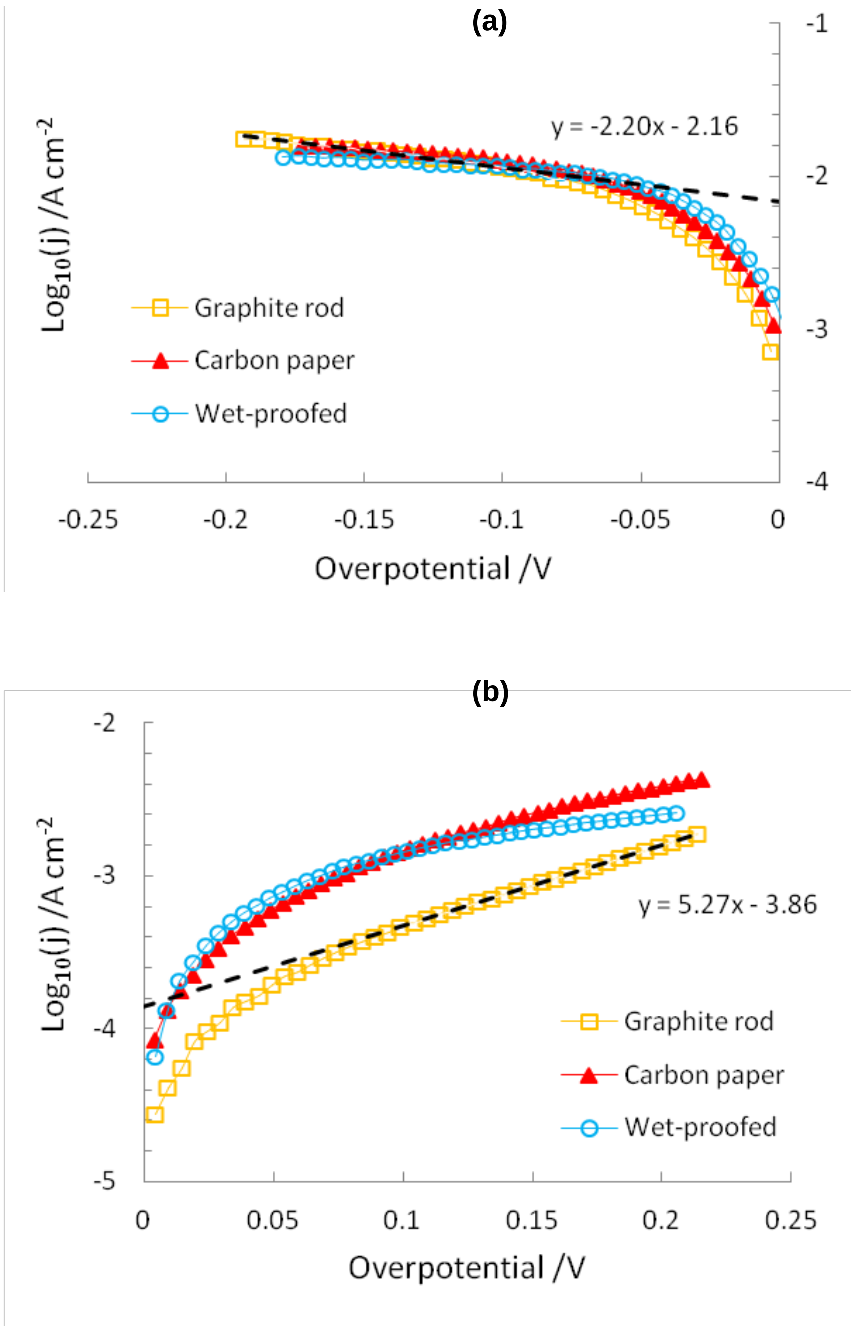

Figure 24. ***IR compensated Tafel plots for the three electrodes materials: (a) V(V) reduction; and (b) V(II) oxidation.***

Note that the linear regression lines for the graphite rod are shown by dashed lines with corresponding equations.

reduction and (b) V(II) oxidation. The kinetic and ohmic overpotentials are decoupled in the Tafel plots by *IR* compensation of the overall ohmic resistances, R_s, measured in the previous section. The actual impact of the *IR* compensation is negligible for the graphite rod and the regular carbon paper electrodes due to the relatively low ohmic resistances; however, for the wet-proofed carbon paper having the highest ohmic resistance, *IR* compensation is essential in order to obtain accurate kinetic parameters. The main observations from the *IR* compensated Tafel plots in Figure 24 are summarized below:

- In general, V(V) reduction kinetics are faster than V(II) oxidation on all three carbon electrodes under study: the y-intercept points of V(V) in Figure 24 (a) are one order of magnitude higher than those of V(II) in Figure 24 (b). This trend is consistent with literature data obtained for solid glassy carbon electrodes in similar electrolytes [22, 23, 50].
- For V(V) reduction in Figure 24 (a), the graphite rod and two porous carbon electrodes produce very similar Tafel curves, while for V(II) oxidation the graphite rod electrode shows notably lower current densities and therefore slower kinetics than the two porous carbon electrodes. This trend is confirmed by repetitive tests on three different days. Overall, porous carbon paper provides faster V(II) and V(V) kinetics than solid graphite electrodes, which is advantageous for microfluidic fuel cell integration.
- The influence of PTFE treatment on the electrochemical kinetics is negligible for both V(V) and V(II) reactions. Therefore, depending on whether hydrophilic or hydrophobic electrode is required, either regular non-treated or PTFE-treated paper, respectively, can be chosen accordingly without compromising the vanadium redox kinetics. For microfluidic fuel cells with flow through configuration, the regular non-treated carbon paper is generally beneficial since it allows liquid electrolytes to fully saturate and flow through the pores with low fluidic resistances.

The exchange current density j_o and charge transfer coefficient α are determined by the y-intercept and slope of the Tafel curves in Equations (19-20), followed by rate constant (k_o) calculation [42]. The charge transfer coefficients α for each electrode material are shown in Figure 25, where the average and standard deviation of three repeated measurements are reported.

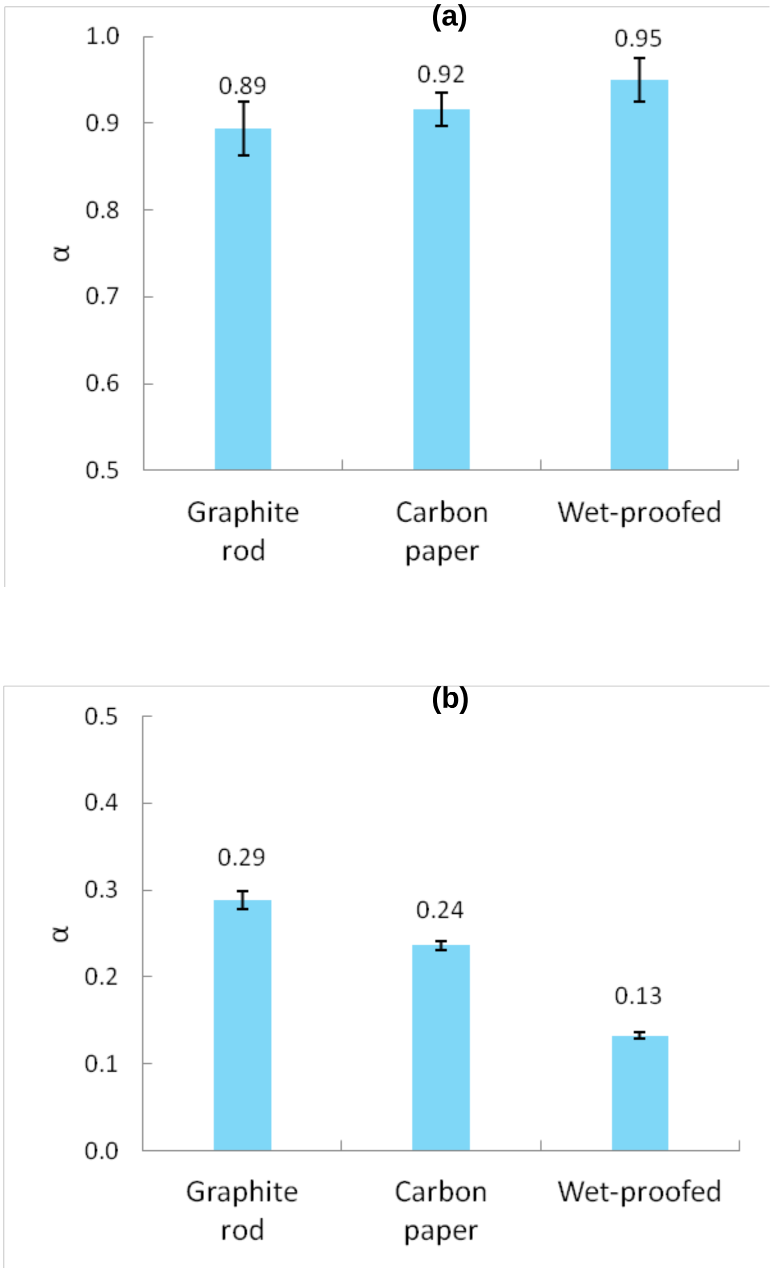

Figure 25. ***Charge transfer coefficients (α) determined from Tafel plots for the three electrode materials: (a) V(V) reduction; and (b) V(II) oxidation.***

For V(V), the *α* values for all three electrodes are close to 0.9 with relatively high degree of variability while for V(II) the values are ranging from 0.1 (wet-proofed paper) to 0.3 (graphite rod), thus indicating that both V(V) reduction and V(II) oxidation under present conditions are highly asymmetric reactions. The notably low α value for V(II) oxidation on the wet-proofed electrode can also be seen in Figure 24 (b) where the linear region slope of the wet-proofed electrode is lower than the others.

The estimated rate constants k_o from the Tafel curves are shown in Figure 26 for (a) V(V) reduction and (b) V(II) oxidation. As already observed in Figure 24, the general trend is that the exchange current densities and therefore the values of k_o are higher for V(V) than those for V(II). More quantitatively, the k_o values in Figure 26 (a) for V(V) are approximately one order of magnitude higher than in Figure 26 for V(II). Therefore, the rate determining half-cell reaction for vanadium redox fuel cell operation is V(II) oxidation, which is used as anode for the microfluidic fuel cells developed in our group. This is contrary to conventional PEM fuel cells where cathodic oxygen reduction is the rate determining half-cell, which is generally much slower than the rapid hydrogen oxidation at the anode. It is also noteworthy that the two porous electrodes offer a 3-4x improvement in V(II) oxidation rate constant compared to the graphite rod.

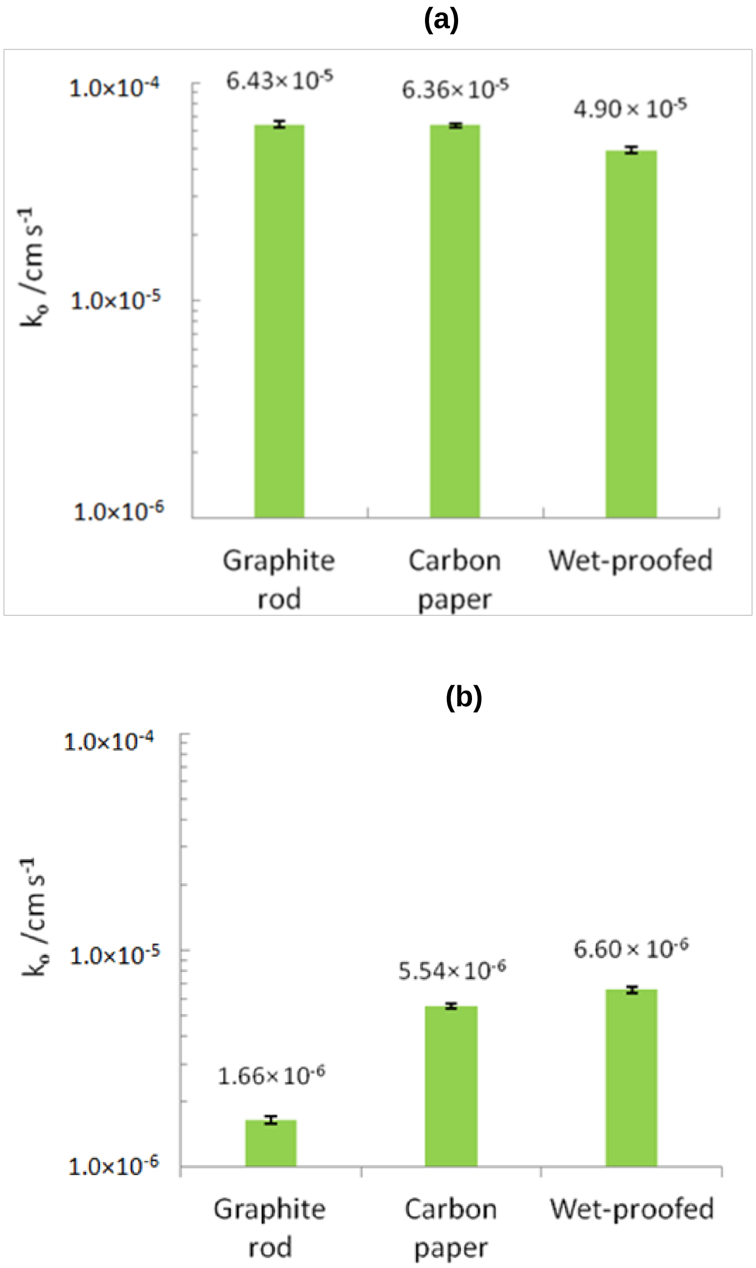

Figure 26. ***Estimated values of rate constants (k_o) extracted from Tafel plots: (a) V(V) reduction; (b) V(II) oxidation.***

5.3.3. Cyclic Voltammetry Analysis

Cyclic voltammetry (CV) is conducted to investigate the reversibility of the V(V)/V(IV) and V(II)/V(III) redox reactions on the three carbon electrodes. The obtained *IR* compensated voltammograms are presented in Figures. 27-29 for graphite rod, regular carbon paper, and wet-proofed carbon paper, respectively. The key observations are:

- While the Tafel curves are very similar for all three electrodes especially for V(V) reduction, the CV curves for each electrode show significant variations, in terms of the magnitude and location of peak current densities.
- In general, the peak potentials for all three electrodes are found to depend on the natural logarithm of scan rate and the peak separations, i.e., the potential difference between anodic and cathodic peaks, are much greater than 57 mV, which are two consistent indications of irreversible redox reactions. Furthermore, the peak separations of V(V)/V(IV) are narrower than those of V(II)/V(III). For example, the peak separation of V(V)/V(IV) with the graphite rod in Figure 27 (a) is 200-300 mV, while for V(II)/V(III) in Figure 27 (b) is around 800 mV. This tendency indicates that V(II)/V(III) redox chemistry is more irreversible than for the V(V)/V(IV) couple, and therefore has slower kinetic rates, which is consistent with the observations in the Tafel analysis in the previous section.
- While the V(V)/V(IV) reactions produce distinctive peaks in all cases, it is notable that no significant peaks are observed for V(II)/V(III) reactions on the two porous carbon electrodes in the present potential range. It is anticipated that the V(V)/V(IV) reactions in Figures 28 (a) and 29 (a) are mass transport limited, resulting from the relatively high kinetic rates found in the Tafel analysis. On the other hand, the V(II)/V(III) reactions in Figures 28 (b) and 29 (b) are expected to be mainly limited by slow kinetics.

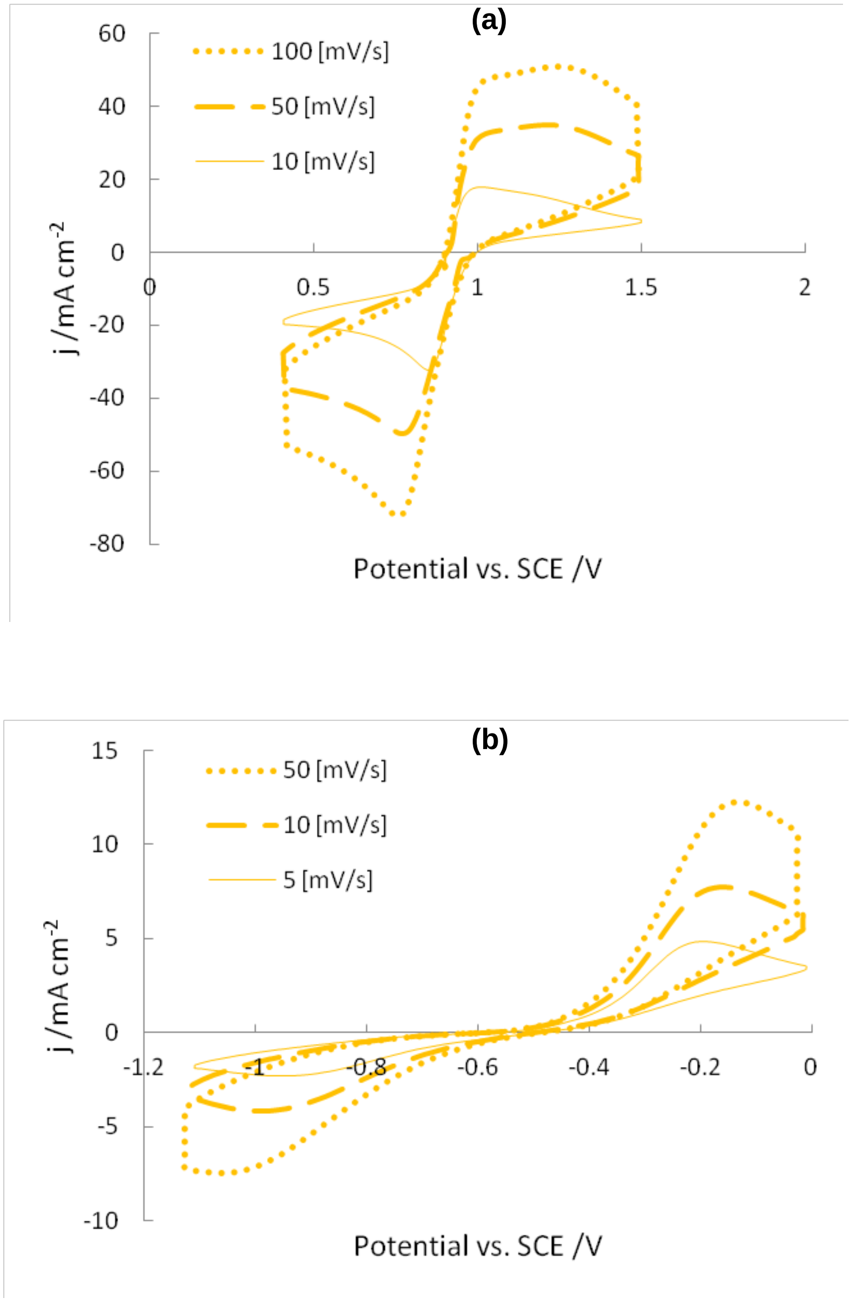

Figure 27. ***IR compensated cyclic voltammograms at the graphite rod in: (a) V(V)/V(IV); and (b) V(II)/(VIII).***

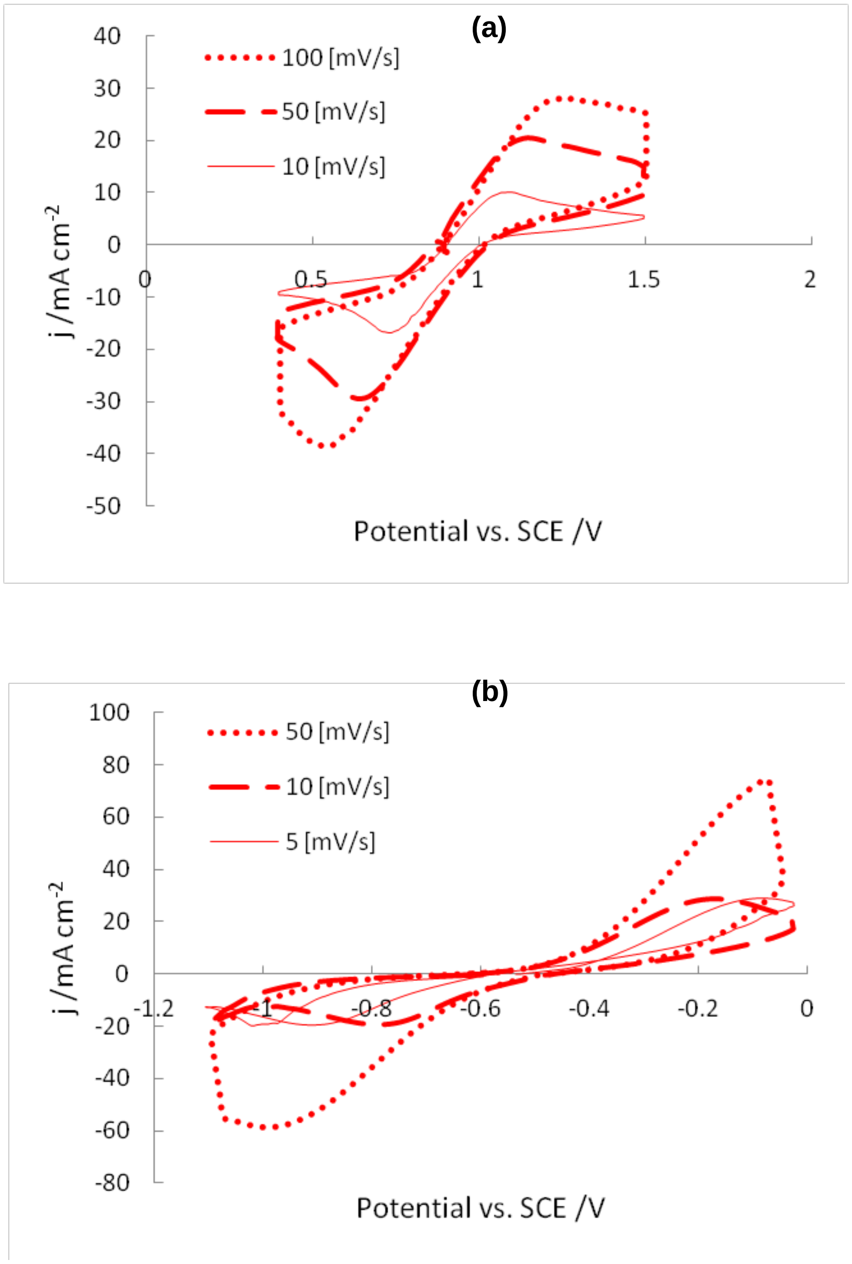

Figure 28. ***IR compensated cyclic voltammograms at the regular carbon paper in: (a) V(V)/V(IV); and (b)V(II)/V(III).***

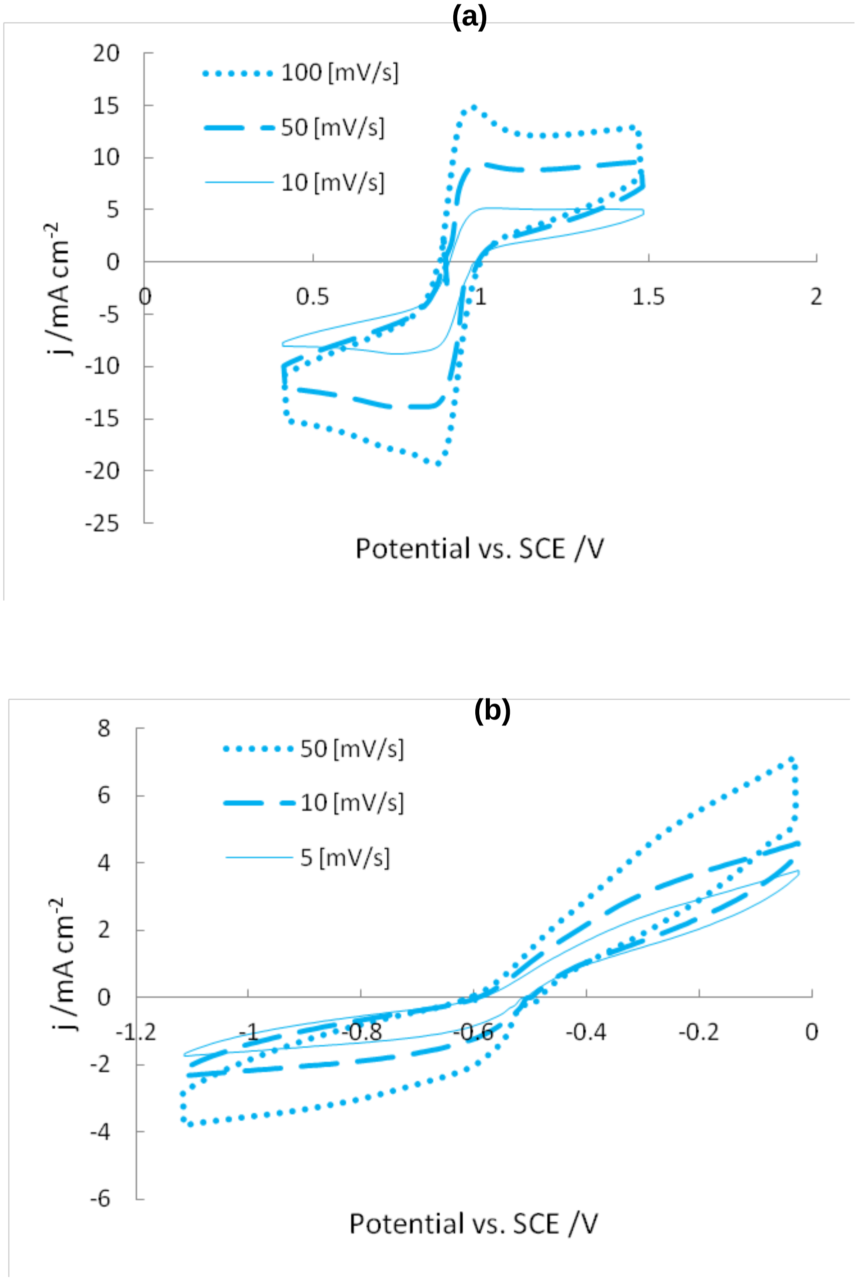

Figure 29. IR compensated cyclic voltammograms at the wet-proofed carbon paper in: (a) V(V)/V(IV); and (b)V(II)/V(III).

Given the peak current densities and peak potentials of V(II) oxidation on the graphite rod in Figure 27 (b), the diffusion coefficient of V(II) species is estimated using

Equation (21) and a linear fit with α = 0.29 (from Tafel analysis in Figure 25 (b)) and c_o^{bulk} = 1.89 M (corresponding to the initial bulk concentration of 94.5% V(II)). For V(V), the cathodic side of the CV curves in Figure 27 (a) is used with α = 0.89 (from Tafel analysis in Figure 25 (a)) and c_o^{bulk} = 1.84 M (corresponding to the initial bulk concentration of 92% V(V)). The calculated diffusion coefficients for V(V) and V(II) are $D_o^V = 1.30 \times 10^{-6}$ and $D_o^{II} = 2.05 \times 10^{-6}$ cm^2 s^{-1}, respectively. These results are consistent with previously reported data in the literature: $D_o^V = 1.1 \sim 1.41 \times 10^{-6}$ [46, 50, 51] and $D_o^{II} = 1.0 \sim 2.14 \times 10^{-6}$ cm^2 s^{-1} [22, 50]. It is notable that the diffusion coefficient of V(II) in our case is 60% higher than that of V(V). On the microfluidic fuel cell device level, this characteristic may potentially contribute to rebalancing the two half-cells with respect to the favorable kinetics of V(V) reduction.

5.3.4. Application of Measured Parameters for Fuel Cell Operation and Simulation

The usefulness of the measured parameters is demonstrated by incorporation into a numerical model of the microfluidic vanadium redox fuel cell with flow-through porous electrodes [25]. The previously developed numerical model is based on conservation of mass, momentum, species, and charge coupled with electrochemical kinetics that governs the fuel cell operation. One major uncertainty associated with this model, expected to be responsible for previously noted discrepancies between simulated and measured performance data [25], is that the kinetic parameters were adopted from literature data for alternate carbon materials such as solid glassy carbon [22] or pyrolytic graphite [47] and electrolyte compositions different to those used in microfluidic fuel cells. The newly obtained parameters for porous carbon paper materials are expected to reduce the uncertainties in this context. The kinetic parameters specified in the previous model and the revised parameters obtained from our present study are compared in Table 6.

Table 6. Kinetic parameters specified in the numerical microfluidic fuel cell models.

		Previous parameters	Revised parameters
V(V)	k_o [cm s^{-1}]	6.80×10^{-5} [47]	6.36×10^{-5}
	α	0.50	0.92
V(II)	k_o [cm s^{-1}]	1.70×10^{-5} [22]	5.54×10^{-6}
	α	0.50	0.24

The rate constants of regular carbon paper for V(V) and V(II) are reduced by 6.5% and 67%, respectively, by incorporation of the newly measured parameters. In addition, the charge transfer coefficients for both V(V) and V(II) are changed significantly due to the non-symmetric characteristics observed in this study: 0.92 and 0.24, respectively. Note that the symmetry coefficients for V(V)/V(IV) reported in earlier literature are in a range of 0.7 ~ 0.73 [46], while for V(II)/V(III) they are 0.43 ~ 0.67 according to reference [22]. We believe that the kinetic parameters are strongly dependent upon the surface condition of the electrodes and the redox electrolyte concentrations. The actual concentration of V(V) in the present study was 92% (equivalent to 1.84 M) or higher, implying that less than 8% of V(IV) existed in the solution, while a 50:50 mixture of V(V)/V(IV) and a glassy graphite electrode were used in reference [46]. Nevertheless, we carefully repeated our experiments on three different days with different electrolyte batches and electrode strips, and found the results to be highly consistent and repeatable.

The simulated polarization curves obtained from the previous and revised numerical models are compared to measured data at a typical flow rate of 10 μL min $^{-1}$ in Figure 30. The low current density regime is shown here to effectively highlight the activation (kinetic) overpotential region and the effect of the revised kinetic parameters. The revised model shows a significantly improved agreement with the experimental data. In contrast to the previous model, the revised model is able to accurately resolve the initial drop in cell potential normally associated with activation losses at the onset of current generation. The obtained parameters and general observations of this study can thus be effectively employed for accurate device-level simulations, design, and optimization of new microfluidic fuel cell architectures.

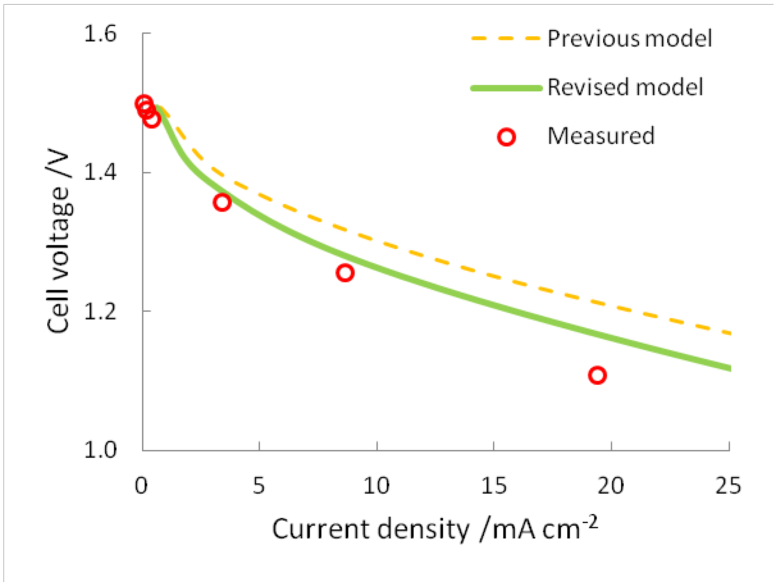

Figure 30. ***Polarization curves at 10 μL min^{-1} obtained from numerical simulations and measured performance of a microfluidic vanadium redox fuel cell with flow-through porous carbon paper electrodes [47].***

5.4. Conclusions

The electrochemical characteristics of the vanadium redox reactions are investigated experimentally on three carbon based electrodes of relevance for microfluidic fuel cells: (i) graphite rod; (ii) carbon paper; and (iii) wet-proofed carbon paper (19% wt. PTFE content). The resistivity of the carbon paper, estimated based on half-cell impedance measurements, is found to be 2.4x higher than that of the graphite rod due to its highly porous structure, and increased further with PTFE content. Kinetic parameters, including exchange current density, charge transfer coefficient, and rate constant are determined for each electrode material. Tafel analysis reveals that V(V) reduction kinetics are faster than V(II) oxidation reactions on all three carbon electrodes. For V(V) reduction, the graphite rod and two porous carbon electrodes produce similar Tafel curves, while for V(II) oxidation the two porous carbon electrodes show notably higher current densities and therefore faster kinetics than the graphite rod electrode. The influence of PTFE layer on electrochemical kinetics is however negligible for both V(V) and V(II) reactions. The estimated rate constants of V(V) reduction and V(II) oxidation on regular carbon paper are somewhat lower than for other carbonaceous materials reported in the literature. In addition, the charge transfer coefficients for both V(V) and V(II) reactions are more non-symmetric than in other studies. We believe that the kinetic parameters are strongly dependent upon the surface condition of the electrodes, the concentration of the vanadium redox species, and the supporting electrolyte (sulfuric acid) concentration.

From the cyclic voltammograms, both half-cell redox reactions are determined to be irreversible. More specifically, the peak to peak separations for the V(V)/V(IV) couple are narrower than those of V(II)/V(III), indicating that the V(II)/V(III) redox reactions are more irreversible and therefore have slower kinetic rates. This trend is consistent with the Tafel analysis where the rate constants for the V(V) half-cell are found to be approximately one order of magnitude higher than for V(II). Finally, when applied in our previously established numerical microfluidic fuel cell model, the kinetic parameters of the carbon paper electrode produce a significantly improved agreement with experimentally measured fuel cell polarization curves.

Several recommendations for microfluidic vanadium redox fuel cell design and operation can be made based on the results of this study. Porous carbon paper electrodes generally provide higher kinetic rates than the graphite rod electrodes. Porous carbon electrodes are thus advantageous in terms of both kinetic and mass transport rates when operated in the flow-through porous electrode configuration. However, the V(II) anode is still expected to be the performance-limiting half-cell and more advanced electrode materials would be required to reach the performance level of the V(V) cathode. It is also noteworthy that the resistivity of carbon paper is higher than for graphite rods and ohmic losses ought to be mitigated on the device-level by integration of current collectors. Although PTFE treatment of the electrodes did not negatively influence the kinetics, it is not recommended for liquid-based fuel cells due to compromised electrode saturation and increased ohmic losses. Reliable and accurate numerical models incorporating relevant empirical parameters such as those reported here are essential for further development of microfluidic fuel cell technologies.

6. Carbon Nanofoam as Electrodes for Microfluidic Fuel Cells

Carbon nanofoam is a carbon-based, synthetic material that has cross-linked networks of nano-scale pores, enabling a significantly higher surface area than conventional carbon papers. In this chapter, the electrochemical properties of vanadium redox couples on the carbon nanofoam are investigated for its potential usage as flow-through porous electrodes in microfluidic fuel cell devices. Kinetic parameters for both V(II) and V(V) discharging reactions are extracted from *IR* compensated Tafel plots and compared: the nanofoam shows superior kinetic characteristics to previously used carbon paper electrodes, offering a 9x rate constant improvement for V(II) oxidation, which is the performance limiting half-cell on the device level. The resistivity of the nanofoam is however 4x higher than for carbon paper, which contributes a negative impact during fuel cell operation. In addition, convective mass transport through the nano-scale pores is limited, thus preventing the net surface area from being fully utilized. Polarization curves obtained from microfluidic fuel cell operation with nanofoam electrodes are compared and discussed in conjunction with the key observations in the electrochemical measurements. Overall, carbon nanofoam electrodes are recommended for microfluidic fuel cell operation in the high cell voltage regime where the performance and efficiency are greatly enhanced.

6.1. Introduction

In the previous chapter, a comprehensive electrochemical study of the vanadium redox reactions on commonly used porous carbon paper (TGPH-060, Toray) electrodes was presented. Tafel analysis revealed that V(V) reduction kinetics were faster than V(II) oxidation reactions. In addition, for V(V) reduction, the carbon paper and solid graphite rod electrode produced similar Tafel curves, while for V(II) oxidation the carbon paper showed notably higher current densities and therefore faster kinetics than the graphite rod electrode. The ohmic resistivity of the carbon paper, estimated based on impedance measurements, was found to be 3x higher than that of the graphite rod due to its highly porous structure.

Developed at Lawrence Livermore National Laboratory [52], carbon aerogels are synthesized by the sol-gel polycondensation of resorcinol and formaldehyde, followed by supercritical drying and pyrolysis in an inert atmosphere. This innovative fabrication process yields unique *carbon foams* that are characterized by high porosity, high surface area, and ultrafine pore sizes (less than 50 nm) [53, 54]. The key advantage of carbon nanofoam as potential electrodes of electrochemical devices over conventional carbon papers is its extremely high surface area of 400-800 $m^2 g^{-1}$ [55], which is approximately 2000x higher than the carbon paper having a mass specific area of 190×10^{-3} m^2 g^{-1} [25]. Snyder et al. evaluated commercialized carbon materials including the nanofoams for their potential use in multifunction energy storage applications [56]. It was claimed that the nanofoam demonstrated the best overall electrochemical performance, with capacities consistently achieving 135 mAh g^{-1} after 50 cycles and capacitances of 5–7 F g^{-1}. Lytle et al. [57] fabricated carbon nanofoam by infiltrating commercially available carbon paper (Toray) with phenolic resin. The polymer-filled paper was then dried and followed by pyrolysis to create electrically conductive sheets of ultraporous carbon structure.

While reports on the electrochemical applications of carbon nanofoam material are available [54, 56, 57], no previous studies have considered the use of nanofoams in microfluidic fuel cells. The objective of the present study is to evaluate commercially available carbon nanofoam (from MarkeTech International) for its potential usage as electrodes in microfluidic vanadium redox fuel cells with flow-through porous electrode architecture. Electrochemical *ex situ* measurements of vanadium redox reactions on nanofoam electrodes, including impedance spectroscopy and Tafel analysis, are employed to investigate the ohmic and electrochemical properties of nanofoam in the context of the present application. Prototype microfluidic fuel cells featuring carbon nanofoams as electrodes are fabricated, tested, and evaluated relative to cells with conventional carbon paper electrodes. The obtained polarization curves are reviewed and discussed with respect to the key observations in the electrochemical *ex situ* measurements.

6.2. Methodology

6.2.1. Electrode and Electrolyte Preparation

Carbon nanofoam materials with and without heat treatment are examined and compared to the regular carbon paper that was reported previously [58]. The carbon nanofoam sheet (Type I, measured thickness ~ 180 μm) is supplied by MarkeTech International and was originally developed as an alternative electrode material to woven carbon cloth [59]. The heat-treated nanofoam is prepared by 1 second exposure of the nanofoam in a propane flame. Based on our preliminary observations, the heat-treated nanofoam shows significantly improved wettability and our intention is to investigate its impact on the electrochemical properties and fuel cell performance. Figure 31 shows scanning electron microscope (SEM) images of the nanofoam, featuring (a) top-down view and (b) cross-sectional view. Randomly distributed as back-bones, carbon fibers are interspersed with macro pores (10-30 μm in diameter) that have a crack-like appearance in the SEM images. It is noteworthy that the macro pores penetrate deeply in the through-plane direction (Figure 31(b)). Note also that no distinguishable differences are observed between non-treated and heat-treated nanofoams in the SEM analysis. Figure 32 shows a highly magnified SEM image of the region that is indicated by the red box in Figure 31(b). The nano-scale pores are randomly distributed in size and the average pore sizes are less than 100 nm. Therefore, compared to the macro pores, the nano pores are anticipated to have significantly higher flow resistances.

As described in the Chapter 5, 2 M vanadium redox electrolyte solutions in 4 M sulfuric acid are prepared from stock electrolyte. V(II) and V(V) solutions are produced by an in-house charger by applying approximately 1.6 V across the anode and cathode. The main focus of the present study is the discharging branch of the vanadium redox reactions, comprising oxidation of V(II) to V(III) and reduction of V(V) to V(IV). The active species concentrations used in this work are 92% (equivalent to 1.84 M) or higher and all measurements are recorded at room temperature.

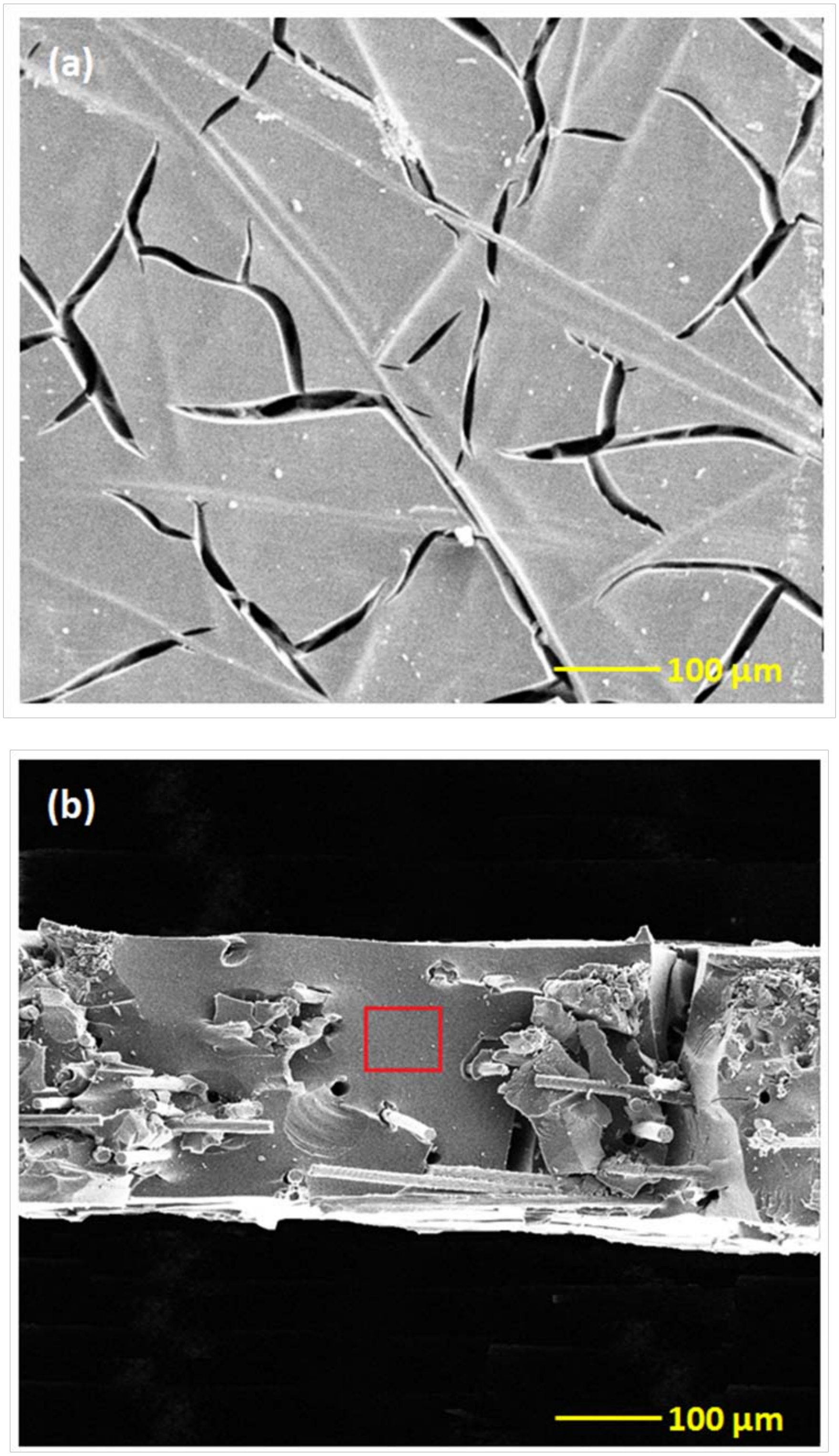

Figure 31. ***Scanning electron microscope (SEM) images of the carbon nanofoam used in this study: (a) top view; and (b) cross section.***

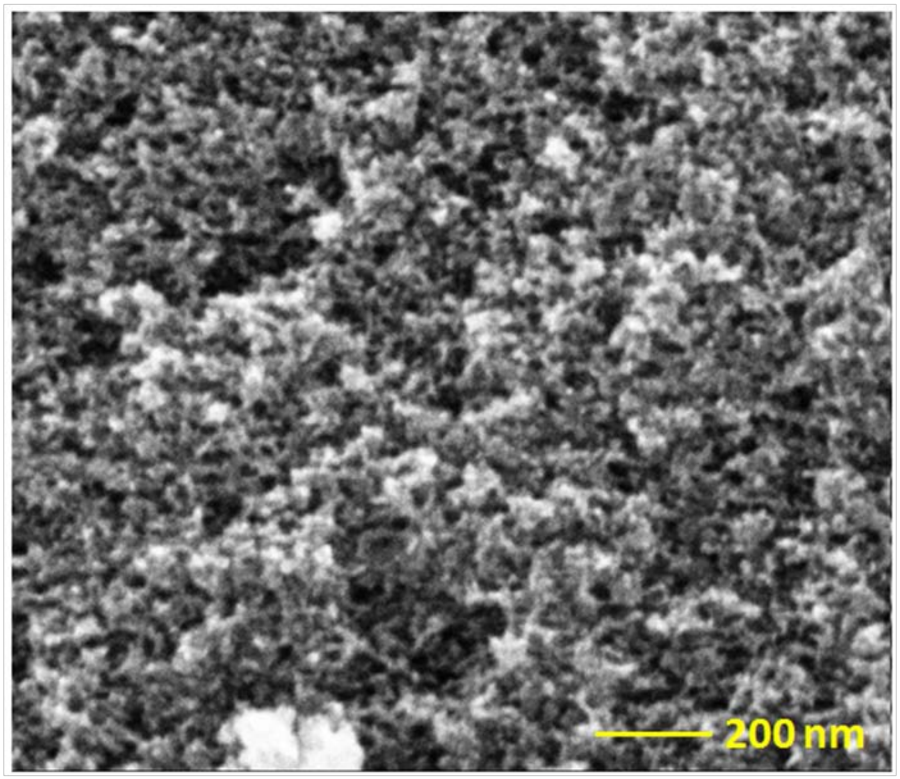

Figure 32. ***Highly magnified SEM image of the nanofoam region indicated by the red box in Figure 31(b).***

6.3. Ex Situ Measurements

A standard three-electrode electrochemical cell controlled and operated by a frequency response analyzer (FRA) capable potentiostat (Reference 3000, Gamry Instruments) is employed for the *ex situ* measurements, as previously described in the section 5.2.3. The stationary working electrodes used in this case are (i) non-treated nanofoam and (ii) heat-treated nanofoam, which have the identical dimensions to the actual electrode prepared for microfluidic fuel cell integration: 18 mm long, 1 mm wide, and 0.18 mm thick [48]. Full details about the experimental setup and procedure can be found in [58].

The overall ohmic resistance and resistivity of the nanofoam material are determined *ex situ* by electrochemical impedance spectroscopy (EIS). At high frequency excitations, the double layer impedance is very low and short circuits the charge transfer branch. This implies that the first real-axis intercept point in the Nyquist plot, denoted as R_s, indicates that the overall impedance is determined by the combined ohmic cell resistance [42]. The R_s values for the carbon nanofoams are measured in V(V) solution with AC amplitude of 10 mV rms over the frequency range from 150 kHz to 10 Hz (at OCP ≈ 0.956 V vs. SCE). For these experiments, the electrolyte solutions are kept still without agitation to impose a pure diffusion condition. The resistivity values are finally calculated from the obtained data using Ohm's law and the electrode dimensions (18 × 1 × 0.18 mm).

A linear potential sweep polarization technique is employed to obtain Tafel curves and investigate the electrochemical kinetics of the vanadium redox reactions on the carbon nanofoam materials. For these measurements, the electrolytes in the three-electrode electrochemical cell are stirred by a magnetic spinner (Corning, PC-220) which is located 3 cm away from the working electrode at the bottom of the container to decouple mass transport limit effects as much as possible.

6.4. In Situ Fuel Cell experiments

A schematic of the membraneless microfluidic fuel cell studied in this chapter is shown in Figure 33. The prototype fuel cells employing (i) non-treated nanofoams and (ii) heat-treated nanofoam as electrodes are fabricated by a master (mold) with measured height of approximately 150 μm. Further details about the fabrication process and cell design can be found in Appendix (p.104-105). Fuel cell polarization curves are measured as described in the previous reports at a flow rate of 10 μL min^{-1} [48]. The current densities and power densities reported here are normalized based on the top surface area of each electrode (approximately 12 × 1 mm).

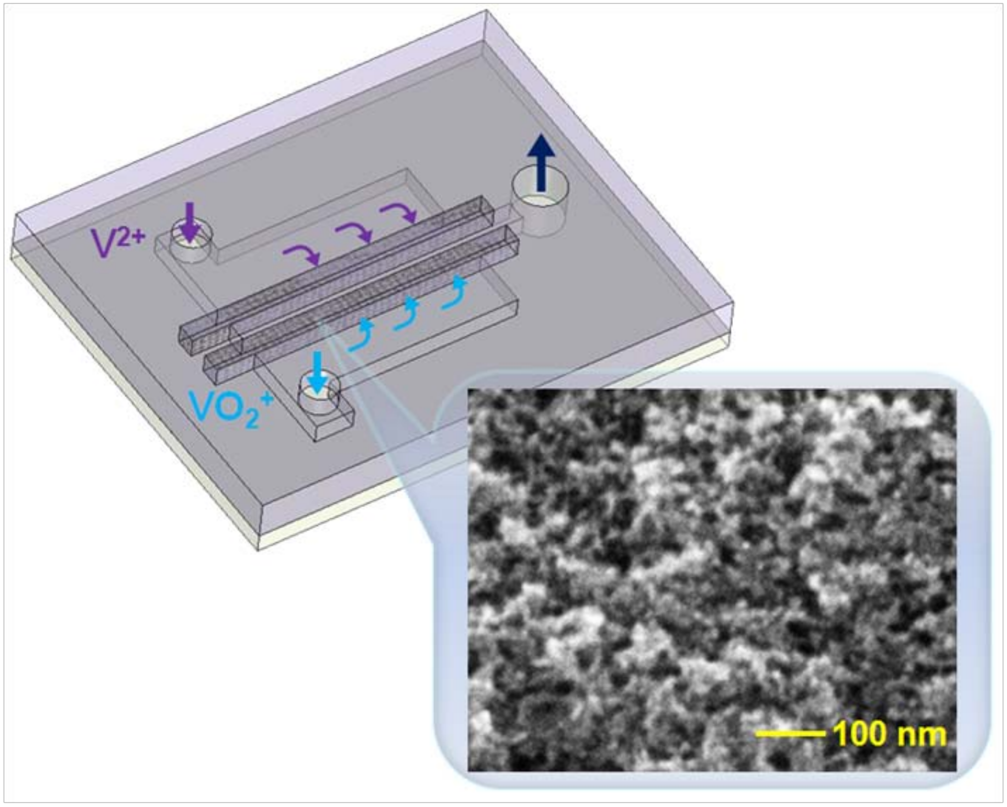

Figure 33. ***Schematic of the microfluidic fuel cell architecture employing nanofoam electrodes.***

6.5. Results and Discussions

The carbon nanofoam electrodes are first analyzed by electrochemical *ex situ* measurements performed in vanadium redox electrolytes, employing the non-treated and heat-treated carbon nanofoam materials as working electrode in a three-electrode electrochemical cell. The overall ohmic resistance and resistivity of the nanofoam are measured by electrochemical impedance spectroscopy. The kinetic parameters for the vanadium redox reactions on the nanofoam electrodes are estimated by linear sweep polarization and key observations are presented. In addition, complete fuel cell polarization curves are measured *in situ* for microfluidic vanadium redox fuel cell devices with embedded nanofoam electrodes. The overall fuel cell performance is compared to existing literature data and the potential use of the nanofoam as electrodes in microfluidic fuel cells is discussed.

6.5.1. Electrochemical Ex Situ Measurements

Electrochemical impedance spectroscopy (EIS) in V(V) solution is first performed to quantify the ohmic properties of the nanofoam electrodes. The net electrode resistance is estimated by subtracting 1 Ω from the first real-axis intercept point (R_s) in the obtained Nyquist plots, assuming the sum of contact and solution resistances to be approximately 1 Ω. Note that electrolyte conditions, electrode positions, and electrical connections are carefully monitored and controlled as constant as possible for each measurement. The corresponding resistivity values determined by Ohm's law and the submerged electrode dimensions are displayed and compared to the regular carbon paper [58] in Figure 34.

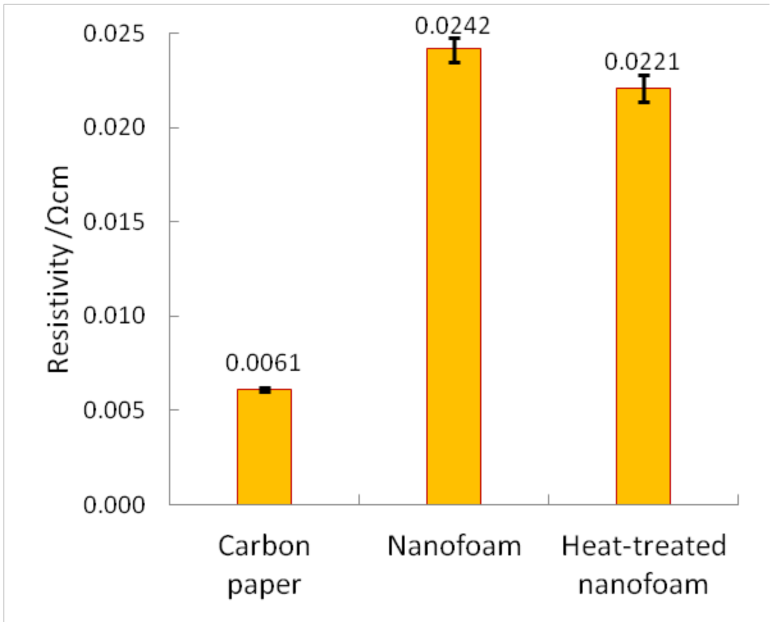

Figure 34. Resistivity values measured ex situ by EIS.

The key observations are summarized below:

- The measured resistance of the nanofoam electrode is almost 4x higher than that of regular carbon paper of the same size. The corresponding resistivity of nanofoam is $24.2 \times 10^{-3}\ \Omega$ cm, which is in good agreement with the manufacturer's specification of $10\text{-}40 \times 10^{-3}\ \Omega$ cm [59].
- The heat-treated nanofoam shows a slightly lower resistivity than the non-treated, as-received material. However, considering the variability of these measurements as indicated by the error bars, it is concluded that there is no significant impact of the heat treatment on the resistivity of nanofoam.

In order to determine the electrochemical kinetic parameters of the vanadium redox reactions with respect to the nanofoam electrodes, a comprehensive Tafel analysis is conducted. With increased ohmic potential drops due to the high resistivity of nanofoam, *IR* compensation is essential in the Tafel analysis to decouple the kinetic and ohmic overpotentials. Figure 35 shows the effect of *IR* compensation in V(V) reduction resulting from the overall ohmic resistance of carbon nanofoam. The compensation is found to contribute up to 400 mA cm^{-2}, which causes a significant upward shift in the Tafel plots, and is therefore important for unbiased and accurate estimation of kinetic parameters. The *IR* compensated Tafel plots for the two nanofoam materials investigated in this study are provided in Figure 36 for (a) V(V) reduction and (b) V(II) oxidation. Note that *IR* compensation was performed using the overall ohmic resistances measured in the previous page for each electrode.

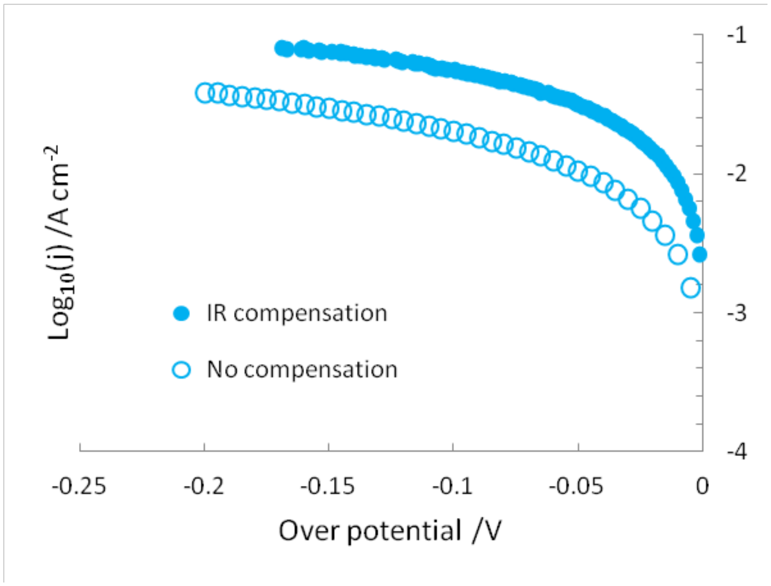

Figure 35. ***Effect of IR compensation in the Tafel plot for V(V) reduction on the nanofoam electrode.***

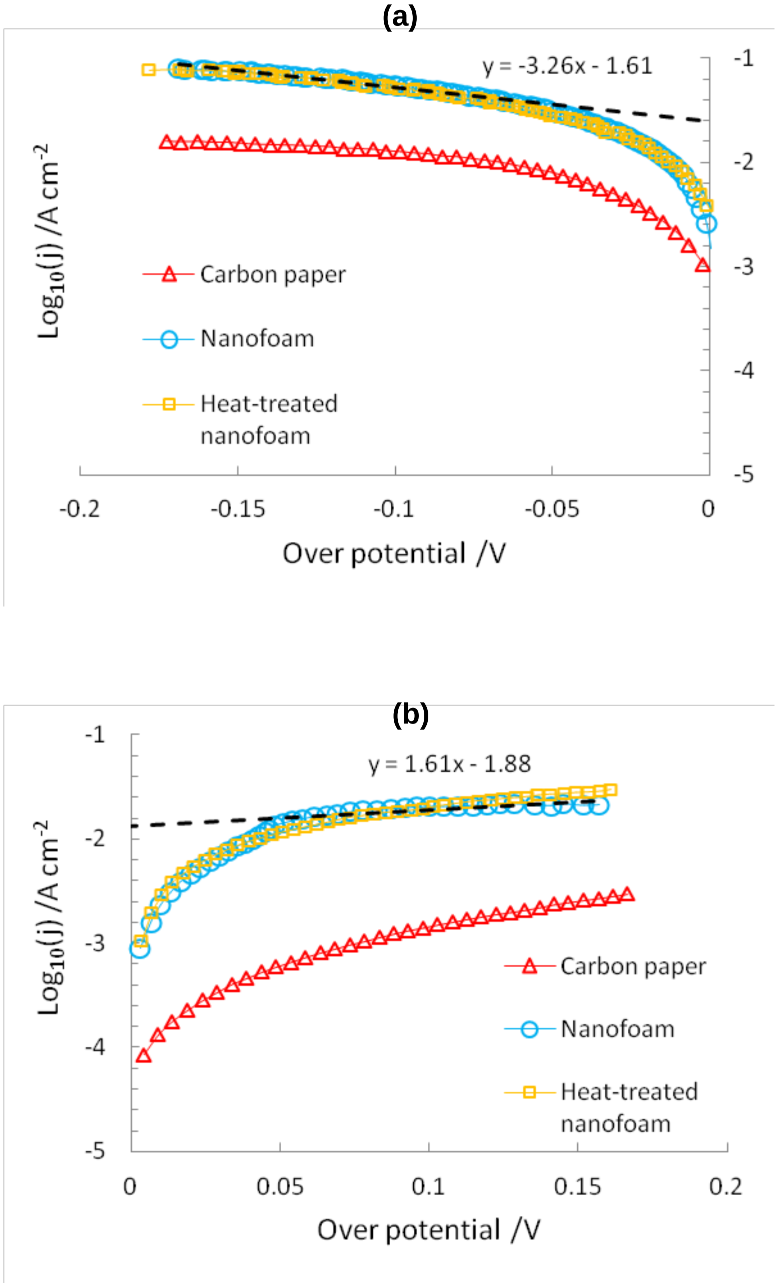

Figure 36. IR compensated Tafel plots measured ex situ for (a) V(V) reduction and (b) V(II) oxidation.

Note that the linear regression lines for the *nanofoam* are shown by the dashed lines with corresponding equations.

The main observations from the Tafel plots are summarized below:

- Compared to the regular carbon paper [58], the nanofoam electrodes show significantly improved kinetic rates for both V(V) reduction and V(II) oxidation, and the relative degree of enhancement is greater in V(II) oxidation.
- In general, V(V) reduction kinetics are faster than V(II) oxidation on the nanofoam electrodes. These findings are consistent with data obtained for solid glassy carbon electrodes [22, 23, 50]. However, the difference in y-intercept values between the V(V) and V(II) curves is significantly reduced compared to the carbon paper, which indicates that the kinetic rate of slower reaction, V(II) half-cell, is enhanced more.
- As anticipated, the Tafel plots for the non-treated and heat-treated nanofoam are almost identical, indicating that the effect of heat treatment on kinetics is negligible. Note that our intention is to investigate the effect of heat treatment in fuel cell operation which involves electrode saturation and mass transport characteristics of the reactant streams.

The kinetic parameters such as exchange current density and charge transfer coefficient are determined from the Tafel plots, followed by rate constant calculation. The values of the charge transfer coefficients (α) for V(V) reduction and V(II) oxidation are illustrated in Figure 37 where the average and standard deviation of three repeated measurements are reported. The α values for both V(V) reduction and V(II) oxidation indicate that the vanadium redox reactions on the nanofoam under present conditions are highly asymmetric, which is consistent with our previous study of solid graphite electrodes in the same electrolytes [58]. Note that the symmetry coefficients for V(V)/V(IV) reported in earlier literature are in a range of 0.7 ~ 0.73 [46], while for V(II)/V(III) they are 0.43 ~ 0.67 according to reference [22, 23]. Nevertheless, the charge transfer coefficients obtained for the nanofoam electrodes are very similar to those of regular carbon paper electrodes under the same conditions.

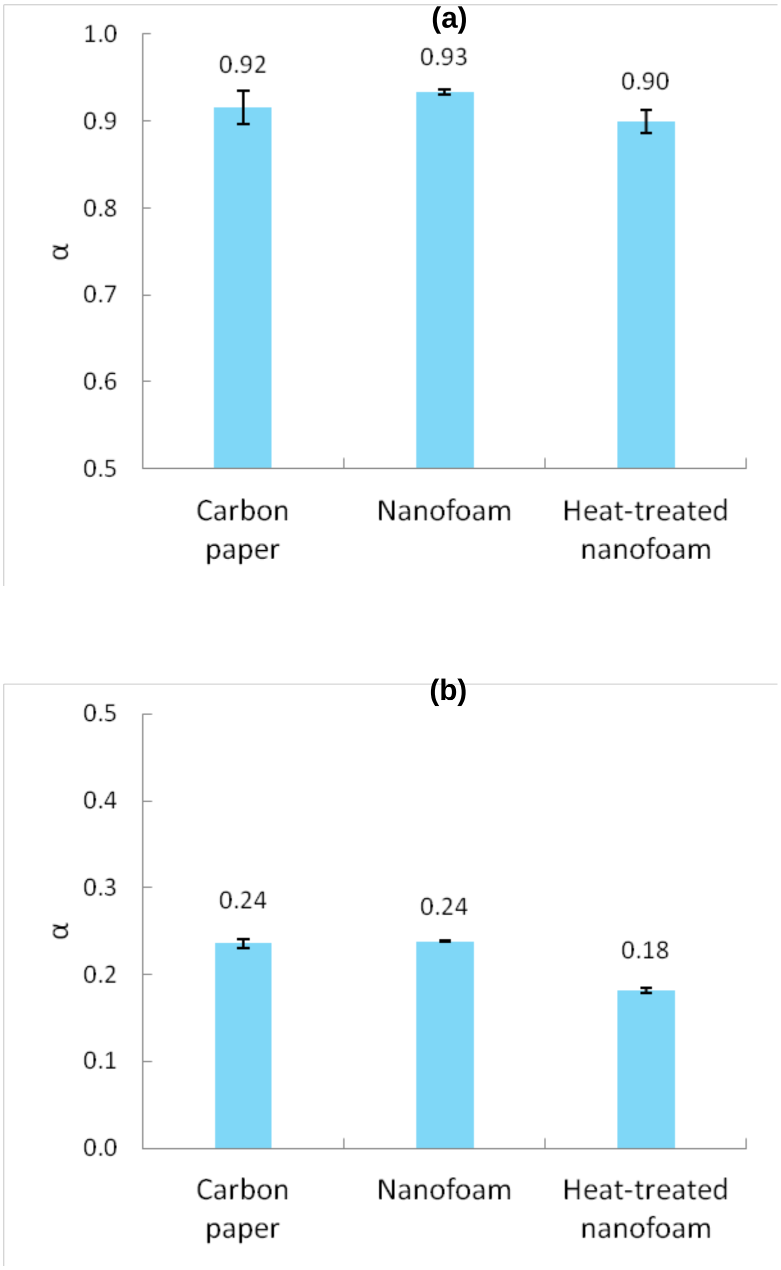

Figure 37. Charge transfer coefficients (α) determined ex situ from Tafel plots for (a) V(V) reduction and (b) V(II) oxidation.

Figure 38 shows the rate constants (k_o) estimated from the Tafel curves for both V(V) reduction and V(II) oxidation reactions. As mentioned, the kinetic rates obtained on carbon nanofoam electrodes are significantly faster than those of the carbon paper: for

V(II) oxidation, the nanofoam shows 9.2x higher rate constant, while 5.2x higher for V(V) reduction.

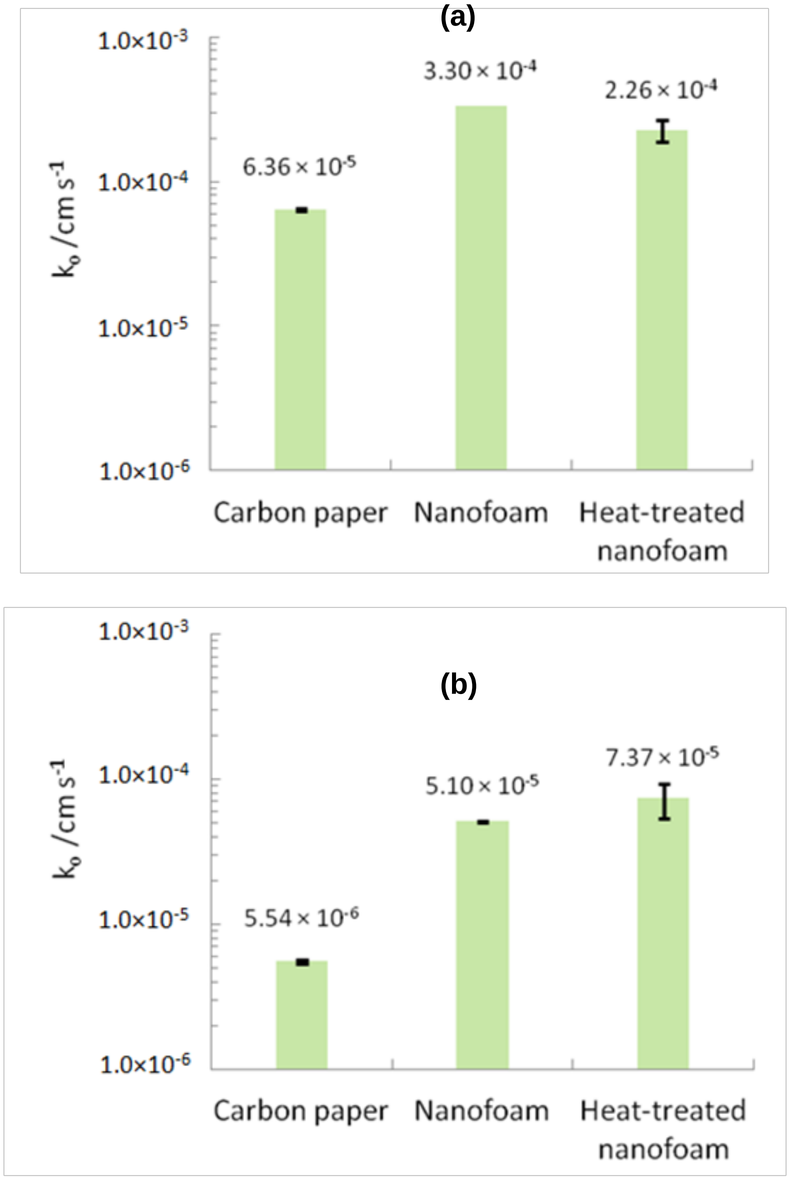

Figure 38. ***Estimated values of rate constants (k_o) calculated by Tafel plots and Equation (4): (a) V(V) reduction; and (b) V(II) oxidation.***

Consequently, it is anticipated that the activation overpotential for fuel cell operation employing the nanofoam electrodes would be much smaller, which is analyzed in the following section. Another interesting observation is that since the enhancement in the kinetic rate of V(II) is greater than V(V), the kinetic rate differences between V(II) and

V(V) half-cells become smaller. More quantitatively, the V(V) kinetic rate of the nanofoam is 6.5x higher than for V(II), while the V(V) rate of the carbon paper is 11x faster than for V(II). As mentioned in the previous section, the heat treatment does not make a noticeable impact on the kinetics of vanadium redox reactions on nanofoam electrodes.

6.5.2. In Situ Fuel Cell Measurements

Prototype microfluidic vanadium redox fuel cells are fabricated and tested employing the nanofoam materials investigated in this work and compared to the regular carbon paper cell [48]. Since the electrolytes, supply rate, and microchannel dimensions are considered identical for the three fuel cell devices, it is assumed that the only difference between these cells is attributed by the electrode materials. Polarization and power density curves, provided in Figures 39-40, are measured with each cell and compared to examine the fuel cell performance at 10 μL min^{-1}. The key observations in terms of performance are:

- As anticipated from the Tafel analysis in the previous section, the nanofoam cells, regardless of the heat treatment, show significantly lower kinetic or activation overpotentials compared to the carbon paper cell and perform exceptionally well at high cell voltages. More specifically, the first three data points of the nanofoam cells do not have a noticeable drop in cell potential (less than 5 mV), while the initial cell potential drop of the baseline cell is clearly seen in Figure 39(b). It is estimated that the activation losses are reduced by up to 200 mV, although it may be masked by other types of voltage losses (as discussed below).

  In the linear regime where the ohmic overpotentials are dominating, the slopes of the nanofoam cells are steeper than that of the baseline. This trend is consistent with the impedance measurements: the overall ohmic resistance of the nanofoam is 4x higher than the carbon paper, which contributes a negative impact during fuel cell operation.

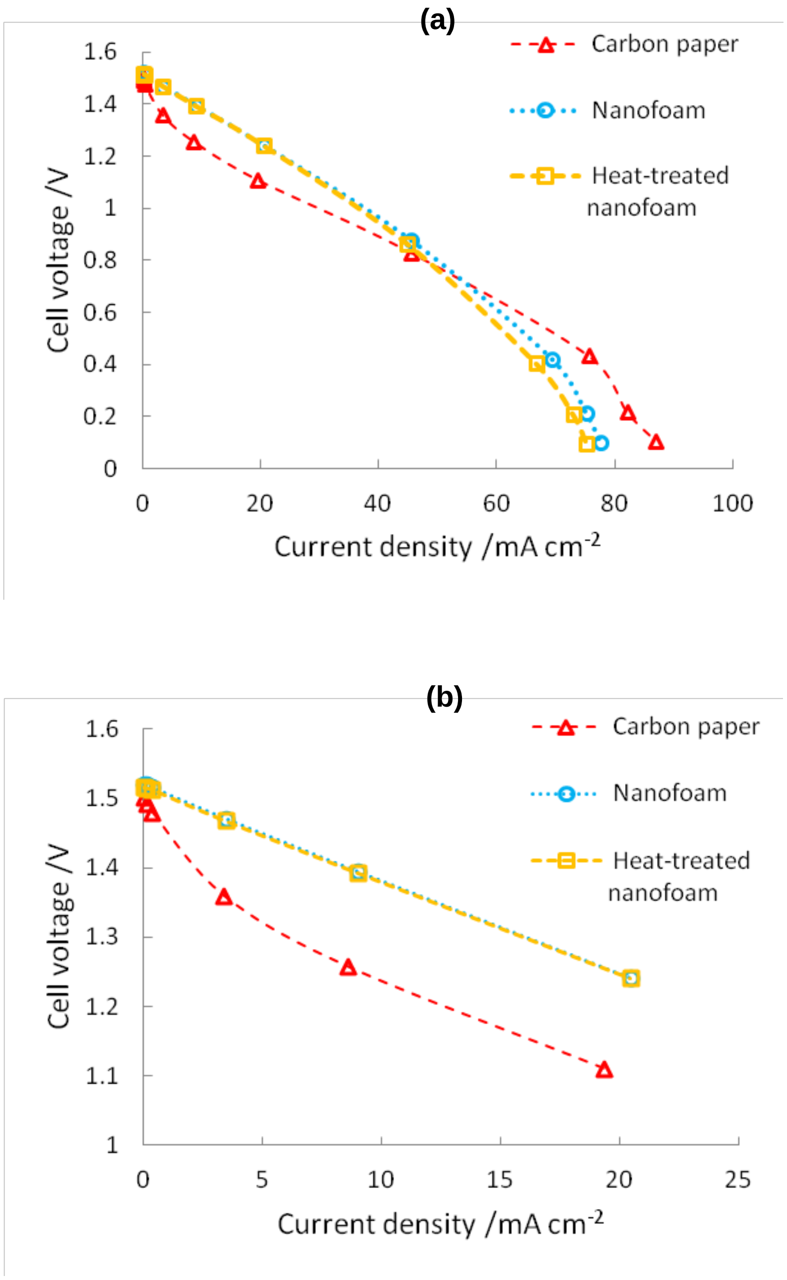

Figure 39. ***Measured polarization curves for microfluidic vanadium redox fuel cell operation at 10 µL min^{-1}: (a) full polarization curve; and (b) zoomed-in plot of the low current density regime.***

- Both the non-treated and heat-treated nanofoam cells have more curvature than the baseline in the linear portion of the polarization curves (Figure 39(a)), indicative of gradually increasing mass transport losses. Our preliminary investigation reveals that convective mass transport by flow through the nano-scale pores is considerably constrained, preventing the net surface area of the nanofoam from being fully utilized. More specifically, it is expected that the main stream of liquid electrolytes flows through the macro pores that have cleavages in the size of 10-30 μm (Figure 31(b)), since the flow resistances of the nano pores are substantially higher. Combined with the higher ohmic resistivity, the limited mass transport properties are expected to reduce the effectiveness of nanofoam as electrodes in microfluidic fuel cells when operated in the high current density regime.

- Our visual inspection indicated that the wetting of electrolyte in the nanofoam is significantly improved after heat treatment (as described in section 6.2.1). The impact of heat treatment on fuel cell performance (Figure 39) is however negligible, implying that the wetting characteristic is not a decisive factor in fuel cell operation.
- The corresponding power density curves in Figure 40 indicate that the nanofoam cells achieve approximately 6% higher peak power density than the carbon paper cell. Although the nanofoam has superior kinetic characteristics to the carbon paper, offering 9x and 5.2x higher kinetic rate constants for V(II) oxidation and V(V) reduction, respectively, the combined effect of increased ohmic and mass transport losses results in a limited net improvement of the peak power density.

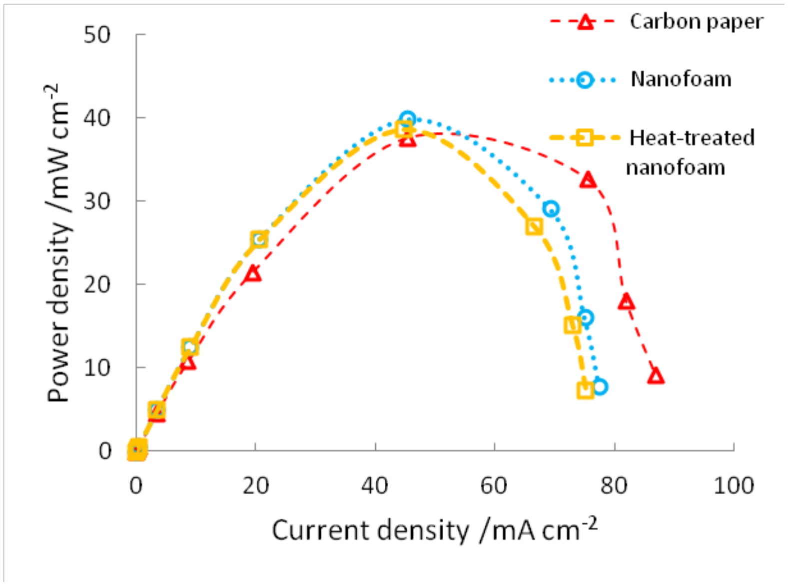

Figure 40. ***Corresponding power density curves for the fuel cell devices operated at 10 µL min^{-1}.***

In summary, the microfluidic vanadium redox fuel cells employing the nanofoam electrode are advantageous over the carbon paper cells for high cell voltage applications due to the high surface area and superior kinetic characteristics. However, at moderate and high current density regimes (low cell voltages), the gain accomplished by the rapid kinetics is compromised by the combined effect of increased ohmic losses and reduced mass transport rates when compared to the carbon paper material.

6.6. Conclusions

In this work, the electrochemical characteristics of vanadium redox couples on carbon nanofoam are investigated experimentally for its potential usage as electrodes of microfluidic fuel cells in the flow-through configuration. Non-treated and heat-treated carbon nanofoam electrodes are investigated and compared to the regular carbon paper reported previously [58]. Electrochemical impedance spectroscopy reveals that the ohmic resistivity of the nanofoam is 4x higher than the carbon paper and the estimated resistivity (24.2×10^{-3} Ω cm) is in good agreement with the manufacturer's specification.

Kinetic parameters for both V(II) and V(V) discharging reactions are extracted from *IR* compensated Tafel plots and compared: the nanofoam shows superior kinetic characteristics to the carbon paper, offering 9x higher rate constant for V(II) oxidation and 5.2x higher for V(V) reduction. The effect of heat treatment on kinetics is found to be negligible.

The microfluidic fuel cell devices employing carbon nanofoam as electrodes, regardless of the heat treatment, demonstrate significantly reduced activation overpotentials due to the high active surface area and rapid kinetics, which is a major advantage for overall fuel cell performance. However, in the linear regime of the polarization curves, the slopes of the nanofoam cells are steeper than that of the baseline, indicative of higher ohmic losses during cell operation. In addition, convective mass transport of liquid electrolytes through the nano-scale pores is limited, preventing the net surface area from being fully utilized. Consequently, the nanofoam cells offer only a moderate improvement in peak power density (6% higher at 10 μL min^{-1}) compared to the baseline cell, provided that the gain of fast kinetic rates is compromised by the combined effect of increased ohmic losses and reduced mass transport rates of the nanofoam material.

To conclude the present study, several recommendations can be made for microfluidic vanadium redox fuel cell device-level integration. Carbon nanofoam materials provide higher surface area and faster kinetics the carbon paper. Hence, nanofoam electrodes are suitable for fuel cell devices operating in the high cell voltage regime. However, as the current density is increased, higher ohmic overpotentials and mass transport limitations will gradually offset the gain from its faster kinetics. Therefore, nanofoam is less suitable as electrodes for devices that require operation at high current densities. The future material development will be focused on electrode materials with high surface area, low resistivity, and low permeability.

7. Double-pass Fuel Cell Architecture

As a part of continuing efforts on developing a microfluidic redox flow battery, a novel cell architecture is proposed adapting a double-pass concept: at a given electrode length and flow rate, this innovative design allows approximately double the flow velocity and therefore boosts cell performance significantly. The proposed cell achieves almost 78% net increase in the peak power density over the baseline cell at 300 μL/min, while 57% increase at 10 μL/min. The peak power density demonstrated by this new cell at 300 μL/min is almost as good as the current collector cell, which is a state-of-the-art performance in the microfluidic fuel cells. The key concept and preliminary fuel cell performance are discussed in this chapter.

7.1. Design Concept

Schematic of the proposed design is shown in Figure 41. There are two key aspects of this novel cell design:

- Firstly, the new cell is geometrically symmetric, having 2 inlet and 2 outlet ports, so that the cell can be operated in both forward and backward directions. In other words, the fuel and oxidant are discharged in one direction and, if necessary, the waste reactants are fed back in the other direction for charging mode operation.
- Double-pass concept: the fuel and oxidant streams flow through the first half of the electrodes and meet in the center channel, flowing in a co-laminar pattern. Before exiting, the two streams flow through the second half of the electrodes and finally flow toward the outlets. The main motivation is originated from a fact that for the baseline cell the overall fuel utilization is substantially low especially at high flow rates (7.7% at 300 μL min^{-1}) as shown in Table 3 (p. 23, Chapter 3). In the proposed cell design, unutilized fuel/oxidants can be consumed at the second half of the electrode. In addition, since the flow inlet area is reduced by half, this innovative

design allows approximately double the convectional mass transport at a given electrode length and flow rate.

(a)

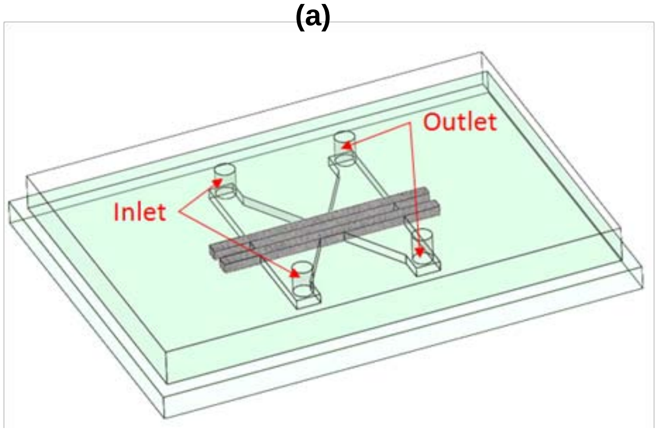

(b)

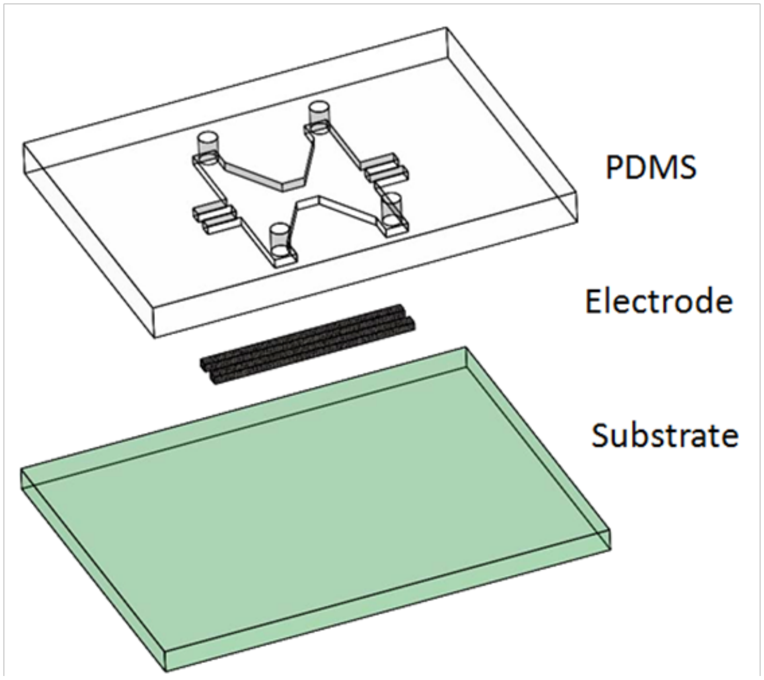

Figure 41. ***Schematic of the double-pass fuel cell design: (a) assembly view; and (b) exploded view (not to scale).***

The electric contacts are located at the end of the electrodes, which are glued to external wires with conductive epoxy as explained previously. Figure 42 shows (a) top view with some key dimensions; and (b) actual cell photo: the first and second half of the electrode are 5 mm each and the land is 4 mm long, which is intended to minimize unwanted flow bypass.

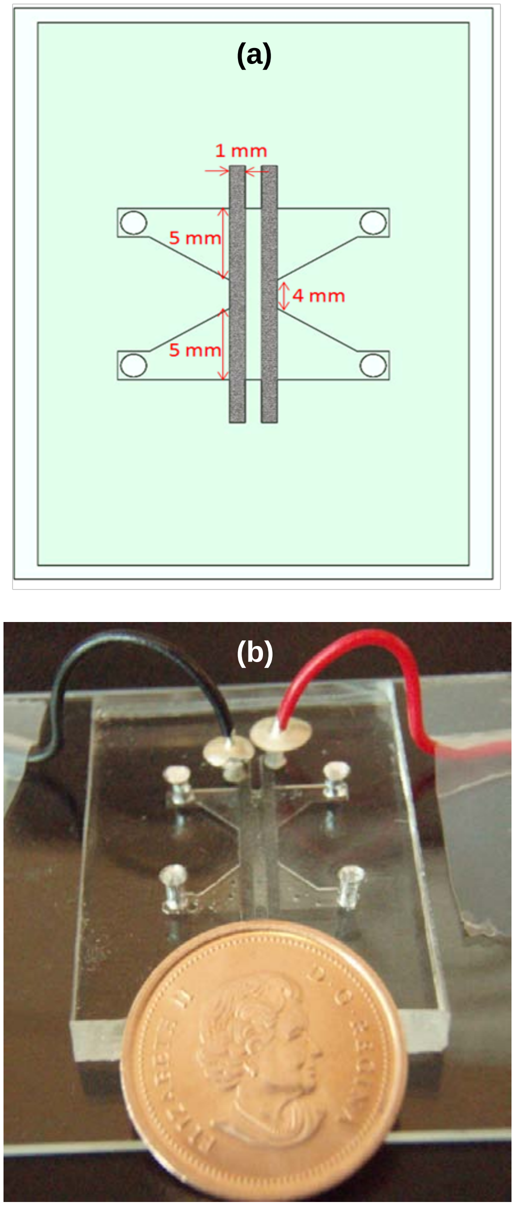

Figure 42. *(a) Top view of the cell with some key dimensions labeled (not to scale); and (b) actual cell photo.*

7.2. Methodology

7.3. Numerical Simulation

A three-dimensional computational fluid dynamics (CFD) simulation is intensively used to investigate the flow characteristics of the double-pass cell. Details about the parameters and specifications of this 3-D model can be found in section 4.1.7 (p. 33-34).

7.4. Fuel Cell Characterization

The prototype fuel cell employing regular carbon paper as electrodes is fabricated by a master (mold) with measured height of approximately 150 μm. The overall fabrication steps are identical to the previous cells discussed in the previous chapters. In addition, fuel cell polarization curves are measured as described in the previous chapters at flow rates of 10 and 300 μL min^{-1}. For fair comparison, the current densities and power densities reported in this chapter are normalized differently, which is based on the net flow area normal to the main flow direction: the net flow area is 0.015 cm^2 (1 cm × 0.15 cm) for the double-pass cell, while it is 0.018 cm^2 (1.2 cm × 0.015 cm) for the baseline and current collector cells discussed in Chapter 4.

7.5. Results and Discussions

7.5.1. Flow Characteristics

Figure 43 shows pathlines of the double-pass cell colored by velocity magnitude at 10 μL min^{-1} (unit: [m s^{-1}]). As explained in section 7.1, the main streams of V(II) and V(V) flow through the first half of the electrodes and meet in the center channel. At the middle of the center channel where the net channel area is the minimum, the streams are accelerated reaching the highest local velocity at around 3.54 mm s^{-1}. After passing by the neck, the velocity field is then decelerated like a diffuser and the streams flow through the second half of the electrodes.

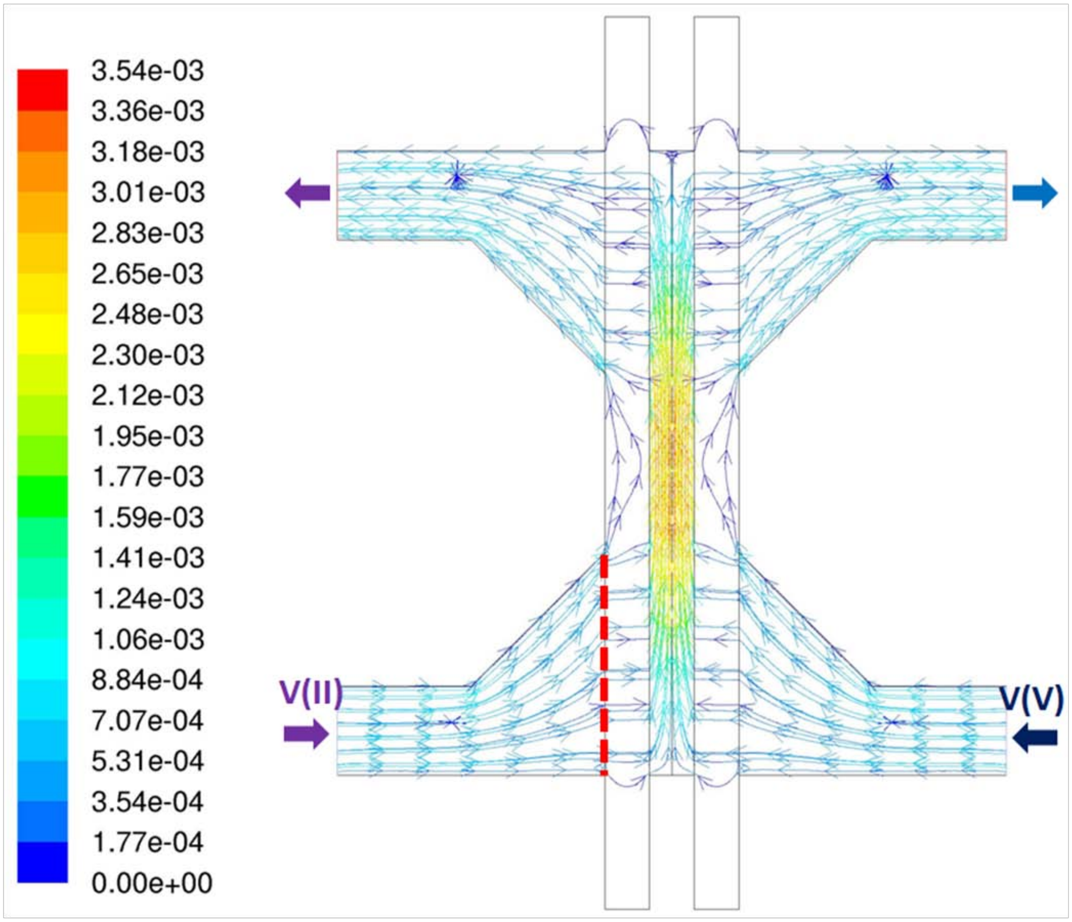

Figure 43. Pathlines colored by velocity magnitude at 10 μL min^{-1}.

The average velocity along the red dashed line in Figure 43 is calculated: 0.29 mm s^{-1}, while it is 0.13 mm s^{-1} for the baseline cell of the same channel height (from section 4.2.1.), indicating that the convectional mass transport rate increased by a factor of 2.2 at a given flow rate of 10 μL min^{-1}. On the other hand, the pumping loss of the double-pass cell is approximately doubled compared to the baseline. However, the pumping loss and the total pressure drop across the porous electrodes are still negligible (less than 0.4% of the total power output).

7.5.2. Polarization Curves

The polarization curves are measured as explained previously: 10 and 300 μL min^{-1}. It is noteworthy that the current densities and power densities reported here are based on the net flow area normal to the main flow direction: the net flow area is 0.015 cm^2 (1 cm × 0.15 cm) for the double-pass cell, while the baseline is 0.018 cm^2 (1.2 cm ×0.15 cm). The measured polarization curves of the double-pass cell are displayed and compared to the baseline and current collector cells [48] in Figure 44.

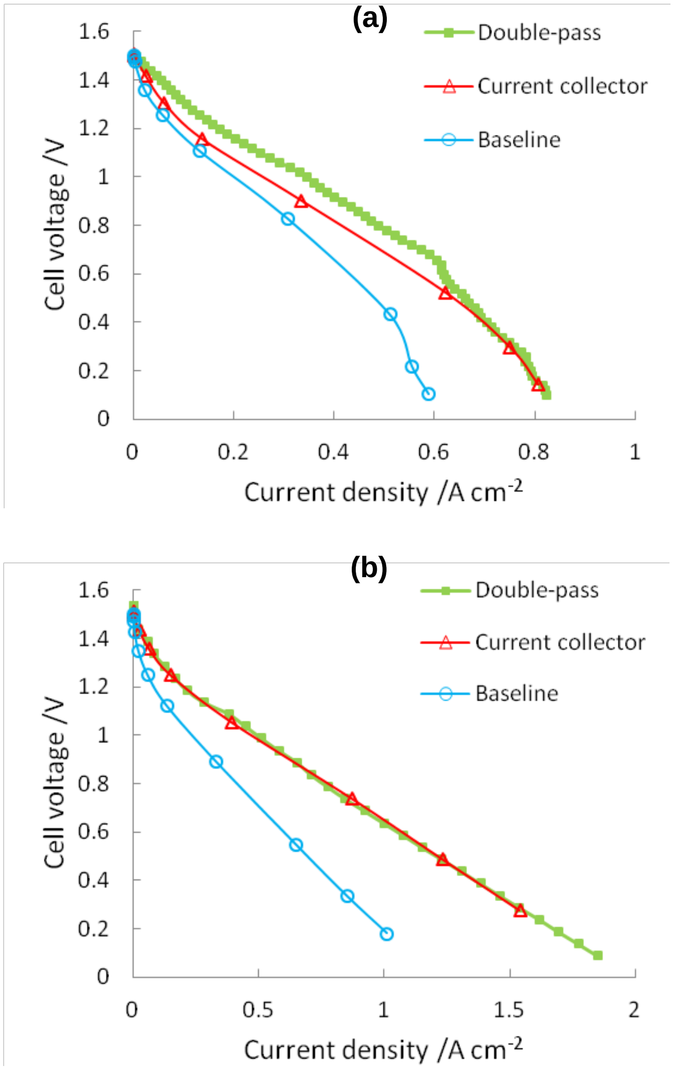

Figure 44. Comparison of polarization curves for the three cells studied: (a) 10 μL min^{-1} ; and (b) 300 μL min^{-1}.

Compared to the baseline cell, the proposed cell shows significantly improved power densities at both flow rates: the peak power density gains are 54% (from 0.26 to 0.40 A cm^{-2}) and 78% (0.36 to 0.64 A cm^{-2}) at 10 and 300 μL min^{-1}, respectively. Figure 45 shows the corresponding power density curves. The pick power density of the proposed design is 0.40 W cm^{-2}, which is a 20% increase over the current collector (0.33 W cm^{-2}) at 10 μL min^{-1}.

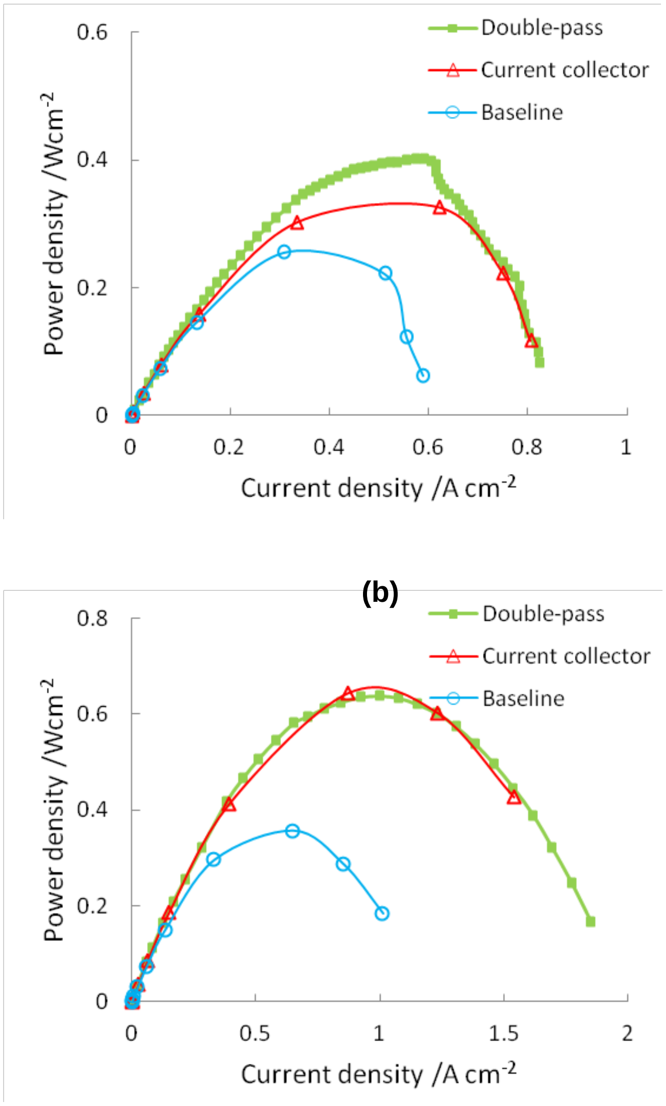

Figure 45. **Corresponding power density curves of the three cells: (a) 10 μL min^{-1} ; and (b) 300 μL min^{-1}.**

7.6. Conclusions

A new cell architecture adapting double-pass concept is proposed and demonstrated. In the proposed cell design, unutilized fuel/oxidants can be consumed at the second half of the electrode. In addition, since the flow inlet area is reduced by half, this innovative design allows approximately double the convectional mass transport at a given electrode length and flow rate. Along with numerical studies, prototype cells are fabricated, tested and compared to the baseline and current collector cells. This proof of concept cell shows significantly improved performance: the power density at 300 μL/min is almost as good as the current collector cell, which is the highest in this field; a 54% increase in the peak power density is achieved at 10 μL/min, compared to the baseline cell.

In parallel with the discharging study on the proposed cell discussed in this chapter, the charging mode operation is being investigated by our group, which is not covered in this thesis. This proposed cell is anticipated to open up new research opportunities in a membraneless, microfluidic redox flow battery, which has not been actively researched yet.

8. Summary and Future Works

Chapter 8 presents a summary and conclusions of the current research, followed by some recommendations for the future development of microfluidic fuel cells.

8.1. Summary and Conclusions

A performance investigation on microfluidic vanadium fuel cell with flow through porous electrodes has been conducted with five individual (but closely related) activities completed. Figure 46 shows typical fuel cell losses (or overpotentials) labeled with corresponding chapters of the current thesis.

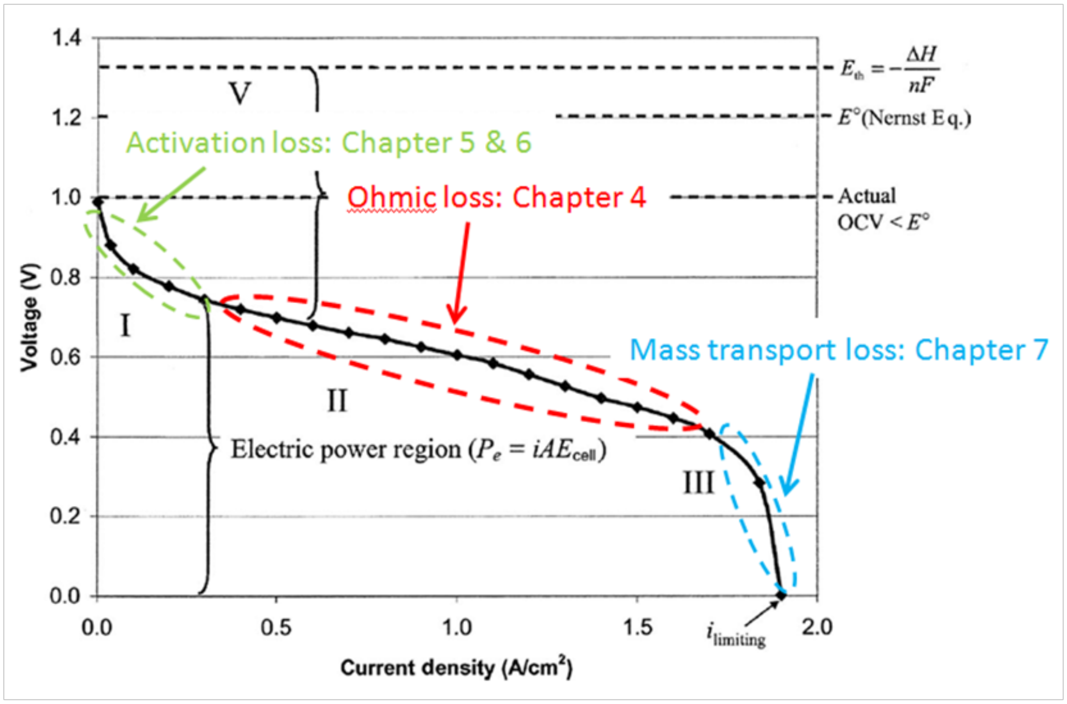

Figure 46. Fuel cell losses labeled with corresponding chapters.

- Parametric study (Chapter 3)
- Chip-embedded thin film current collector (Chapter 4)
- Electrochemical study on Porous Carbon Electrodes (Chapter 5)
- Carbon nanofoam as electrodes (Chapter 6)
- Double-pass fuel cell architecture (Chapter 7)

8.1.1. Parametric Study

The dimensions of porous carbon electrodes and microchannels are varied from the baseline design to investigate their impacts on the fuel cell performance. In addition, a dependency on the number of electrical contacts is examined. Numerical simulations are performed in parallel with experimental activities to understand the coupled effects of mass transport, electrochemistry, electron conduction, and fluid mechanics:

- Mass transport rates control the performance at low flow rates. The limiting current density can be increased at a given flow rate by reducing the electrode inlet area.
- Ohmic resistance controls the performance at high flow rates. Both current and power density can be increased by reducing the overall ohmic resistance in the longitudinal direction.
- Increasing the number of electrical contacts has only minor impact on the mass transport limit and ohmic resistance and consequently no major effect on cell performance.
- Narrowing down the center channel contributes a slight improvement at high flow rates due to reduced ohmic resistance but has no measureable impact on performance at low flow rates.
- In order to minimize the discrepancies between modeling results and measured data, detailed impedance measurements for the current cells are strongly recommended.

8.1.2. Chip-embedded Thin Film Current Collector

A chip-embedded thin film current collector is discussed to mitigate the high contact resistance associated with the use of porous electrodes in microfluidic fuel cells. The main motivation of this work is to reduce the contact resistance of the cell by means of custom-designed, device-integrated current collectors that allows an increased number of contact points distributed across the length of the electrodes in close proximity to the reaction sites. In addition to regular performance measurements, an electrochemical impedance spectroscopy (EIS) study is conducted to analyze the voltage losses, impedance characteristics, and ohmic contributions of the cells:

- Compared to the baseline, the current collectors incorporated in the CC-I cell (regular carbon paper) results in a peak power density improvement from 52 to 93 mW cm^{-2}, corresponding to a 79% net increase. This drastic performance boost is attributed to a net decrement of 7.9 Ω in contact resistances, quantified by a negative shift in the high frequency impedance measured by EIS. The reduction in overall ohmic cell resistance associated with the current collectors is comparable to the net reduction in polarization curve slope in the central, linear portion of the curve. The CC-I cell achieved a volume specific peak power density of 6.2 W cm^{-3}, which compares favorably to all previously reported microfluidic fuel cell devices.
- A carbon paper coated with an MPL is also evaluated as a potential strategy to enhance the contact area and uniformity of the porous carbon / current collector interface in the CC-II cell. The overall performance of CC-II is however found to be substantially lower than that of the baseline. Provided that the MPL-coated carbon paper contained a significant amount of PTFE as a structural binder and hydrophobicity agent, we expect that the electrode does not wet completely, resulting in reduced utilization of active reaction area and non-uniform flow distribution inside the electrodes.

8.1.3. Electrochemical study on Porous Carbon Electrodes

The electrochemical characteristics of the vanadium redox reactions are investigated experimentally on three carbon based electrodes of relevance for microfluidic fuel cells: (i) graphite rod; (ii) carbon paper; and (iii) wet-proofed carbon paper (19% wt. PTFE content). Half-cell electrochemical impedance spectroscopy is applied to measure the overall ohmic resistance and resistivity of the electrodes. Kinetic parameters for both V(II) and V(V) discharging reactions are extracted from Tafel plots and compared for the different electrodes:

- The resistivity of the carbon paper, estimated based on half-cell impedance measurements, is found to be 2.4x higher than that of the graphite rod due to its highly porous structure, and increased further with PTFE content.
- Tafel analysis reveals that V(V) reduction kinetics are faster than V(II) oxidation reactions on all three carbon electrodes. For V(V) reduction, the graphite rod and two porous carbon electrodes produce similar Tafel curves, while for V(II) oxidation the two porous carbon electrodes show notably higher current densities and therefore faster kinetics than the graphite rod electrode. The influence of PTFE layer on electrochemical kinetics is however negligible for both V(V) and V(II) reactions. The estimated rate constants of V(V) reduction and V(II) oxidation on regular carbon paper are somewhat lower than for other carbonaceous materials reported in the literature. In addition, the charge transfer coefficients for both V(V) and V(II) reactions are more non-symmetric than in other studies.
- From the cyclic voltammograms, both half-cell redox reactions are determined to be irreversible. More specifically, the peak to peak separations for the V(V)/V(IV) couple are narrower than those of V(II)/V(III), indicating that the V(II)/V(III) redox reactions are more irreversible and therefore have slower kinetic rates. This trend is consistent with the Tafel analysis where the rate constants for the V(V) half-cell are found to be approximately one order of magnitude higher than for V(II). Finally, when applied in our previously established numerical microfluidic fuel cell model, the kinetic parameters of the carbon paper electrode produce a significantly improved agreement with experimentally measured fuel cell polarization curves.

8.1.4. Carbon nanofoam as electrodes

Carbon nanofoam is a carbon-based, synthetic material that has cross-linked networks of nano-scale pores, enabling a significantly higher surface area than conventional carbon papers. In Chapter 6, the electrochemical characteristics of vanadium redox couples on carbon nanofoam are investigated experimentally for its potential usage as electrodes of microfluidic fuel cells in the flow-through configuration. Non-treated and heat-treated carbon nanofoam electrodes are investigated and compared to the regular carbon paper reported previously:

- Electrochemical impedance spectroscopy reveals that the ohmic resistivity of the nanofoam is 4x higher than the carbon paper and the estimated resistivity (24.2×10^{-3} Ω cm) is in good agreement with the manufacturer's specification. Kinetic parameters for both V(II) and V(V) discharging reactions are extracted from *IR* compensated Tafel plots and compared: the nanofoam shows superior kinetic characteristics to the carbon paper, offering 9x higher rate constant for V(II) oxidation and 5.2x higher for V(V) reduction. The effect of heat treatment on kinetics is found to be negligible.
- The microfluidic fuel cell devices employing carbon nanofoam as electrodes, regardless of the heat treatment, demonstrate significantly reduced activation overpotentials due to the high active surface area and rapid kinetics, which is a major advantage for overall fuel cell performance. However, in the linear regime of the polarization curves, the slopes of the nanofoam cells are steeper than that of the baseline, indicative of higher ohmic losses during cell operation. In addition, convective mass transport of liquid electrolytes through the nano-scale pores is limited, preventing the net surface area from being fully utilized. Consequently, the nanofoam cells offer only a moderate improvement in peak power density (6% higher at 10 μL min-1) compared to the baseline cell, provided that the gain of fast kinetic rates is compromised by the combined effect of increased ohmic losses and reduced mass transport rates of the nanofoam material.

8.1.5. Double-pass Fuel Cell Architecture

A new cell architecture is proposed adapting a double-pass concept. In the proposed cell design, unutilized fuel/oxidants can be consumed at the second half of the electrode. In addition, since the flow inlet area is reduced by half, this innovative design allows approximately double the convectional mass transport at a given electrode length and flow rate. Along with numerical studies, prototype cells are fabricated, tested and compared to the baseline and current collector cells:

The proposed cell shows significantly improved performance: the power density at 300 μL/min is almost as good as the current collector cell, which is the highest in this field; a 54% increase in the peak power density is achieved at 10 μL/min, compared to the baseline cell.

In parallel with the discharging study on the proposed cell discussed in this chapter, the charging mode operation is being investigated by our group. This proposed cell is anticipated to open up new research opportunities in a membraneless, microfluidic redox flow battery, which has not been actively researched yet.

8.2. Future Works

Based on the results and observations from the current studies, several recommendations can be made for the future development of microfluidic fuel cells:

- Activation overpotential: carbon nanofoam materials provide higher surface area and faster kinetics than the carbon paper. Hence, nanofoam electrodes are suitable for fuel cell devices operating in the high cell voltage regime. However, as the current density is increased, higher ohmic overpotentials and mass transport limitations will gradually offset the gain from its faster kinetics. Therefore, future works in the material development would be focused on lowering both ohmic and fluidic resistances. Uniform distribution of the pore sizes is also important to maximize the utilization of active electrode areas without any unwanted bypasses of the electrolyte streams.
- Ohmic overpotential: a thin film current collector effectively reduces the overall cell resistance and therefore improves the cell performance. Further enhancement in cell performance is expected, provided that the contact between the porous electrode and current collector is improved: a uni-body design will be preferable in this context. We anticipate that non-PTFE treated porous media with smoother surfaces would be a more suitable choice in this context.
- Mass transport overpotential: the mass transport limits are greatly improved by the double-pass design. However, this proposed cell is profoundly susceptible to the fuel /oxidant crossover since the unutilized fuel/oxidant are supposed to be consumed at the second half of the electrode. Hence, a new strategy of reducing the crossover is essential for further enhancements of the proposed cell.

To make a major commercial break-through in the miniaturized fuel cells, much further research efforts are required. The main challenge lies in developing a microfluidic fuel cell system integrated with auxiliary components such as micro pumps, fluid reservoirs, and control units. In addition, the power output should be at least in the 1-20 W range for portable electronic devices, with high overall energy density. The research opportunities in this field are numerous, including unit cell improvements, scale-up solutions, and system integration,

References

[1] Kjeang, E., Djilali, N. and Sinton, D. (2009) "Advances in Microfluidic Fuel Cells" In T. Zhao (ED), Micro Fuel Cells: Principles and Applications (pp.100-137)

[2] Meyers, J.P. and Maynard, H.L. (2002) "Design considerations for numaturized PEM fuel cells", *Journal of Power Sources*, 109, 76-88

[3] Nguyen, N.T. and Chan, S.H. (2006) "Micromachined polymer electrolyte membrane and direct methanol fuel cells - a review", *Journal of Micromechanics and Microengineering*, 16, R1-R12

[4] Morse, J.D. (2007) "Micro-fuel cell power sources", *International Journal of Energy Research*, 31, 576-602

[5] Kundu, A., Jang, J.H., Gil, J.H., Jung, C.R., Lee, H.R., Kim, S.H., Ku, B. and Oh, Y.S. (2007) "Micro-fuel cells - Current development and applications", *Journal of Power Sources*, 170, 67-78

[6] Wang, Y., Pham, L., de Vasconcellos, G.P.S. and Madou, M. (2010) "Fabrication and characterization of micro PEM fuel cells using pyrolyzed carbon current collector plates", *Journal of Power Sources*, 195, 4796-4803

[7] Chiao, M., Lam, K.B. and Lin, L.W. (2006) "Micromachined microbial and photosynthetic fuel cells", *Journal of Micromechanics and Microengineering*, 16, 2547-2553

[8] Ferrigno, R., Stroock, A.D., Clark, T.D., Mayer, M. and Whitesides, G.M. (2002) "Membraneless vanadium redox fuel cell using laminar flow ", *Journal of the American Chemical Society*, 124, 12930-12931

[9] Choban, E.R., Markoski, L.J., Wieckowski, A. and Kenis, P.J.A. (2004) "Microfluidic fuel cell based on laminar flow", *Journal of Power Sources*, 128, 54-60

[10] Choban, E.R., Spendelow, J.S., Gancs, L., Wieckowski, A. and Kenis, P.J.A. (2005) "Membraneless laminar flow-based micro fuel cells operating in alkaline, acidic, and acidic/alkaline media", *Electrochimica Acta*, 50, 5390-5398

[11] Cohen, J.L., Westly, D.A., Pechenik, A. and Abruna, H.D. (2005) "Fabrication and preliminary testing of a planar membraneless microchannel fuel cell", *Journal of Power Sources*, 139, 96-105

[12] Jayashree, R.S., Gancs, L., Choban, E.R., Primak, A., Natarajan, D., Markoski, L.J. and Kenis, P.J.A. (2005) "Air-breathing laminar flow-based microfluidic fuel cell", *Journal of the American Chemical Society*, 127, 16758-16759

[13] Kjeang, E., Michel, R., Harrington, D.A., Djilali, N. and Sinton, D. (2008) "A microfluidic fuel cell with flow-through porous electrodes", *Journal of the American Chemical Society*, 130, 4000-4006

[14] Salloum, K.S. and Posner, J.D. (2010) "Counter flow membraneless microfluidic fuel cell", *Journal of Power Sources*, 195, 6941-6944

[15] Moore, S., Sinton, D. and Erickson, D. (2011) "A plate-frame flow-through microfluidic fuel cell stack", *Journal of Power Sources*, 196, 9481-9487

[16] Kjeang, E., Proctor, B.T., Brolo, A.G., Harrington, D.A., Djilali, N. and Sinton, D. (2007) "High-performance microfluidic vanadium redox fuel cell", *Electrochimica Acta*, 52, 4942-4946

[17] Senturia, S.D. (2001) "Microsystem Design", Norwell, Kluwer Academic Publisher

[18] Kjeang, E., Djilali, N. and Sinton, D. (2009) "Microfluidic fuel cells: A review", *Journal of Power Sources*, 186, 353-369

[19] Shaegh, S.A.M., Nguyen, N.T. and Chan, S.H. (2011) "A review on membraneless laminar flow-based fuel cells", *International Journal of Hydrogen Energy*, 36, 5675-5694

[20] Giner, J., Swette, L. and Cahill, K. (1976) NASA TM-19760, US Dept. of Energy

[21] Thaller, L.H. (1979) NASA TM-79143, US Dept. of Energy

[22] Sum, E. and Skyllas-kazacos, M. (1985) "A Study of the V(Ii)/V(Iii) Redox Couple for Redox Flow Cell Applications", *Journal of Power Sources*, 15, 179-190

[23] Sum, E., Rychcik, M. and Skyllas-kazacos, M. (1985) "Investigation of the V(V)/V(Iv) System for Use in the Positive Half-Cell of a Redox Battery", *Journal of Power Sources*, 16, 85-95

[24] Gattrell, M., Park, J., MacDougall, B., Apte, J., McCarthy, S. and Wu, C.W. (2004) "Study of the mechanism of the vanadium 4+/5+redox reaction in acidic solutions", *Journal of the Electrochemical Society*, 151, A123-A130

[25] Krishnamurthy, D., Johansson, E.O., Lee, J.W. and Kjeang, E. (2011) "Computational modeling of microfluidic fuel cells with flow-through porous electrodes", *Journal of Power Sources*, 196, 10019-10031

[26] Larminie, J. and Dicks, A. (2003) "Fuel Cell Systems Explained", Chichest, West Sussex, John Wiley & Sons Inc.

[27] Mench, M.M. (2008) "Fuel Cell Engines", Hoboken, NJ, John Wiley & Sons Inc.

[28] Haynes, W.M. and Bruno, T.J. (2002) "Handbook of Chemistry and Physics", Boca Raton, CRC Press

[29] Fabjan, C., Garche, J., Harrer, B., Jorissen, L., Kolbeck, C., Philippi, F., Tomazic, G. and Wagner, F. (2001) "The vanadium redox-battery: an efficient storage unit for photovoltaic systems", *Electrochimica Acta*, 47, 825-831

[30] Shah, A.A., Watt-Smith, M.J. and Walsh, F.C. (2008) "A dynamic performance model for redox-flow batteries involving soluble species", *Electrochimica Acta*, 53, 8087-8100

[31] Al-Fetlawi, H., Shah, A.A. and Walsh, F.C. (2009) "Non-isothermal modelling of the all-vanadium redox flow battery", *Electrochimica Acta*, 55, 78-89

[32] McDonald, J.C., Duffy, D.C., Anderson, J.R., Chiu, D.T., Wu, H.K., Schueller, O.J.A. and Whitesides, G.M. (2000) "Fabrication of microfluidic systems in poly(dimethylsiloxane)", *Electrophoresis*, 21, 27-40

[33] Hoang, L. (2010) "Proton Exchange Membrane (PEM) Electrolytic Recharging Cell for Vanadium Redox Species", internal communication

[34] Bird, R.B., Stewart, W.E. and Lightfoot, E.N. (2007) "Transport Phenomena", New York, NY, John Wiley & Sons Inc.

[35] You, D.J., Zhang, H.M. and Chen, J. (2009) "A simple model for the vanadium redox battery", *Electrochimica Acta*, 54, 6827-6836

[36] Schmal, D., Vanerkel, J. and Vanduin, P.J. (1986) "Mass-Transfer at Carbon-Fiber Electrodes", *Journal of Applied Electrochemistry*, 16, 422-430

[37] Lee, J.W. and Kjeang, E. (2011) "A Parametric Study on Microfluidic Vanadium Fuel Cells" 9th Fuel Cell Science, Engineering and Technology Conference, ASME, Washington DC

[38] Gostick, J.T., Fowler, M.W., Pritzker, M.D., Ioannidis, M.A. and Behra, L.M. (2006) "In-plane and through-plane gas permeability of carbon fiber electrode backing layers", *Journal of Power Sources*, 162, 228-238

[39] TGPH-060, TORAY Industries, http://fuelcellstore.com/products/toray/specs.pdf (2011)

[40] Hussaini, I.S. and Wang, C.Y. (2010) "Measurement of relative permeability of fuel cell diffusion media", *Journal of Power Sources*, 195, 3830-3840

[41] Fluent 6.3 Documentation, www.fluentusers.com (2011)

[42] Schmicker, W. and Santos, E. (2010) "Interfacial Electrochemistry", New York, Springer

[43] de Leon, C.P., Frias-Ferrer, A., Gonzalez-Garcia, J., Szanto, D.A. and Walsh, F.C. (2006) "Redox flow cells for energy conversion", *Journal of Power Sources*, 160, 716-732

[44] Skyllas-Kazacos, M., Kazacos, G., Poon, G. and Verseema, H. (2010) "Recent advances with UNSW vanadium-based redox flow batteries", *International Journal of Energy Research*, 34, 182-189

[45] Kazacos, M., Cheng, M. and Skyllas-kazacos, M. (1990) "Vanadium Redox Cell Electrolyte Optimization Studies", *Journal of Applied Electrochemistry*, 20, 463-467

[46] Zhong, S. and Skyllaskazacos, M. (1992) "Electrochemical-Behavior of Vanadium(V) Vanadium(Iv) Redox Couple at Graphite-Electrodes", *Journal of Power Sources*, 39, 1-9

[47] Yamamura, T., Watanabe, N., Yano, T. and Shiokawa, Y. (2005) "Electron-transfer kinetics of Np3+/Np4+, NpO2+/NpO22+, V2+/V3+, and VO2+/VO2+ at carbon electrodes", *Journal of the Electrochemical Society*, 152, A830-A836

[48] Lee, J.W. and Kjeang, E. (2012) "Chip-Embedded Thin Film Current Collector for Microfluidic Fuel Cells", *International Journal of Hydrogen Energy*, 37, 9359-9367

[49] Bard, A.J. and Faulkner, L.R. (2001) "Electrochemical Methods: Fundamentals and Applications", Hoboken, NJ, John Wiley & Sons

[50] Oriji, G., Katayama, Y. and Miura, T. (2005) "Investigations on V(IV)/V(V) and V(II)/V(III) redox reactions by various electrochemical methods", *Journal of Power Sources*, 139, 321-324

[51] Oriji, G., Katayama, Y. and Miura, T. (2004) "Investigation on V(IV)/V(V) species in a vanadium redox flow battery", *Electrochimica Acta*, 49, 3091-3095

[52] Pekala, R.W. (1989) "Organic Aerogels from the Polycondensation of Resorcinol with Formaldehyde", *Journal of Materials Science*, 24, 3221-3227

[53] Wang, J., Angnes, L., Tobias, H., Roesner, R.A., Hong, K.C., Glass, R.S., Kong, F.M. and Pekala, R.W. (1993) "Carbon Aerogel Composite Electrodes", *Analytical Chemistry*, 65, 2300-2303

[54] Pekala, R.W., Farmer, J.C., Alviso, C.T., Tran, T.D., Mayer, S.T., Miller, J.M. and Dunn, B. (1998) "Carbon aerogels for electrochemical applications", *Journal of Non-Crystalline Solids*, 225, 74-80

[55] Al-Muhtaseb, S.A. and Ritter, J.A. (2003) "Preparation and properties of resorcinol-formaldehyde organic and carbon gels", *Advanced Materials*, 15, 101-114

[56] Snyder, J.F., Wong, E.L. and Hubbard, C.W. (2009) "Evaluation of Commercially Available Carbon Fibers, Fabrics, and Papers for Potential Use in Multifunctional Energy Storage Applications", *Journal of the Electrochemical Society*, 156, A215-A224

[57] Lytle, J.C., Wallace, J.M., Sassin, M.B., Barrow, A.J., Long, J.W., Dysart, J.L., Renninger, C.H., Saunders, M.P., Brandell, N.L. and Rolison, D.R. (2011) "The right kind of interior for multifunctional electrode architectures: carbon nanofoam papers with aperiodic submicrometre pore networks interconnected in 3D", *Energy & Environmental Science*, 4, 1913-1925

[58] Lee, J.W., Hong, J.K. and Kjeang, E. (2012) "Electrochemical characteristics of vanadium redox reactions on porous carbon electrodes for microfluidic fuel cell applications", *Electrochimica Acta*, 83, 430-438

[59] MarkeTech, http://www.mkt-intl.com/aerogel/Carbon_Nanofoam.shtml (2012)

Appendices

Appendix A.

Microfabrication

The microfluidic fuel cells introduced in this thesis are fabricated by a series of microfabrication sequence described here:

1. Mater (mold) fabrication

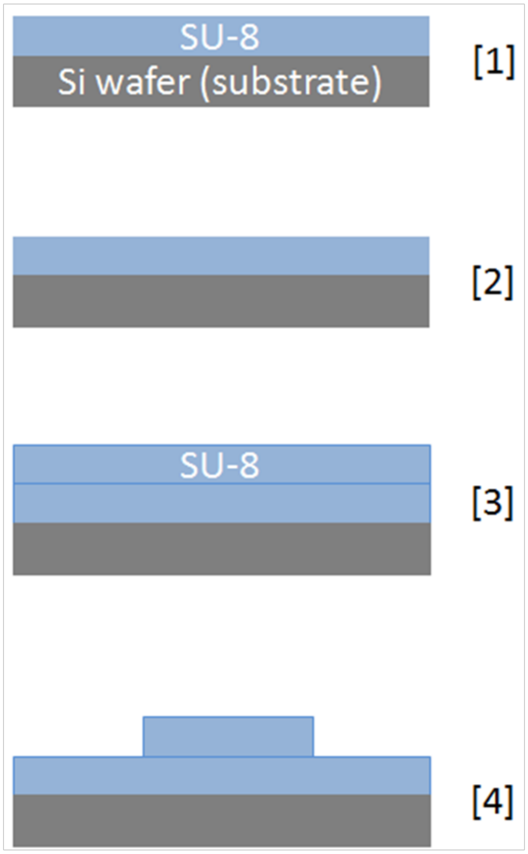

Step	Description
[1]1st layer	Spin coating at 1030 rpm, curing at 65 °C(10 min), 95 °C(45 min)
[2] 1st layer	Flood exposure for 18 sec
	Post exposure bake at 65 °C(5 min), 95 °C(15 min)
[3] 2nd layer	Spin coating at 1030 rpm, curing at 65 °C(10 min), 95 °C(45 min)
[4] 2nd layer	Exposure with mask for 18 sec
	Post exposure bake at 65 °C(5 min), 95 °C(15 min)
	Develop for approximately 20 min

Note that the first layer is intended to serve as an adhesion layer for the second layer (mold structure) in order to use the master multiple times without delamination issues.

2. PDMS & bonding

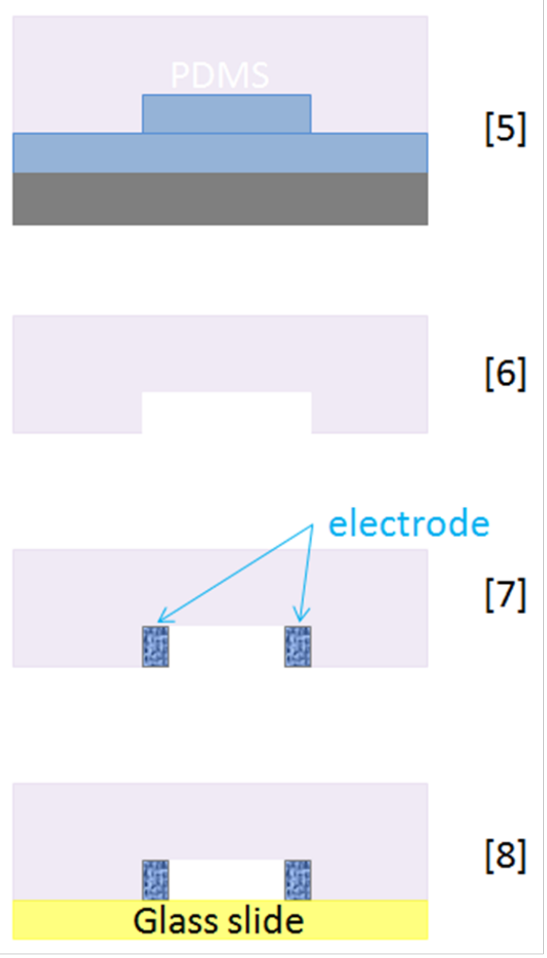

Step	Description
[5] PDMS	Dispening PDMS manually, curing for 48 hours at room temperature
[6] PDMS	Peeling off from the master
[7] Electrode	Inserting electrode manually
[8] Bonding	Applying corona discharger for 1 min to both glass slide and PDMS

Note that the average fabrication time for the current process is approximately 1 week.